A New Switch-Count Reduction Configuration and New Control Strategies for Regenerative Cascaded H-Bridge Medium Voltage Motor Drives

A NEW SWITCH-COUNT REDUCTION CONFIGURATION AND NEW CONTROL STRATEGIES FOR REGENERATIVE CASCADED H-BRIDGE MEDIUM VOLTAGE MOTOR DRIVES

BY

SARAH MOHAMED BADAWI, B.Sc.

A THESIS

SUBMITTED TO THE DEPARTMENT OF ELECTRICAL & COMPUTER ENGINEERING

AND THE SCHOOL OF GRADUATE STUDIES

OF MCMASTER UNIVERSITY

IN PARTIAL FULFILMENT OF THE REQUIREMENTS

FOR THE DEGREE OF

MASTER OF APPLIED SCIENCE

© Copyright by Sarah Mohamed Badawi, October 2020

All Rights Reserved

Master of Applied Science (2020) McMaster University

(Electrical & Computer Engineering) Hamilton, Ontario,

Canada

TITLE: A New Switch-Count Reduction Configuration and New Control Strategies for Regenerative Cascaded H-Bridge Medium Voltage Motor Drives

AUTHOR:

Sarah Mohamed Badawi
B. Sc.
Ain Shams University, Cairo, Egypt

SUPERVISOR:

Dr. Mehdi Narimani

NUMBER OF PAGES:

xxiii, 195

To my husband, my parents, my late grandparents,

my siblings, nieces and nephew.

All that I am and all that I have is because of them.

Abstract

Cascaded H-bridge (CHB) multilevel inverters have significant popularity with motor drives applications due to their modularity, scalability, and reliability. Typical CHB inverters employ diode rectifiers that allow unidirectional power flow from the grid to the load. To capture and utilize the regenerated energy in regenerative applications, regenerative CHB drives were introduced with two-level voltage source converters in the front end to allow bidirectional energy flow. This solution is accompanied by challenges of high number of switches and control circuits, high switching power losses, and massive dimensions. Recently, developing more economic versions of regenerative cascaded H-bridge drives has become one of the hottest topics in power electronics research.

In this thesis work, two solutions are proposed for more energy efficient and economic regenerative CHB drives. The first solution is a proposed power cell configuration that reduces the number of switches per cell by two. Additionally, phase alternation connection method and carrier phase-shifting techniques are introduced to

address the challenges of the presented configuration. The switch-count reduction reduces the system's complexity, switches' cost, and footprint.

The second proposed solution is a new controller to operate the front-end converters as fundamental frequency ends (FFEs). The proposed controller is employed in both the conventional regenerative cascaded H-bridge and the proposed reduced switch-count configuration. This solution minimizes the switching power losses, and results in more compact and economic design, with higher DC-link utilization.

Theoretical analysis and simulation studies of both proposed solutions show promising performance and capability to be applied as energy-efficient and cost effective regenerative CHB motor drives.

Experimental validation of the proposed reduced switch-count configuration is presented for STATCOM operation of a scaled-down 7-Level regenerative CHB drive system. The future work of this thesis includes experimental validation of the proposed FFE controller, and operation of the system with regenerative motor load.

Acknowledgements

First and Foremost, I would like to sincerely thank the Almighty God for His endless and uncountable graces, and for blessing me with the strength, knowledge, persistence and opportunity to undertake this research work and complete it.

The completion of this thesis has been a wonderful journey with many persons whom I would like to truly thank. My sincere appreciation goes to my supervisor Dr. Mehdi Narimani for his guidance, efforts, advice, and support during my graduate studies. I have and I am still learning from him and will always be grateful for the opportunities he offered and the knowledge I gained from him on personal, professional, and academic levels.

I would also like to express my deepest gratitude to my motor drives research team in HiPEL for the very fruitful scientific discussions and insights along the way, and for the work on the experimental prototype that was a great team work since the first day. Zhituo Ni, who has taught me a lot professionally and personally, led the team

in in detailed PCB design and mentored me during my work, and has never hesitated to share his knowledge and experience. Ahmed Hisham, who has always been there for advice, assistance and discussion, and whose leading work and continuous contribution on the prototype control and hardware from the start and during the uncertain times and situation of the pandemic has played an undeniable role in the whole team reaching a significant milestone. Shaoyi Yuan, who has always be there for assistance and useful discussions.

My gratitude is also extended to all my colleagues and the staff in Electrical and Computer Engineering department. I would like to especially thank Cheryl Gies and Tracey Coop, whose smiles, care, support, and help have always been there for me. Also, I would like to thank the department technical support team for the precious help with the needed software resources.

I would also like to truly thank Dr. Navid Zargari and George Cheng from the R&D team in Rockwell Automation Canada for their guidance and support. As our research industrial partners, they both have provided me with fruitful discussions, and practical and industrial remarks and insights that have helped me throughout my research work.

Last but certainly not least, a very special thank you to my family and friends. My parents, Afaf and Mohamed Badawi, I would not have been here and nothing would have been achieved without their unconditional love, support, and efforts. My husband, Ahmed, whom I could have never achieved anything without his love, support, patience, and encouragement in every single step. My siblings, Shaimaa, Hagar, and Ahmed, and their beautiful families who are always there for me no matter what, with their love and support. My parents-in-law, Azza and Hisham Abdelrazek for their ultimate support and love. My late grandparents, whose love and care is still here. Dr. Badr and Dr. Somayya, who have taught me a lot with their wisdom and devotion during their lives. My friends: Alaa, Bassant, Eman, Nada, Sally, Salma, Samaa, Sara, Sarah, Shaza, Toka, Yara, and Maria for their continuous support and their presence in my life.

This research work has been conducted thanks to the funding from Rockwell Automation Canada, the support from Mathworks with Matlab/Simulink, the support from dSpace with MicroLabBox and ControlDesk, and the support from Altium with Altium Designer.

Contents

List of Figures

List of Tables

Chapter 1

Introduction

1.1 Background

Motor drive, in definition, is a device that converts fixed input frequency and voltage to variable output frequency and voltage in order to directly control motor speed and torque [1]. It is commonly referred to as adjustable speed drive (ASD) or variable speed drive (VSD) [1]. For high power motors, medium voltage operation is preferred as it results in lower current for the same power rating in comparison with low voltage operation. Thus, it reduces the cables' size, copper weight and cost, lowers the power losses, and improves the efficiency of the system [1].

From the late 1990s, the technological evolution of high-power semiconductors devices, especially of insulated gate bipolar transistors (IGBTs), has led to the advancement and the prevalence of medium voltage (MV) motor drives [2]. MV drives cover the power ranges from 0.4 MW to 40 MW with medium voltage ratings of 2.3 kV to 13.8 kV. Nevertheless, most of the MV drives in commission are between 1 MW to 4 MW in power ratings with voltage levels of 3.3 kV to 6.6 kV [2].

MV drives are mainly used in heavy industry applications [1], [2]. Pipeline pumps in the petrochemical industry, cooler exhaust fans in the cement industry, conveyors in mining and steel industry, main propulsion propellers in the marine, feed water pumps in power generation, and traction drives in the transportation industry are just few examples.

In a market study [1], general purpose applications that do not require high dynamic performance represent 80% of the MV drives market, while the remaining 20% are special purpose applications with higher performance requirements as shown in Fig. 1.1.

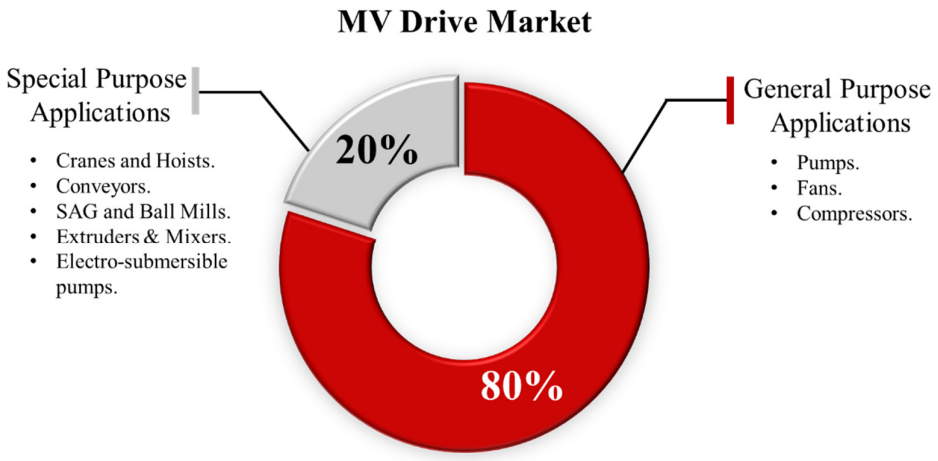

Fig. 1.1. Medium Voltage Drives Market [1].

Currently, only 3% of the installed motors employ MV drives, while the remaining 97% operate at fixed speed as shown in Fig. 1.2 [2].

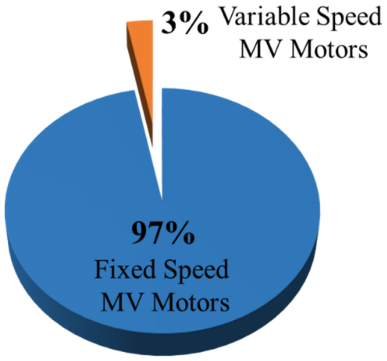

Fig. 1.2. Medium Voltage Motors in Commission [2].

In fixed-speed motors, the control of the fluid flow through a fan or compressor is only achieved using mechanical damping systems and control valves as illustrated in the performance curves provided in Fig. 1.3 [1], [2]. Consequently, considerable amount of energy is wasted.

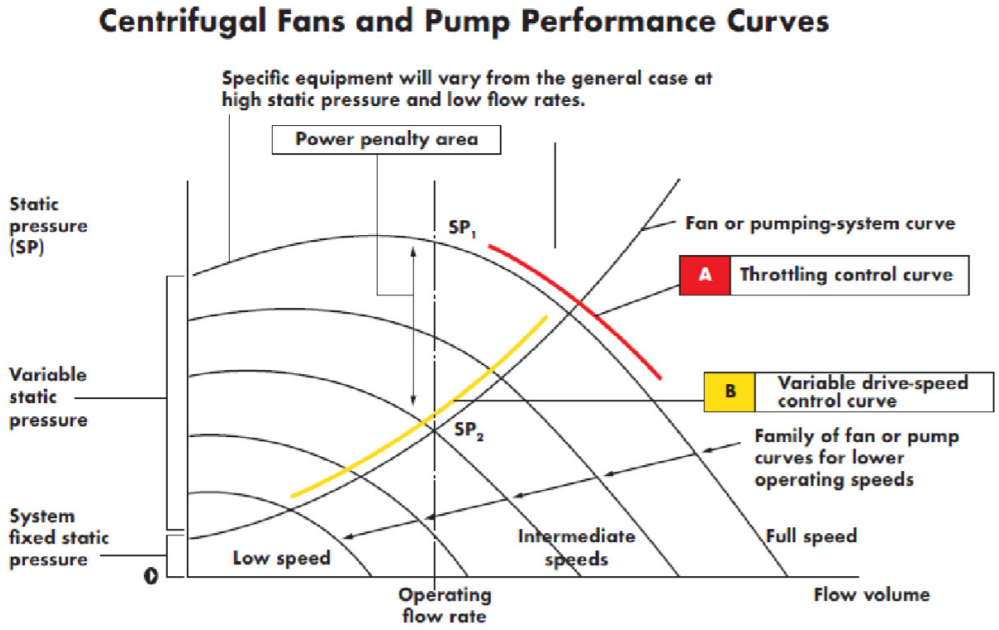

Fig. 1.3. Centrifugal Fans and Pumps Performance Curves [1].

The variable speed drive control curve in Fig. 1.3 indicates that the use of MV drives as a retrofit in these systems can save energy significantly and increase the productivity. According to [1], the use of VFD with a 1000 HP motor can save 25% of its electricity costs. As a result, an MV-VFD can payback its cost within 1 to 2 years.

The general structure of MV drives is illustrated in Fig. 1.4 [2].

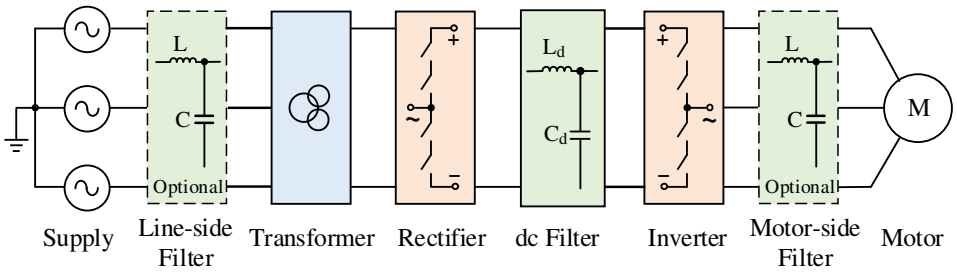

Fig. 1.4. General Block Diagram of Medium Voltage Drives [2].

Typically, an MV drive consists of:

1. ***Phase-shifting transformer***: mainly used to reduce line currents distortion.
2. ***Rectifier***: used to obtain the desired DC voltage. It can be either uncontrolled or controlled rectifier depending on the system requirements.
3. ***DC filter***: can be either a capacitor to provide stiff DC voltage, or an inductor to smooth the DC current depending on the inverter type.
4. ***Inverter***: converts the electrical energy from DC form to controllable AC form. Inverters are classified into voltage source inverters (VSIs), and current source inverters (CSIs). VSIs synthesize the output AC voltage from a fixed DC voltage. On the other hand, CSIs produce the output AC currents from fixed DC current. For the sake of brevity and to stay within the focus of this work, only VSIs are considered hereinafter.

5. ***Input and output line filters***: are added depending on the system requirements, and the type of used converter.

Unlike low voltage drives, the nature of MV drives poses many requirements as well as challenges. These requirements can be summarized in the following [2]:

1. ***Line-side requirements***: compliance with the grid connection standards, high input power factor (>0.9), and LC resonance suppression in case of having input LC filter.
2. ***Motor-side requirements***: low voltage stress (*dv/dt*), common mode voltage stress minimization, low total harmonic distortion, and LC resonance suppression in case of using output LC filter.
3. ***Switching devices considerations***: compromising between high performance of high switching frequency operation, their power losses, and the waveform distortion. In addition to the need for static and dynamic voltage equalizing techniques in case of switches' series connection.
4. ***Overall drive requirements***: high efficiency, low manufacturing cost, small footprint with easy installation, high reliability with minimum repair downtime, and fault-tolerant operation.

The line-side requirements are addressed in the rectification stage through using multi-pulse rectifier in conjunction with phase-shifting transformer to provide low harmonic content. The inverter design, on the other hand, being the main core of the drive, must take into consideration the motor-side, switching devices, and most of the overall system requirements.

Fig. 1.5 shows an MV two-level VSI phase leg [2],, and the resulting line-to-line voltage. The output voltage suffers from high *dv/dt*, and high common mode voltage

stress. In order to withstand medium voltage stress, switching devices are connected in series. In addition, very high switching frequency is required to have acceptable harmonic content. All these factors have made the 2L-VSI configuration not suitable for MV applications [3].

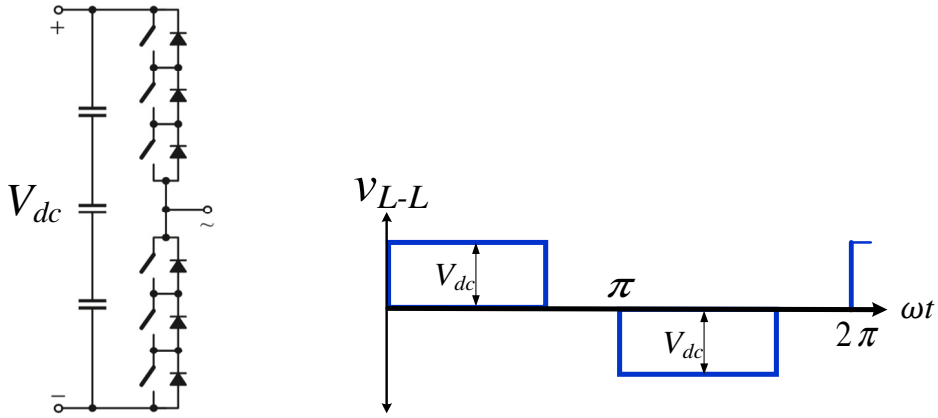

(a) MV 2L-VSI Phase Leg [2]. (b) Line-to-Line Output Voltage.

Fig. 1.5. Medium Voltage Two-Level Voltage Source Inverter.

To address the above challenges, multilevel inverters (MLIs) were introduced as the ultimate solution for the medium and high voltage applications [2]-[4]. In MLIs, high output voltage is synthesized as a stepped waveform of several low voltage levels as shown in Fig. 1.6(a). Compared to MV 2L-VSI, MLIs have the following features [2]-[4]:

- Reduced voltage stress (*dv/dt*) and common mode voltage stress.
- Lower harmonic distortion.
- Lower devices' switching frequency.
- No switches' series connection.
- Lower electromagnetic interference.

Numerous MLI topologies have been proposed in literature [2]-[7]. Fig. 1.6(b) shows the most common three topologies used in MV drives: neutral-point clamped

(NPC) MLIs [2]-[5], flying capacitor (FC) MLIs [2]-[4], and cascaded H-bridge (CHB) MLIs [2]-[4], [6].

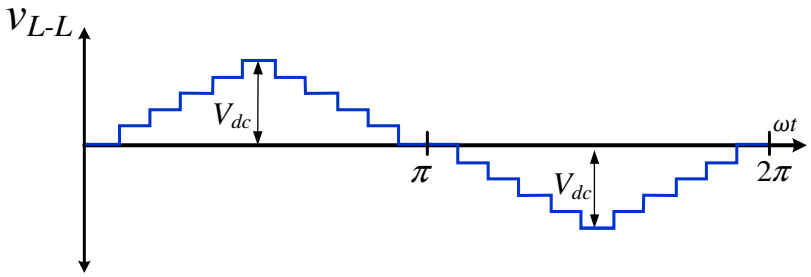

(a) Multilevel Inverter Output Line-to-Line Voltage.

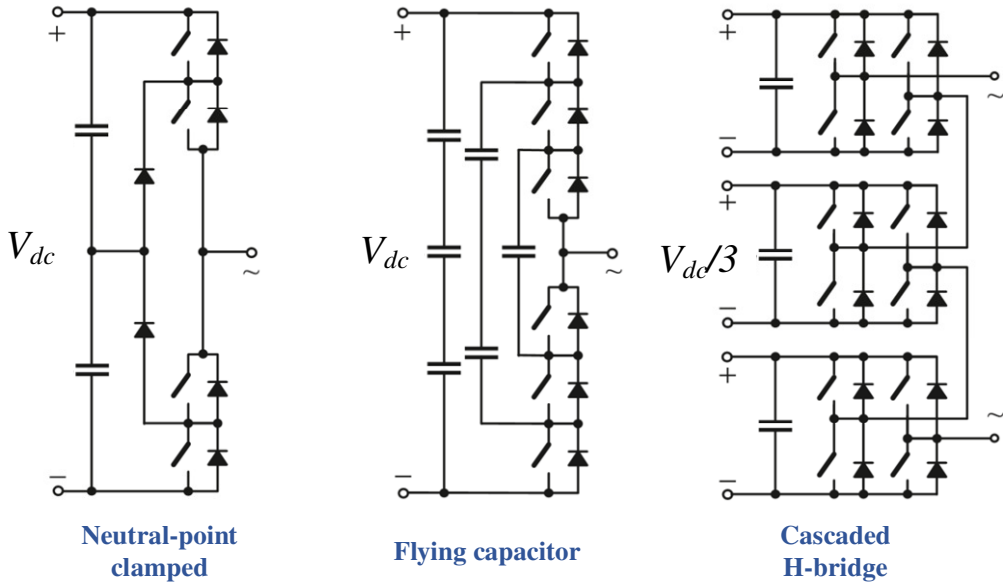

(b) NPC MLI, FC MLI, and CHB MLI Phase Legs [2].

Fig. 1.6. Multilevel Inverters.

1.2 Motivation

As shown in Fig. 1.6(b), each CHB MLI phase leg consists of multiple low voltage units with their outputs connected in series to produce the required voltage. This structure has caused CHB MLIs to be advantageous over other MLIs due to the following:

- Employing the least number of total components to produce the same number of voltage levels, as illustrated in Table 1.1 [7].

TABLE 1.1. COMPARISON BETWEEN POWER COMPONENTS IN DIFFERENT TOPOLOGIES TO GENERATE (M) PHASE VOLTAGE LEVELS [7].

Inverter Configuration	**NPC**	**FC**	**CHB**
Main Switching Devices	2(m-1)	2(m-1)	2(m-1)
Clamping Diodes	(m-1) (m-2)	0	0
DC-link Capacitors	(m-1)	(m-1)	(m-1)/2
Flying Capacitors	0	(m-1)(m-2)/2	0

- No neutral point or capacitor voltage balancing problems [2], [7].
- Scalable design that is easier to maintain with minimal repair downtime [2], [7].
- Fault tolerant capability due to their modular structure [2], [7].

Consequently, CHB-based MV motor drives have placed themselves in numerous industries such as oil and mining, marine, cement, and power generation [1], [2]. Table 1.2 shows examples of the existing CHB-based MV drives in the market, their voltage and power ranges, and their manufacturers [2], [8]-[11]. Fig. 1.7 shows one example of these drives, the HIVECTOL-HVI by Hitachi [9].

TABLE 1.2. EXISTING INDUSTRIAL CHB-BASED MV MOTOR DRIVES [2], [8]-[11].

Product Name	**Manufacturer**	**Voltage Range**	**Power Range**
Powerflex 6000 [2], [8]	*Rockwell Automation*	2.3 to 11 kV	Up to 11 MVA
HIVECTOL-HVI [9]	*Hitachi*	2.4 to 11 kV	0.31 to 16.7 MVA
ACS580MV [10]	*ABB*	6 to 11 kV	0.2 to 6.3 MVA
Perfect Harmony GH-180 [2], [11]	*Siemens*	2.3 to 11 kV	0.12 to 24.4 MVA

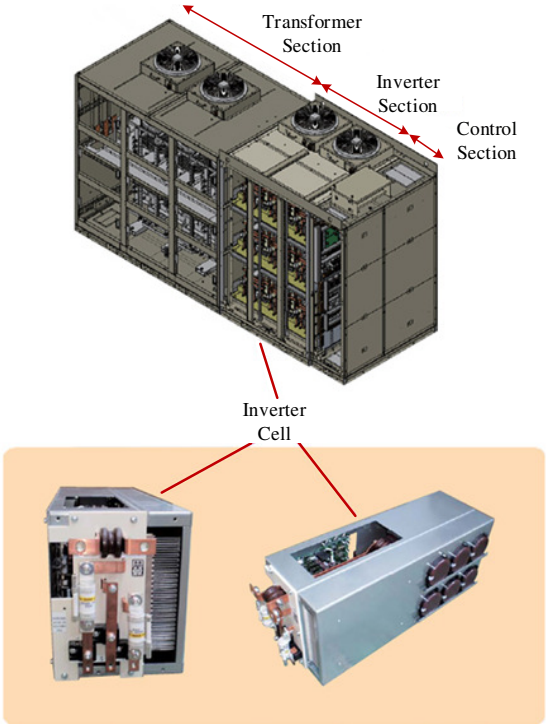

Fig. 1.7. HIVECTOL-HVI by Hitachi (Courtesy of Hitachi) [9].

The typical configuration of CHB-based MV drive employs three-phase diode rectifier in each CHB unit [2]. As a result, only unidirectional power flow from the grid side to the motor side is allowed.

In some MV motor drives applications, where the load can overhaul the motor such as downhill conveyors, cranes, and hoists, or where the load has very high inertia [1], rated power can be regenerated from the motor side instead of being consumed. Fig. 1.8 shows the amount of regenerated power from a downhill conveyor with linear ramp stop profile [1]. Table 1.3 illustrates the regeneration applications by industry [1]. If the installed motor drive does not have regeneration capability, this regenerated energy would have to be dissipated in form of heat in a resistor load [12], which makes the system energy inefficient, and increases its cost, dimensions, and carbon footprint.

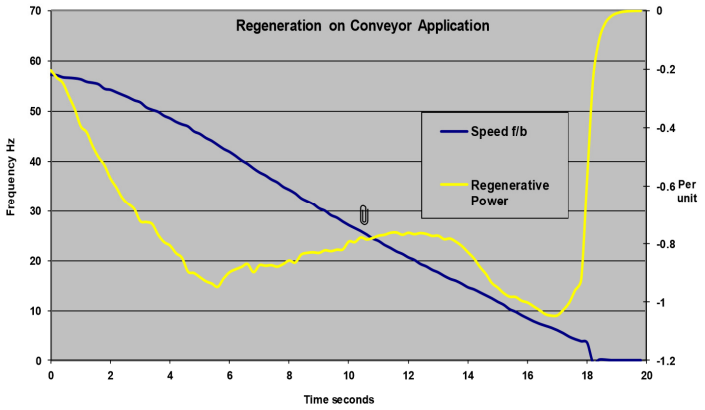

Fig. 1.8. Downhill Conveyor Regenerative Linear Ramp Stop [1].

TABLE 1.3. REGENERATION APPLICATIONS BY INDUSTRY [1].

Industry Segment	Applications
Cement	• Material handling conveyors • Pre-heater induced draft fans • Ball mills
Marine (Commercial)	• Propulsion and positioning drives • Anchor handling
Mining	• Bucket wheel excavator and reclaimer • Dragline
Oil and Gas	• Drill stem • Oil centrifuge • Pipeline booster pump
Power Generation	• Boiler induced draft fan

Accordingly, bidirectional power flow between the grid and the motor is advantageous in these applications. To allow bidirectional power flow in a CHB power cell, the replacement of the diode bridge rectifier with a three-phase PWM (2L-VSI) rectifier was introduced [12]-[14]. However, this comes with many challenges including increase in the system number of switches, power losses, cost, complexity, and failure probability, which outweigh its advantages compared with other regenerative MLIs. In the recent years, introducing more optimized topologies and control techniques for regenerative CHB-based MV drives has become one of the hottest areas in the industrial motor drives research [14] - [21].

The motivation of this thesis work is to deliver more efficient and economic versions of regenerative CHB motor drives that can place them in the regenerative applications market. In this work, two solutions are proposed hereinafter to achieve this goal: switch-count reduction, and switching frequency reduction. Throughout the thesis, each of these solutions is thoroughly investigated and analyzed. For analysis verification, a simulation model of regenerative CHB drive in Matlab/Simulink has been developed on which performance studies are conducted. The proposed methods show promising performance to be employed in the next-generation of regenerative CHB motor drives. In addition, a scaled down regenerative CHB drive experimental setup was implemented to validate the proposed methods.

1.3 Contributions

The contributions of the presented work can be outlined as follows:

- An extensive literature review of the existing reduced switch-count regenerative CHB motor drives. These topologies structure, performance, modulation, and control are investigated to point out their main drawbacks that are needed to be overcome.
- Proposal of a new reduced switch-count regenerative CHB power cell configuration based on four-switch three-phase inverter active front end. For a $2m+1$ level CHB drive, the proposed configuration reduces the number of switches by $6m$. Detailed analysis of the proposed topology performance, control, and the resulting challenges has been provided.

- Proposal of phase-alternation connection for the proposed configuration to eliminate current unbalance, triplen and carrier harmonics from the input primary currents.
- Proposal of two carrier phase shifting methods for the proposed configuration to eliminate the carrier side band harmonics and comply with the grid connection standards.
- Analysis of the application of sinusoidal PWM (SPWM) with and without third order harmonic injection on the proposed configuration. SPWM without third order harmonic injection has proven to have better overall performance in the proposed configuration.
- Model implementation of a regenerative CHB drive using the proposed topology and techniques with a regenerative FOC controlled motor on Matlab/Simulink. The simulation studies on this model show a promising performance of the system and very high potential to be applied as a retrofit in regenerative applications.
- Proposal of a new fundamental frequency end (FFE) controller with the highest DC-link voltage utilization factor, DC-link voltage regulation, and reactive power flow control.
- Application of the proposed FFE controller in regenerative CHB motor drive with 2L-VSI in the front end. Even though the number of the switches is not reduced, fundamental frequency switching minimizes the switching power losses and creates a room for more efficient and compact design with low cost. The system performance has been analyzed both theoretically and using

simulation studies on the regenerative CHB drive Matlab/Simulink model with regenerative FOC controlled motor load.

- Application of the proposed FFE controller in conjunction with the proposed reduced switch-count CHB configuration. Theoretical analysis of the system is provided along with simulation studies on a regenerative CHB drive in Matlab/Simulink. The proposed solution shows outstanding performance and efficiency resulting from merging both switch-count reduction with switching frequency minimization.
- Experimental implementation of a reconfigurable scaled-down version of a regenerative CHB motor drive along with front end and drive output controllers.
- Experimental validation of the proposed reduced switch-count configuration using preliminary results from the developed setup in STATCOM operation.

1.4 Thesis Structure

The thesis is structured as follows:

Chapter 2 provides a detailed overview of the cascaded H-bridge motor drives. The aim of this chapter is to present the necessary details needed for the understanding of the presented work, and to point out the challenges accompanying the conventional regenerative CHB drives.

Chapter 3 provides a comprehensive literature review of the existing reduced switch-count regenerative CHB topologies. Many issues are associated with these topologies as they are based on single-phase AFEs. To address these issues, potential reduced switch-count configurations based on three-phase AFEs are discussed.

Chapter 4 goes into depth of the selected proposed reduced switch-count configuration based on four-switch three-phase inverter (FSTPI) AFE. Detailed analysis

of the FSTPI, its standalone operation, and the resulting challenges is provided. Two proposed methods are presented to overcome these challenges. Simulation studies on a developed model for regenerative CHB drive are provided to validate the theoretical analysis.

Chapter 5 provides a brief review on the modulation techniques used in AFEs and their associated power losses. After that, the fundamental frequency ends (FFEs) are introduced and their different controllers and challenges are thoroughly discussed. A new FFE controller approach is proposed in this chapter to overcome the challenges of the existing controllers. The performance of the proposed controller is verified through simulation studies in Matlab/Simlink.

Chapter 6 presents the application of 2L-VSI FFEs in regenerative CHB motor drives using the proposed controller in Chapter 5. Another step further presented in this chapter is to combine the reduced switch-count configuration, proposed in chapter 4, and switching power losses reduction by employing FSTPI FFEs in regenerative CHB motor drives. Both approaches' performances have been analyzed theoretically and using simulation studies of the developed model of regenerative CHB drive.

Chapter 7 discusses the experimental implementation of a scaled-down version of a 7-level regenerative CHB drive. The developed system is reconfigurable and is meant to verify the proposed methods throughout the thesis. Experimental validation of the proposed reduced switch-count configuration is presented in this chapter. The experimental validation of the proposed FFE controller is considered in the future work.

The last chapter, chapter 8, concludes the thesis. Summary of the presented work, its main contributions, and future work are provided.

Chapter 2

Cascaded H-Bridge (CHB) Medium-Voltage (MV) Drives

2.1 Structure of CHB MV Drive

The general structure block diagram of the typical CHB MV drive is shown in Fig. 2.1(a) [8]. It comprises a phase shifting transformer and multiple low voltage basic building blocks called “Power Cells”.

The phase-shifting transformer serves the following purposes [8]:

- Stepping down the input voltage to a value suitable for the power cell.
- Mitigation of the common mode voltage stress. Therefore, standard motors’ isolation can be used.
- Providing the electrically isolated input voltages needed for each cell.

- Compliance with the grid standards in the input side by cancellation of the input current low order harmonics.

The details of the typical non-regenerative CHB power cell are shown in Fig. 2.1(b). It comprises three stages [2]:

a) *Rectification:* the cell input three-phase voltage is rectified through a three-phase diode rectifier. Each cell is fed through a secondary winding from the phase-shifting transformer.

b) *Energy Storage*: an intermediate DC-link capacitor stores the energy during operation and smooths the voltage ripples.

c) *Inversion:* a single-phase H-bridge is employed in the output stage to deliver the required voltage and frequency.

The power cells' low voltage outputs are connected in series to synthesize medium voltage with low harmonic distortion. *N* cells per phase generate (2*N*-1) phase-to-neutral voltage levels. The number of the cascaded cells is mainly determined by the desired output voltage, harmonic content, and cost [2]. In practice, the number of power cells ranges from 9 cells for 2.3 kV to 27 cells for 11 kV as shown in Table 2.1.[2], [8].

TABLE 2.1. TOTAL NUMBER OF CHB POWER CELLS FOR DIFFERENT OUTPUT VOLTAGES [8].

Output Voltage (kV)	Total Number of CHB Power Cells
2.3 / 2.4 / 3 / 3.3	9
4 / 4.16	12
6	15
6.3 / 6.6 / 6.9	18
10	24
11	27

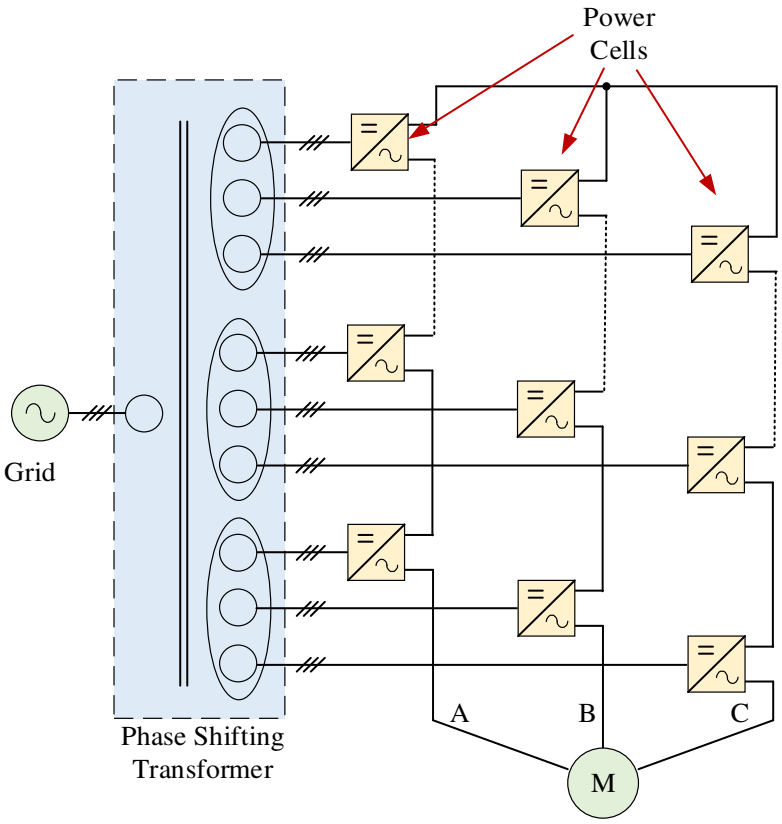

(a) CHB MV Drive Block Diagram.

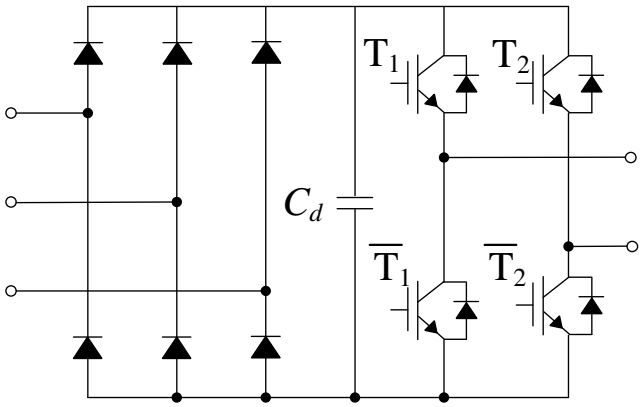

(b) Typical Non-Regenerative CHB Power Cell.

Fig. 2.1. Typical CHB MV Motor Drive Structure [2].

2.2 Harmonic Cancellation using Phase-Shifting Transformers

Due to the application of diode rectifier in each cell input, odd non-triplen low order harmonics are present in the cells' input currents. If ordinary multi-winding transformer is used, these harmonics will be reflected in the primary side. To overcome this issue, multi-pulse phase-shifting transformers are employed [2], [8].

The concept of phase-shifting transformer can be illustrated by the example of the Δ/Z-1 configuration and phasor diagram shown in Fig. 2.2 [2], where the phase shift between the secondary and primary voltages is an arbitrary angle δ and is given by:

$$|\delta| = \angle\overline{V_{ab}} - \overline{V_{AB}} \tag{2.1}$$

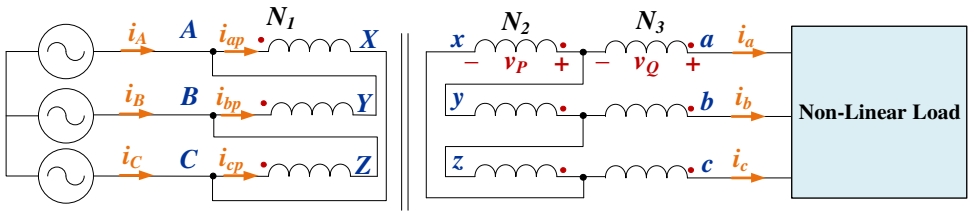

(a) Connection Diagram.

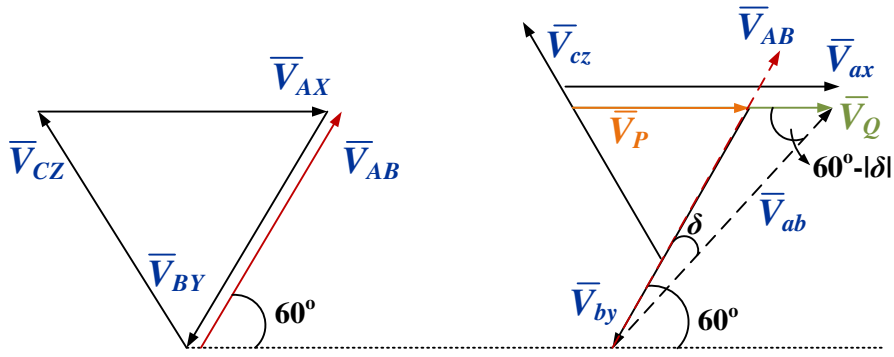

(b) Phasor Diagram.

Fig. 2.2. Δ/Z-1 Phase-Shifting Transformer [2].

By analysis of the phasor diagram in Fig. 2.2(b), the turns ratios are given by [2]:

$$\frac{N_3}{N_2+N_3}=\frac{\sin(|\delta|)}{\sin(60^o-|\delta|)}$$
$$\frac{N_1}{N_2+N_3}=\frac{\sqrt{3}}{2\sin(60^o-|\delta|)}\frac{V_{AB}}{V_{ab}} \quad (2.2)$$

From (2.2), there are two extreme scenarios [2]:

- Reduction of N_2 to zero, which will lead to a Δ/Y configuration with δ=-30°.
- Reduction of N_3 to zero, which will lead to a Δ/Δ configuration with δ=0°.

Considering the first scenario of Δ/Y configuration with unity voltage ratio (V_{AB}/V_{ab}) to supply a nonlinear load, then the secondary line currents are given by:

$$i_a=\sum_{n=1,5,7,11..}^{\infty} I_n \sin(n(\omega t-30^o-\phi))$$
$$i_b=\sum_{n=1,5,7,11..}^{\infty} I_n \sin(n(\omega t-30^o-\phi-120^o)) \quad (2.3)$$
$$i_c=\sum_{n=1,5,7,11..}^{\infty} I_n \sin(n(\omega t-30^o-\phi+120^o))$$

, where I_n is the peak value of the harmonic order n, and ϕ is the angle phase shift between the secondary load line currents and secondary phase voltages.

Referring the secondary currents to the primary side, the phase primary currents are expressed by:

$$i_{ap}=i_a\frac{N_2}{N_1}=\frac{1}{\sqrt{3}}\sum_{n=1,7,13,..}^{\infty} I_n \sin(n(\omega t-\phi-30^o))$$
$$i_{bp}=i_b\frac{N_2}{N_1}=\frac{1}{\sqrt{3}}\sum_{n=1,7,13,..}^{\infty} I_n \sin(n(\omega t-\phi-30^o-120^o)) \quad (2.4)$$
$$i_{cp}=i_c\frac{N_2}{N_1}=\frac{1}{\sqrt{3}}\sum_{n=1,7,13,..}^{\infty} I_n \sin(n(\omega t-\phi-30^o+120^o))$$

By applying Kirchhoff's current law, the primary line currents for point *A* are:

$$i_A = i_{ap} - i_{bp} = \sum_{n=1,7,13,..}^{\infty} I_n \sin(n(\omega t - \phi - 30^o) + 30^o) + \sum_{n=5,11,17,..}^{\infty} I_n \sin(n(\omega t - \phi - 30^o) - 30^o) \quad (2.5)$$

(2.5) can be generalized for any phase-shifting transformer with phase-shifting angle δ to become [2]:

$$i_A = i_{ap} - i_{bp} = \sum_{n=1,7,13,..}^{\infty} I_n \sin(n(\omega t - \phi + \delta) - \delta) + \sum_{n=5,11,17,..}^{\infty} I_n \sin(n(\omega t - \phi + \delta) + \delta) \quad (2.6)$$

From (2.6), for the primary current in a general phase-shifting transformer [2]:

- The positive sequence harmonics line currents angles are given by:

$$\angle i_{An} = \angle i_{an} - \delta = -n\phi + n\delta - \delta \quad \text{for } n = 1,7,13,\ldots \quad (2.7)$$

- The negative sequence harmonics line currents angles are given by:

$$\angle i_{An} = \angle i_{an} - \delta = -n\phi + n\delta + \delta \quad \text{for } n = 5,11,17,\ldots \quad (2.8)$$

Consequently, for a phase-shifting transformer, with *k* secondary winding groups feeding *k* non-linear loads, the phase-shifting angle for each secondary group (δ_k) can be selected such that certain harmonics summation in the primary side is equal to zero and thus cancelled.

In case of CHB MV drives, the phase-shifting transformer is feeding 6-pulse diode rectifiers in each cell. Typically, the secondary winding groups are designed to be shifted from each other by ($60^o/m$), where *m* is the number of cells in each phase. This technique can cancel harmonics of orders equal to $6i \pm 1$, where *i* is an integer not multiple of *m* [2], [8].

2.3 Motor Side Modulation Techniques

2.3.1 H-Bridge SPWM Modulation Schemes

Sinusoidal pulse-width modulation (SPWM) is the most common modulation technique for CHB drive output voltage. For the power cell output single-phase H-bridge inverter, shown in Fig. 2.3, SPWM can be bipolar or unipolar [2].

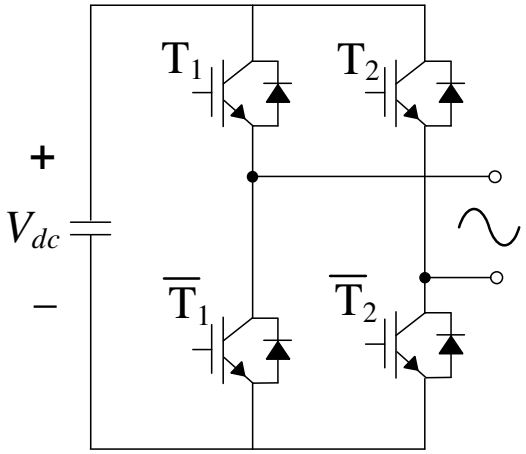

Fig. 2.3. Single-Phase H-bridge Inverter.

In bipolar SPWM, one sinusoidal modulation waveform is compared with a triangular carrier signal to generate the gating signals for the two upper switches (T_1 and T_2) in each power cell. The switches in the same leg are switched complementarily. The scheme waveforms for the H-bridge inverter are shown in Fig. 2.4. The H-bridge inverter switching frequency is equal to the carrier switching frequency. Therefore, the resulting output voltage harmonic spectrum contains harmonic sidebands centered around the carrier switching frequency and its multiples. The output voltage varies between the positive and negative values of the DC-link voltage ($\pm V_{dc}$) in each half cycle [2].

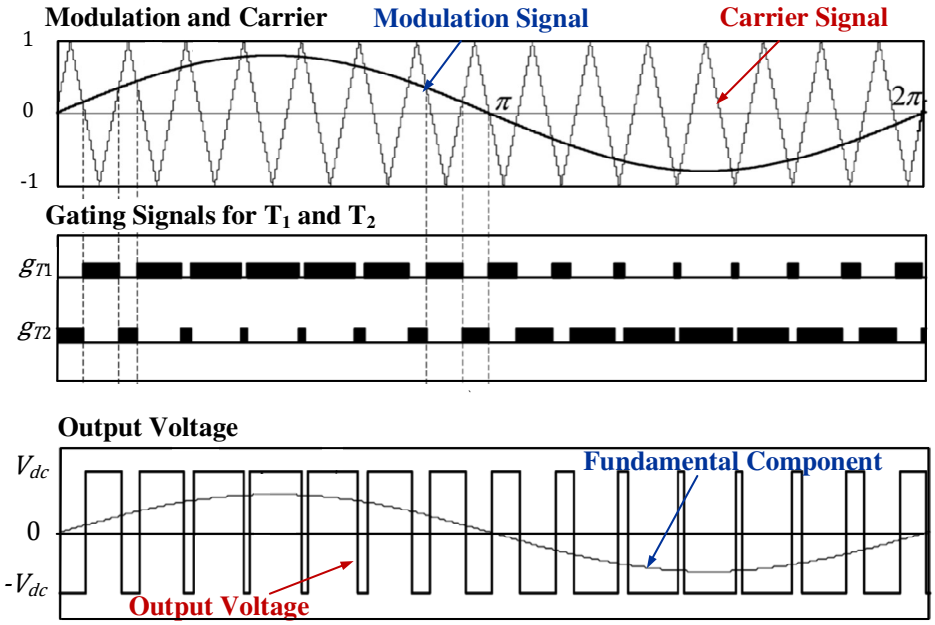

Fig. 2.4. Bipolar Modulation Scheme Waveforms [2].

Fig. 2.5 shows one implementation method for the unipolar PWM scheme. Two sinusoidal modulation waveforms are compared with one triangular carrier signal. The two modulating signals are out of phase by 180°. Each comparison resulting gate signals are responsible for switching one leg of the H-bridge. In each half cycle, the output waveform varies between with zero and $+V_{dc}$, or zero and $-V_{dc}$. In this scheme, the effective inverter switching frequency is double the carrier switching frequency. Therefore, the harmonic spectrum of the output voltage contains sideband harmonics around even multiples of the carrier frequency. Another implementation for the unipolar PWM scheme can be achieved by comparing two carrier signals of 180° phase shift with one modulating signal.

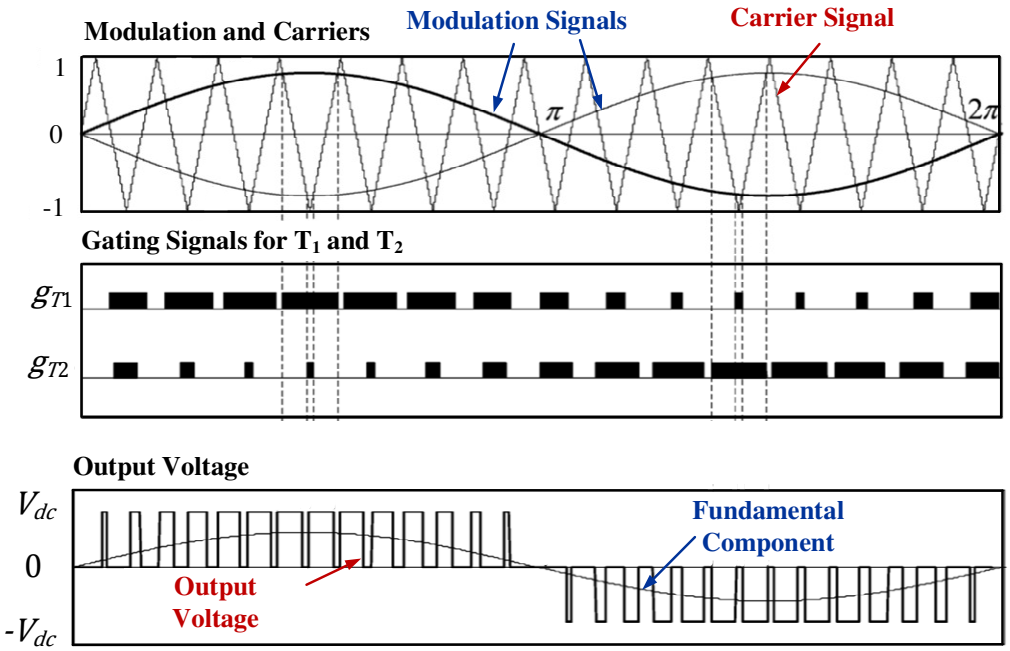

Fig. 2.5. Unipolar Modulation Scheme Waveforms [2].

2.3.2 Carrier Shifting Schemes

In CHB MLI with *m*-cell per phase, 2*m* carriers are used in the phase cells to obtain (2*m*+1) level output phase voltage. These carriers are shifted from each other, either in phase or levels or both, to synthesize the required voltage in a stepped waveform and improve its harmonic content [2].

a) Phase-Shifted Multi-Carrier Scheme (PS-PWM):

In this method, all the carriers have the same unity magnitude and same frequency, but phase-shifted from each other by $360^{o}/_{2m}$. It should be noted that each two adjacent legs' carriers are phase-shifted by 180°. Therefore, the phase-shifted PWM is in essence a unipolar modulation. The devices' switching frequencies are equal to the carrier switching frequency ($f_{sw,carrier}$).

The whole multilevel inverter switching frequency ($f_{sw,inverter}$) can be expressed in terms of the carrier switching frequency ($f_{sw,carrier}$) by [2]:

$$f_{sw,inverter} = 2m * f_{sw,carrier} \tag{2.9}$$

b) Level-Shifted Multi-Carrier Scheme (LS-PWM):

This scheme employs carriers of same frequency and magnitude of $1/2m$. The carriers are level-shifted so that they occupy continuous sections.

There are three main types of LS-PWM [2]:

- In-Phase Disposition (IPD), where all the carriers have the same phase shift. This method provides the best harmonic performance.
- Alternative Phase Opposite Disposition (APOD) method, where the carriers are out-of-phase in alternative fashion.
- Phase Opposite Disposition (POD), where the carriers above zero level are out of phase from the carriers below the zero level.

Due to level-shifting of carriers, the devices' switching frequencies are not equal neither to each other nor to the carrier frequency. Generally, the inverter switching frequency of this scheme is equal to the carrier frequency. Accordingly, the average device switching frequency ($f_{sw,device(avg)}$) can be given by:

$$f_{sw,device(avg)} = \frac{f_{sw,carrier}}{2m} \tag{2.10}$$

Unequal devices' switching frequencies are also accompanied by unequal conduction time and power loss sharing between the devices. Therefore, it is very important to rotate the switching gates between different cells to distribute the devices loading equally.

As the total inverter switching frequency in LS-PWM is equal to the carrier frequency, the carrier frequency should be increased to have the same inverter switching frequency as PS-PWM. The average device switching frequency in both schemes remains equal. However, the voltage total harmonic distortion using LS-PWM is lower than that of PS-PWM [2].

2.4 Motor Side Control Techniques

Motor speed and torque can be controlled by various control schemes. Two of the most popular schemes are scalar speed control and vector field oriented control (FOC) [2], [22]-[24].

2.4.1 Scalar Speed Control

This technique is also known as Voltage/Frequency (*v/f*) or Volt/Hertz control [22]-[24]. The output voltage and frequency magnitudes are controlled together such that their ratio remains constant and thus the motor flux is kept constant to avoid saturation or loss of flux. This relation is based on the general induced voltage equation of AC-machines, which is approximated to be equal to the output voltage given by [22]-[24]:

$$E_{ph} = 4.44 * k * p * f * \varphi \tag{2.11}$$

, where E_{ph} is the maximum induced phase voltage, k is the coil constant, p is the number of pole-pairs, f is output electrical frequency, and φ is air gap flux.

The optimal *v/f* ratio is determined by the rated operation conditions. This control method is mainly open-loop as shown in the block diagram in Fig. 2.6(a). The only input is the desired speed (N_{ref}) which sets the reference frequency and thus the required voltage, while the torque is mainly dictated by the load.

Scalar control main advantages are simplicity of implementation, low cost, and immunity to feedback signals errors. However, this comes at the cost of steady state error, poor dynamic performance, non-controllability of the magnetic flux, and torque oscillations. This type of control is suitable for loads such as fans, pumps, mixers, and grinders where the control accuracy is not important [22]-[24].

A better steady state performance can be achieved by implementing closed-loop *v/f* control through having a speed feedback signal as shown in Fig. 2.6(b) [22]-[24]. Nevertheless, the sluggish dynamic performance and uncontrolled magnetic flux remain the main disadvantages of the scalar control. To overcome these issues vector control techniques were introduced.

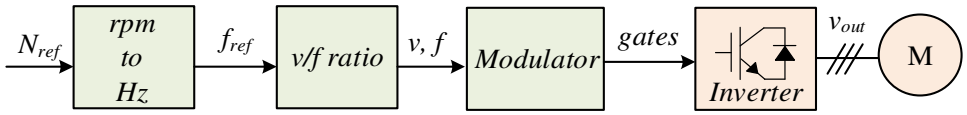

(a) Open-loop v/f control scheme.

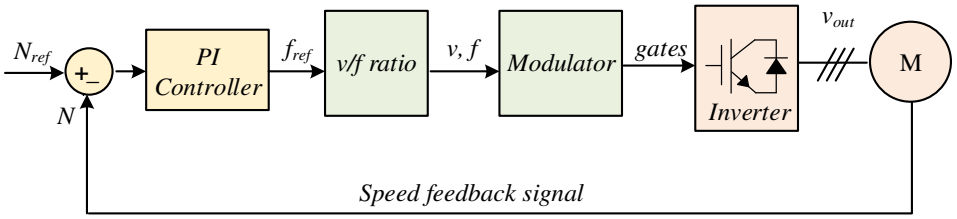

(b) Closed-loop v/f control scheme.

Fig. 2.6. Scalar Speed Control Schemes [22]-[24].

2.4.2 Vector Field-Oriented Control (FOC)

The idea behind this method is to mimic the DC machine control, which have two independent currents (armature and field) to control magnetic flux and torque separately [2], [22]-[24]. In AC machines, the stator current carries both the torque and flux current components together. In the stationary *abc*-reference frame, these two components are highly coupled in one single AC component, the stator current vector i_s. Obtaining

decoupled DC current components can be achieved through using the *d-q* reference frame which is rotating with the same angular frequency (ω) as the stator current as shown in Fig. 2.7.

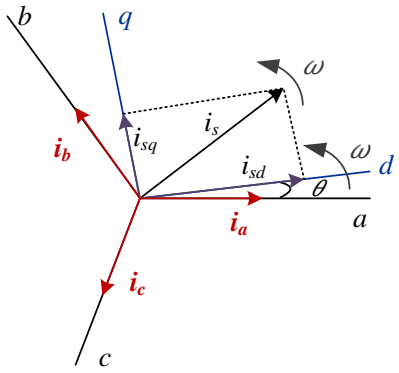

Fig. 2.7. Stator Current Vector in Stationary and Rotating Frames.

The following *abc/dq*0 transformation is applied on the three-phase time-varying components to obtain the two separate DC components in the *d-q* reference frame, the zero component does not exist for a balanced three-phase system [2]:

$$\begin{bmatrix} x_d \\ x_q \\ x_0 \end{bmatrix} = \frac{2}{3} \begin{bmatrix} \cos(\theta) & \cos\left(\theta - \frac{2\pi}{3}\right) & \cos\left(\theta + \frac{2\pi}{3}\right) \\ -\sin(\theta) & -\sin\left(\theta - \frac{2\pi}{3}\right) & -\sin\left(\theta + \frac{2\pi}{3}\right) \\ \frac{1}{2} & \frac{1}{2} & \frac{1}{2} \end{bmatrix} \begin{bmatrix} x_a \\ x_b \\ x_c \end{bmatrix} \tag{2.12}$$

The induction machine rotor flux (λ_r) and electromagnetic torque (T_e) in *d-q* frame are given by [2]:

$$\begin{aligned} \overline{\lambda_r} &= \lambda_{dr} + j\lambda_{qr} \\ \lambda_{dr} &= L_{lr} i_{dr} + L_m (i_{ds} + i_{dr}) \\ \lambda_{qr} &= L_{lr} i_{qr} + L_m (i_{qs} + i_{qr}) \end{aligned} \tag{2.13}$$

$$T_e = \frac{3}{2L_r} (i_{qs}\lambda_{dr} - i_{ds}\lambda_{qr}) \tag{2.14}$$

, where λ_{dr} and λ_{qr} are the rotor flux *d* and *q* components, i_{ds} and i_{qs} are the stator current *d* and *q* components, i_{dr} and i_{qr} are the rotor current *d* and *q* components, L_{lr} is the rotor leakage inductance, L_m is the mutual inductance, and L_r is the rotor self-inductance.

In FOC, the *d*-axis component is usually chosen to align with the rotor flux (λ_r) orientation [2]. In this case, the transformation angle θ is the rotor flux angle θ_{fr}. Consequently,

$$\begin{aligned} \lambda_{dr} &= \lambda_r \\ \lambda_{qr} &= 0 \end{aligned} \tag{2.15}$$

By substitution with (2.15) in (2.13) and (2.14), it is shown that the rotor flux is now controlled by stator current *d*-component, while the electromagnetic torque is controlled by the stator current *q*-component. Thus, both variables are controlled independently.

Based on the method used to determine the rotor flux angle, the FOC method is classified into two categories, direct FOC and indirect FOC [2]:

- In direct FOC, θ_{fr} is obtained directly through flux sensors, or from measured terminal voltage and current.
- In indirect FOC, θ_{fr} is calculated through addition of the detected rotor position angle and the calculated slip angle.

The general block diagram for FOC scheme is shown in Fig. 2.8 [2]. Reference speed (N_{ref}) is used to set the required torque ($T_{e\text{-}ref}$) and flux (λ_{r-ref}). The reference torque sets the reference *q*-axis current (i_{qs-ref}) while the reference flux is used to set

the reference *d*-axis current (i_{ds-ref}). The feedback signals of line currents are transformed using the calculated rotor flux angle (directly or indirectly) from *abc* to *d-q* frame. The measured *d-q* currents are then compared with the reference currents to produce the required PWM modulation signals through the torque and flux controllers.

The advantages of this method include good torque response, good dynamic performance, indirect control of torque, and accurate control of speed. However, the need for feedback signals, more complex implementation, and higher cost are the main challenges of this method [22]-[24].

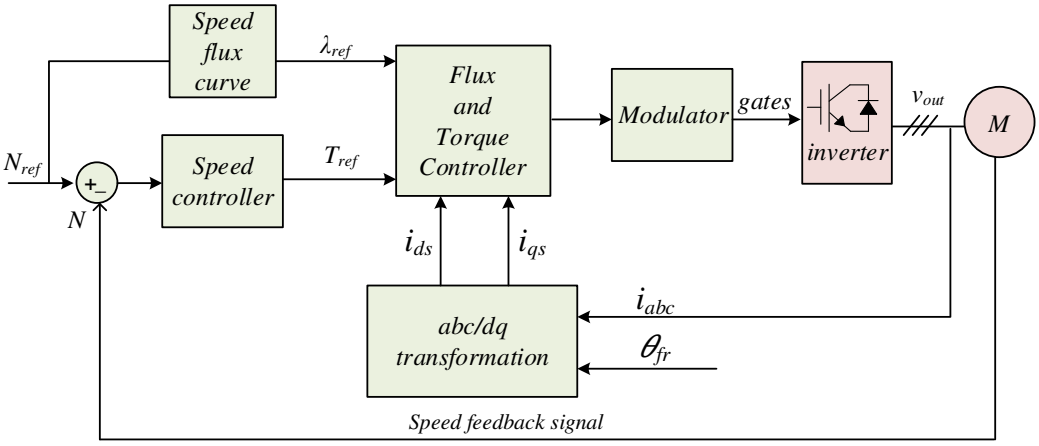

Fig. 2.8. Field Oriented Control General Control Scheme [2].

2.5 Regenerative CHB Motor Drives

The unprecedented increase in the world demand for energy resources is accompanied by threatening side effects of climate change and global warming. In the International Energy Agency (IEA) report [25], energy production is found to be the main contributing factor to the greenhouse emissions. One way to minimize these effects is by increasing the efficiency of the electrical systems.

Many industrial applications, with loads that can overhaul the motor such as downhill conveyors, centrifuges, elevators, and forklifts, or loads characterized by very

high inertia such as fans, can operate in braking or regenerative modes [1]. During these modes, the energy is regenerated from the motor to the grid side. This energy must be directed away from the DC-link to avoid overvoltage failures. The typical solution in the typical non-regenerative cell, Fig. 2.1(b), is to dissipate this energy in every cell as heat in a resistor load through a controlled chopper as shown in Fig. 2.9 [12]. This approach lowers the drive efficiency, and increases the system's cooling costs, size, and carbon footprint.

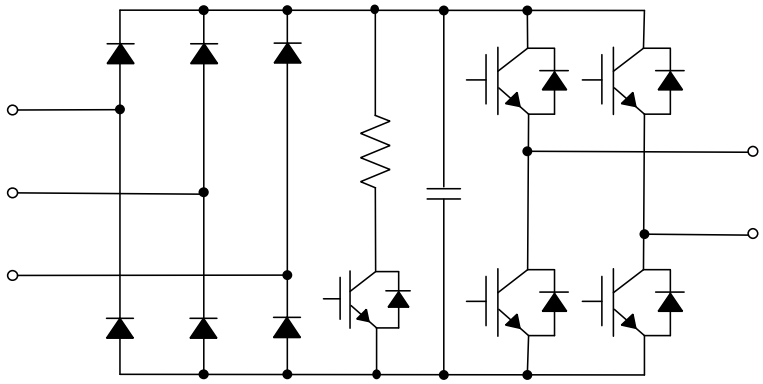

Fig. 2.9. Dissipation of Braking Energy in Resistor through Chopper [12].

With these two previous points in mind, capturing and utilizing this energy from regenerative loads can be very advantageous. In order to achieve this, bidirectional power flow must be allowed between the motor and the grid sides. This way, the regenerated energy can be fed back to the grid or stored to be used by the load later. Motor drives that allow this type of energy flow are called "Regenerative Motor Drives". Typically regenerative motor drives depend on the replacement of uncontrolled passive diode front ends (DFEs) with controlled active front ends (AFEs).

2.5.1 Conventional Regenerative CHB Power Cell

Fig. 2.10 shows the conventional regenerative CHB power cell introduced in [12]-[14]. The three-phase uncontrolled rectifier is replaced by a PWM-controlled 2L-VSI, and three inductors are used as input filters. The cell configuration allows bidirectional power flow between the motor and the grid, and provides reactive power compensation. The phase-shifting transformer can now be replaced by a simpler multi-winding transformer since the low order harmonics do not exist any longer. The DC-link voltage in this cell is fully controlled during motoring and regeneration. Moreover, high switching frequency of the AFE helps in reducing the ripples on the DC-link capacitor [12]-[14].

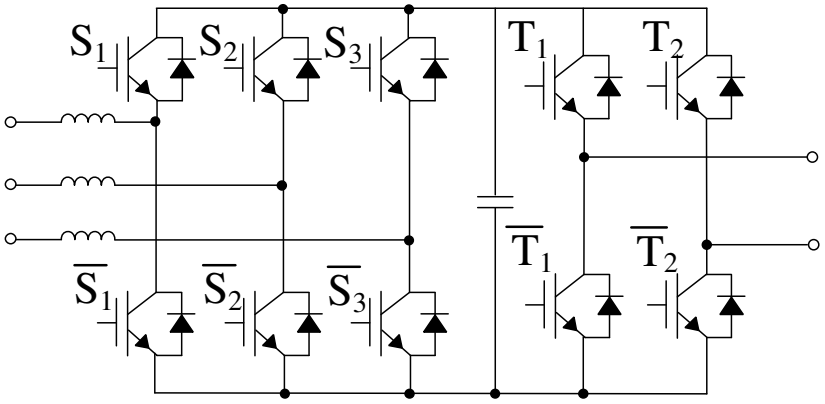

Fig. 2.10. Conventional Regenerative CHB Power Cell [12]-[14].

2.5.2 AFE Side Control

The typical AFE control scheme block diagram is shown in Fig. 2.11. It comprises two control loops: DC-link voltage controller, and current controller [13].

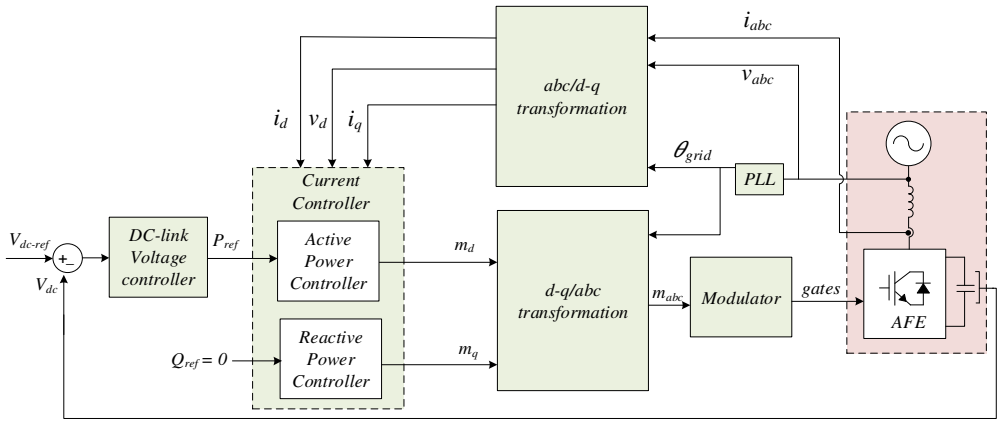

Fig. 2.11. 2L-VSI AFE Control Block Diagram [13].

The DC-link voltage controller regulates the DC-link voltage value to match the reference voltage value. It sets the reference active power value and direction. The reactive power reference is usually set to zero for unity power factor operation. The two power components reference values are fed as the input to the current control loop.

The current control loop is based on the voltage oriented control (VOC) in *d-q* reference frame. The active (*P*) and reactive (*Q*) powers for a balanced system in *d-q* frame are given by [13]:

$$P = \frac{3}{2}(v_d i_d + v_q i_q)$$
$$Q = \frac{3}{2}(v_q i_d - v_d i_q) \tag{2.16}$$

, where v_d and v_q are the grid voltage *d* and *q* components, and i_d and i_q are the cell input current *d* and *q* components.

Following the same decoupling concept as in FOC scheme, the transformation in (2.12) is applied on the measured grid voltage and the line currents. v_d is aligned with the grid voltage by using the grid voltage angle as the transformation angle, while v_q is set to zero. A phase-locked loop (*PLL*) is needed to estimate the grid angle.

Consequently, from (2.16), i_d controls the active power, while i_q controls the reactive power. The AFE current controller tracks the *d-q* current components to match the reference values by setting the desired modulation signals components (m_d and m_q) in *d-q* frame. The *d-q* modulation signals goes through the *d-q*/*abc* transformation. The result is three-phase modulation signals (m_{abc}) which are fed to the modulator to generate the required gating signals to the 2L-VSI inverter.

2.5.3 Challenges

The conventional regenerative CHB motor drives have many challenges which hinder both their practical and economic viability:

- The conventional regenerative power cell contains ten IGBT switches, which increases the cell cost and dimensions.
- Since each switch needs a gate-driving circuit, the control hardware implementation becomes more complex and inconvenient.
- The increase of the switches' number also affects the system reliability, as the failure probability becomes higher.
- AFE switches' power losses call for more advanced heat sink design, which affects both the cost and the size of the power cell.
- Unlike the non-regenerative CHB drive, the conventional regenerative CHB drive uses more switches than NPC and FC regenerative topologies. For instance, to generate five levels per phase, conventional regenerative CHB drive will use twenty switches for each phase (2 cells per phase), while regenerative back-to-back NPC will use only 16 switches per phase as shown in Fig. 2.12 [26].

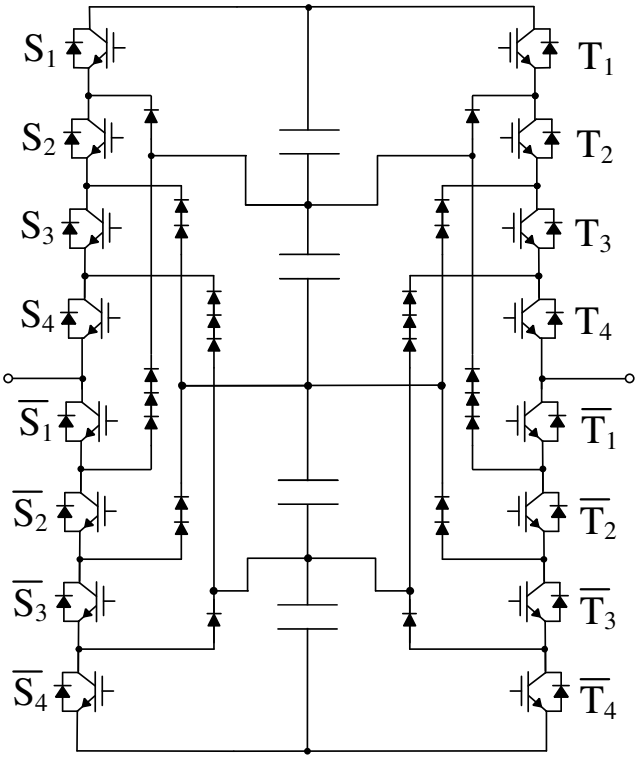

Fig. 2.12. Regenerative Five-Level NPC Phase Leg [26].

2.6 Approaches for more economic regenerative CHB drives.

To make use of the CHB configuration full potentials in regenerative applications, developing more practical and economic versions of regenerative CHB drives has become one the hottest motor drives research topics [14]-[21].

Many approaches are adopted to achieve this goal which can be classified into two main categories:

- *Architecture*: includes research of reduced switch-count topologies to optimize the cell design from architecture point of view [15]-[20].
- *Control*: includes employing new control techniques to optimize the cell performance and efficiency [14], [21].

The presented work in the following chapters addresses both the architecture and control aspects:

- The existing reduced switch-count topologies will be reviewed in Chapter 3 and a novel reduced switch-count regenerative power cell is proposed with thorough analysis in chapter 4.
- A new control scheme for switching the front end with fundamental frequency is provided to minimize the switching power losses and increase the cell efficiency in chapters 5 and 6.

2.7 Summary

To construct the necessary background for this work, a review of the typical CHB motor drive structure and modulation along with different schemes for motor control are reviewed. Additionally, harmonic cancellation concept in phase-shifting transformer is briefly provided as it will be used in some parts of this thesis.

The conventional regenerative CHB motor drive and its control are discussed in addition to the challenges associated with the increase of its number of switches. The discussion illustrated the importance of researching more economic versions of regenerative CHB motor drives. On the basis of that, two approaches were chosen as the main directions in the next chapters: switch-count reduction, and minimizing the front end switching frequency.

Chapter 3

Reduced Switch-Count Regenerative CHB Power Cells

3.1 Introduction

Switch-count reduction of regenerative CHB power cells has become an active research area as one approach to increase their reliability, efficiency, and practical implementation, and reduce their cost and complexity [15]-[19].

In order to have a reduced switch-count power cell configuration that is able to replace the conventional regenerative power cells, the following aspects should be

considered to reach the best compromise [15]-[19]:

- Grid interface transformer design, i.e. the possibility to use existing transformer configuration without having a new design.
- Ease and simplicity of active front end (AFE) control scheme implementation.
- DC-link voltage ripples.
- Compliance with the grid connection standards.
- Good dynamic performance.
- Stability against grid side disturbances – e.g. voltage sag and voltage unbalance.
- Reactive power compensation capability.
- Switches current and voltage ratings.

In literature, three regenerative CHB power cells with reduced switch-count configurations were proposed based on single-phase active front ends [15]-[19]. Single-phase interfaces pose many limitations to replace the conventional regenerative power cell. Therefore, reduced switch-count configurations based on three-phase interfaces are advantageous. As CHB cells are of low voltage ratings, possible power cell configurations with three-phase interface and lower number of switches can be adopted from the low-cost low-voltage drives.

Fig. 3.1 shows the discussed configurations in this chapter. The three existing reduced switch-count power cells based on single-phase AFEs are reviewed. Additionally, two power cell configurations based on reduced switch-count three-phase AFEs are presented as potential configurations. One of these two configurations is selected to move forward with as the proposed solution in this thesis.

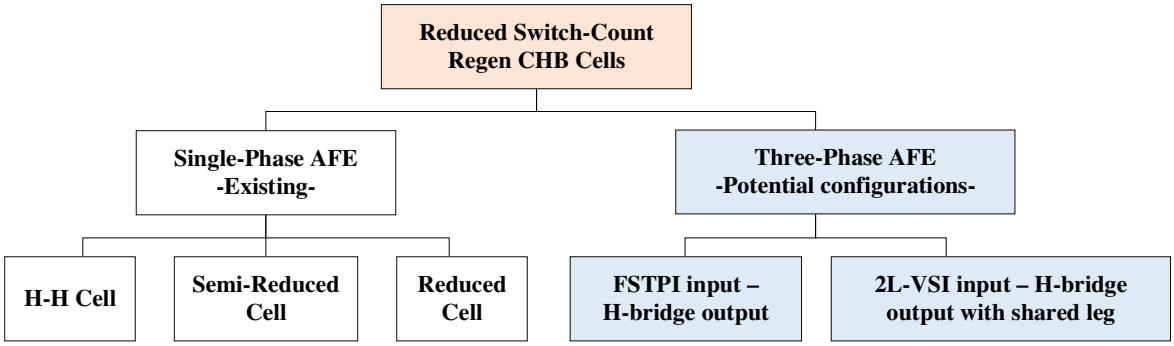

Fig. 3.1. Classification of Cells Configurations with Reduced Switch-Count.

3.2 Existing Reduced Switch-Count Power Cells

3.2.1 H-Bridge Input H-Bridge Output (H-H) Power Cell

a) Power Cell Structure

This power cell configuration, shown in Fig. 3.2, was proposed in [15]. A single-phase full bridge (H-bridge) controlled rectifier is used in the active front end as well as the cell output. As a result, total of eight switches is used in each power cell instead of ten switches. The cell is connected to the grid side through a single phase transformer and grid-tying filter. The modulation and control of the output inverter does not change from that in the typical CHB power cell [15]. Thus, the focus will be on the working principle, modulation, and control of the AFE.

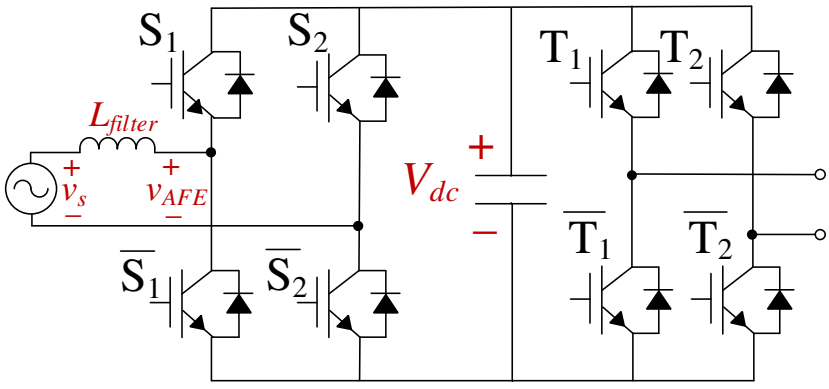

Fig. 3.2. H-H Cell Power Cell Configuration. [15]

b) AFE Working Principle

- *AFE Modulation*

The modulation of the AFE side H-bridge inverter can be realized using either bipolar or unipolar SPWM techniques. Unipolar modulation is preferred since the output of the controlled rectifier to the grid side will have three levels switching between $+V_{dc}$, 0, and $-V_{dc}$, where V_{dc} is the average DC-link voltage, resulting in lower current distortion than having two voltage levels [15].

- *AFE Governing Equations*

For the H-bridge AFE shown in Fig. 3.2, there are four possible switching states [19]. The switching conditions for each state are illustrated in Table 3.1, where the two switches in the same leg are complementary. Fig. 3.3 shows the three equivalent circuits resulting from the four corresponding switching states.

The filter inductor voltage (v_L) is expressed by [19]:

$$v_L = L_{filter}\frac{di_s}{dt} = v_s - v_{AFE} = v_s - kV_{dc} \tag{3.1}$$

, where i_s is the cell input current, L_{filter} is the filter inductance, k is a switching state constant which can be 1, 0, or -1.

TABLE 3.1. H-BRIDGE AFE SWITCHING STATES AND OUTPUT VOLTAGE.

State Number	S_1	S_2	v_{AFE}
I	1	0	$+V_{dc}$
II	1	1	0
III	0	0	0
IV	0	1	$-V_{dc}$

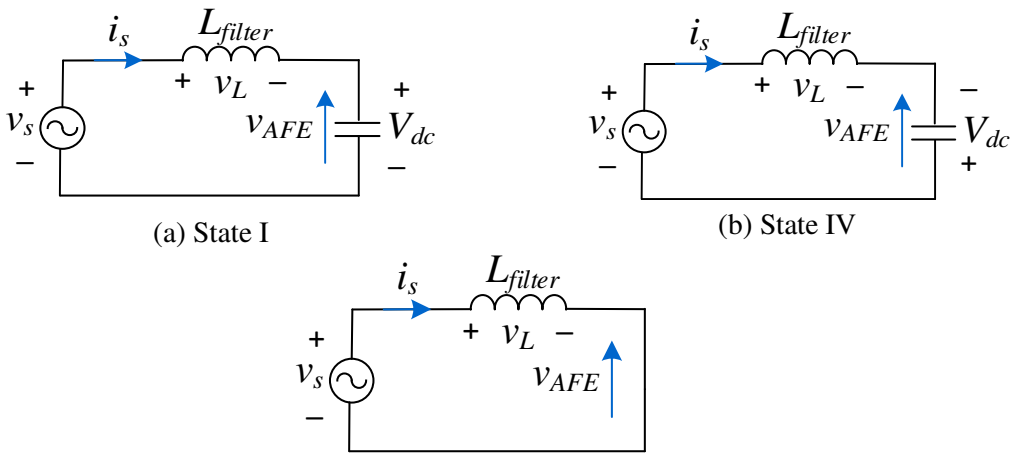

(a) State I

(b) State IV

(c) States II and III.

Fig. 3.3. H-H Cell AFE Equivalent Circuit in Different Switching States [19].

Assuming the maximum input voltage to be V_s, from (3.1), if $V_{dc} > V_s$:

a) When k = 1 (state I), the voltage drop across the filter will be negative, and i_s will decrease.

b) When k = -1 (state IV), the filter voltage drop will be positive increasing the line current.

c) When k = 0 (states II and III), the current will depend on the input voltage v_{in}.

If, otherwise, $V_{dc} < V_s$, the current cannot be controlled. Instead the IGBT anti-parallel diodes will act as an uncontrolled rectifier to charge the DC-link voltage to V_s. Therefore, for stable and proper operation of the AFE, the DC-link voltage must be higher than the maximum of the cell input voltage.

c) DC-Link Ripples

For an H-bridge inverter, the single phase instantaneous power from the fundamental components is given by [15]:

$$\begin{aligned} p(t) &= V_1 \sin(\omega t) * I_1 \sin(\omega t - \varphi) \\ &= \frac{V_1 I_1}{2}\left(\cos\varphi - \cos(2\omega t - \varphi)\right) \end{aligned} \tag{3.2}$$

, where V_1 and I_1 are the maximum voltage and current, ω is the fundamental angular frequency, and φ is the phase shift between the voltage and current.

According to (3.2), the single phase power contains a pulsating component of double the inverter output fundamental frequency. In the H-H cell, these pulsating components will be injected to the DC-link from both the input and output side H-bridge converters. Therefore, the DC- link capacitor contains voltage ripples of double the input frequency ($2\omega_{in}$) and double the output frequency ($2\omega_o$).

d) Cell Input Current Harmonics

In addition to the switching frequency ripples resulting from the PWM scheme, two types of lower order harmonics exist in the input currents [15]:

- Due to the presence of output second order ripples on the DC-link, the input currents will be modulated by this ripple frequency. As a result, the input currents will contain lower order harmonics of ($\omega_{in} \pm 2\omega_o$). This is illustrated in the input currents spectrum in Fig. 3.4 [15], where the input frequency is 50 Hz and output frequency is 10 Hz.

- The second order input harmonic ripples ($2\omega_{in}$) on the DC-link are reflected in the cell input currents as third order harmonic ripples as shown in Fig. 3.4 [15]. In some applications, a notch filter is used in parallel to the DC-link to filter these ripples [15]

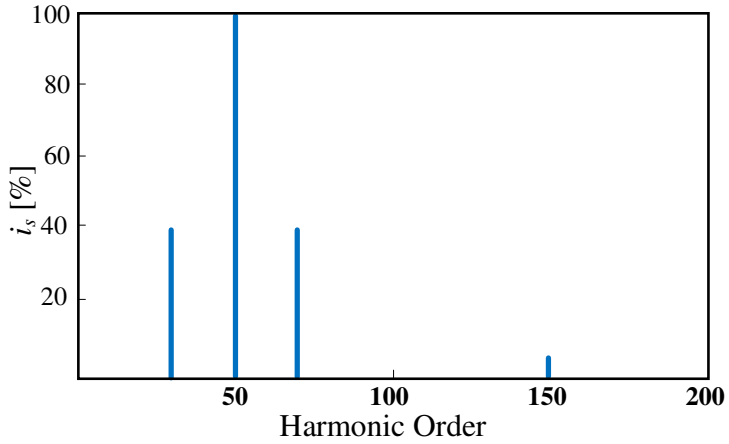

Fig. 3.4. H-H Cell Input Current Harmonic Spectrum
for Input Frequency of 50 Hz and Output Frequency of 10 Hz [15].

e) AFE Controller

The basic control scheme for the H-bridge AFE is shown in Fig. 3.5. It comprises a DC-link voltage control loop and current control loop [15], [19].

In the DC-link voltage controller block, the measured DC-link voltage (V_{dc}) is compared with the desired reference value ($V_{dc\text{-}ref}$) to set the required active power to regulate the DC-link voltage. The reference current amplitude ($\left|i_{s-ref}\right|$) is determined by the DC-link voltage controller. This amplitude must be multiplied by a sinusoidal waveform of the same phase and frequency as the input voltage (v_s) for unity power factor. Therefore, a single-phase PLL is required.

The current controller can be a hysteresis or linear controller [19]. It produces the required modulation to the modulator block which produces the firing gates to the AFE switches.

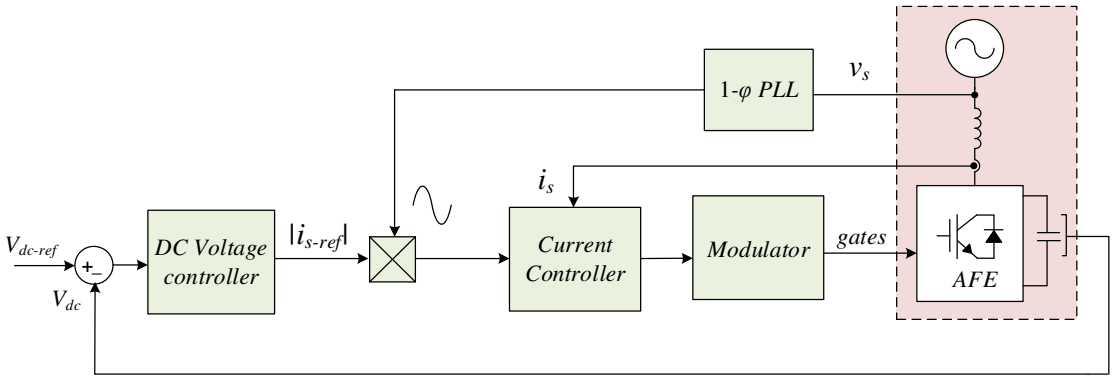

Fig. 3.5. Control Scheme Block Diagram for AFE in H-H Cell [15], [19].

f) Compliance with Grid Connection Standards

Elimination of low order harmonics of ($\omega_{in} \pm 2\omega_o$) is achieved by connecting three PWM rectifiers corresponding to different load phases to the same source through the secondary windings as illustrated in Fig. 3.6 [15].

The power supplied by arbitrary row *x* rectifier cell in each phase is:

$$
\begin{aligned}
p_{xA}(t) &= \frac{V_1 I_1}{2}\left(\cos\varphi - \cos(2\omega t - \varphi)\right) \\
p_{xB}(t) &= \frac{V_1 I_1}{2}\left(\cos\varphi - \cos(2\omega t - \varphi - \frac{2\pi}{3})\right) \\
p_{xC}(t) &= \frac{V_1 I_1}{2}\left(\cos\varphi - \cos(2\omega t - \varphi + \frac{2\pi}{3})\right)
\end{aligned}
\tag{3.3}
$$

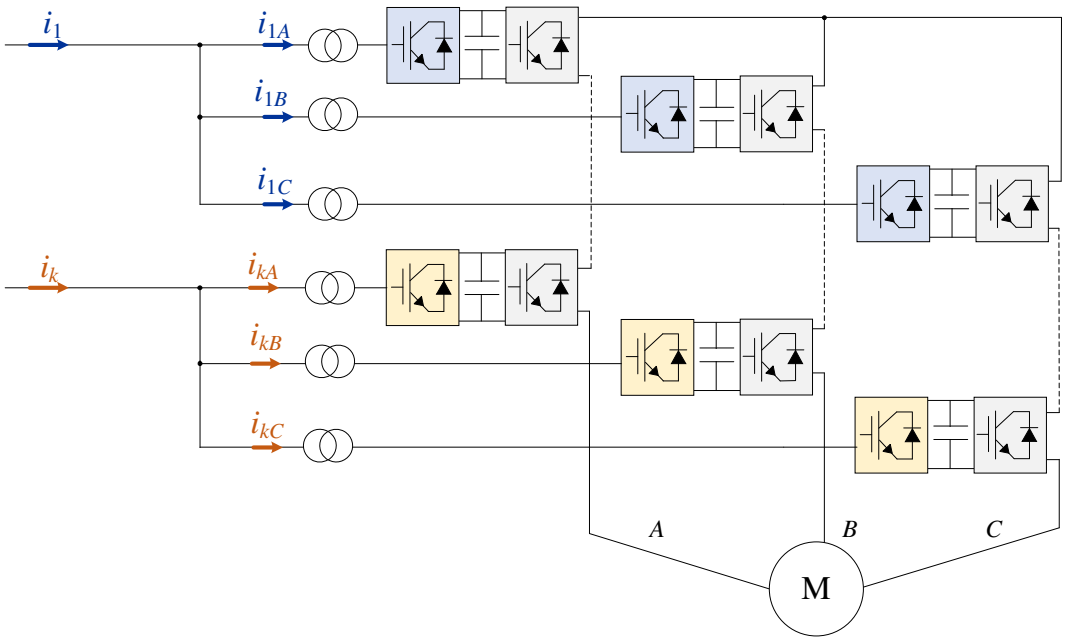

Fig. 3.6. Illustration of H-H Cells Parallel Connection for Low Order Harmonic Elimination from the Primary Currents [15].

From (3.3), it is clear that cell output pulsating power in different phases are phase shifted by 120° from each other. Consequently, the resulting ripples in the corresponding input currents of frequencies ($\omega_{in} \pm 2\omega_o$) will be displaced by the same phase shift. Due to the parallel connection through the secondary windings, the corresponding primary current for arbitrary row *x* is:

$$i_x = i_{xA} + i_{xB} + i_{xC} \tag{3.4}$$

Consequently, the summation of the low order harmonic components in the primary is zero and thus they will not show in the primary currents. However, this method is only valid if the number of cells/phase is multiple of three [15].

To eliminate the primary high order switching harmonics, the carriers are shifted between the parallel-connected cells by 120° [15].

g) Switches Ratings

The IGBT switches' voltage ratings are based on the DC-link voltage value (V_{dc}). To obtain the same drive output voltage waveform, the DC-link voltage is kept the same in both the conventional and the H-H cell. As a result, the switches' voltage ratings in both cells are equal to V_{dc}.

For the conventional 2L-VSI AFE, the maximum r.m.s. output line-to-line voltage is achieved using third order harmonic injection and is given by [2]:

$$V_{l-l,3\phi} = 0.707 V_{dc} \tag{3.5}$$

With the same DC-link voltage, the maximum r.m.s. phase ouput voltage from H-bridge is [2]:

$$V_{ph,1\phi} = 0.707 V_{dc} \tag{3.6}$$

The average powers in the conventional regenerative cell and the H-H cell are:

$$\begin{aligned} P_{in,3\phi} &= \sqrt{3} * V_{l-l,3\phi} * I_{ph,3\phi} \\ P_{in,1\phi} &= V_{ph,1\phi} * I_{ph,1\phi} \end{aligned} \tag{3.7}$$

By substitution with (3.5) in (3.6) in (3.7), for the same cell power rating in three-phase and single-phase AFEs, their input currents can be related by:

$$I_{1-\phi} = 1.73 I_{ph-3\phi} \tag{3.8}$$

Therefore, the current ratings of H-H cell AFE switches should be increased by 73% from the conventional cell AFE current ratings.

3.2.2 Semi-Reduced Power Cell

a) Power Cell Structure

A cell with further reduction from the H-H cell was proposed in [16], [17]. The cell configuration is shown in Fig. 3.7. Only six switches are used in the power cell by having a single phase half-bridge inverter as the AFE and the typical H-bridge in the output stage. Similar to the H-H cell, the single phase AFE is tied to the grid through a single phase transformer and a filter. The drive output modulation and control do not change.

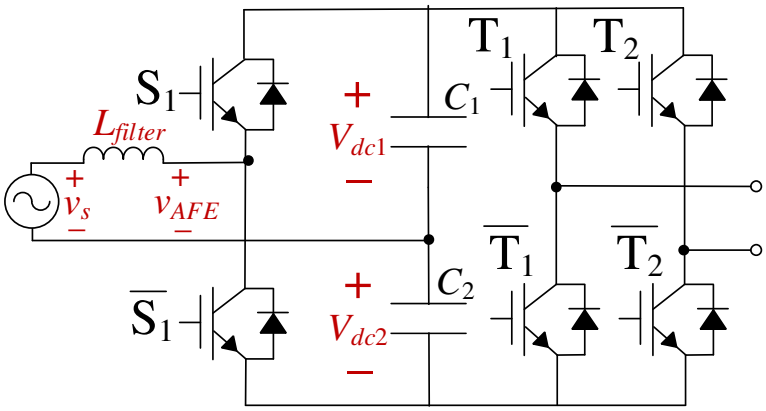

Fig. 3.7. Semi-Reduced Cell Power Cell Configuration [16], [17].

b) AFE Working Principle

- *AFE Modulation*

SPWM is used to modulate the half-bridge AFE [16], [17], [19]. The reference modulating signal is compared with one carrier signal to generate the gating pulses to the two complementary switches. The output voltage steps between $+V_{dc1}$ and $-V_{dc2}$, where V_{dc1} and V_{dc2} are the average DC voltages on C_1 and C_2 respectively. Ideally, V_{dc1} and V_{dc2} are equal to half of the total DC-link voltage (V_{dc}).

- *AFE Governing Equations*

Table 3.2 shows the possible two switching states. The equivalent circuit for each state is shown in Fig. 3.8 [16], [17], [19]. For proper control and operation, both V_{dc1} and V_{dc2} should be higher than the maximum of the input voltage v_s.

TABLE 3.2. HALF-BRIDGE AFE SWITCHING STATES AND THEIR CORRESPONDING OUTPUT VOLTAGE.

State Number	S_1	v_{AFE}
I	1	$+V_{dc1}$
II	0	$-V_{dc2}$

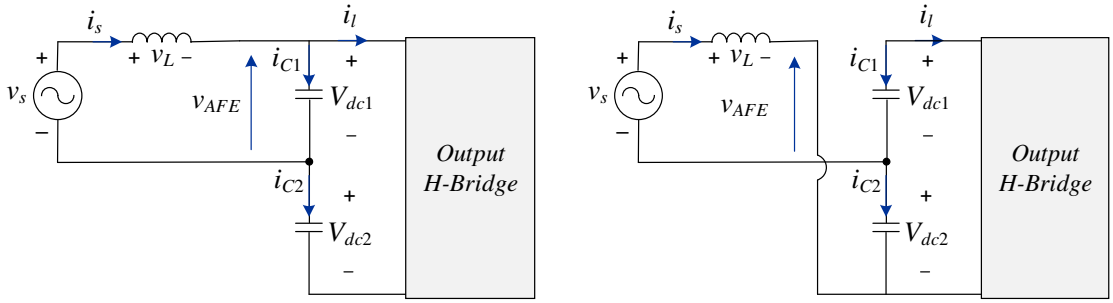

(a) AFE equivalent circuit in state I. (b) AFE equivalent circuit in state II.

Fig. 3.8. Semi-Reduced Cell AFE Equivalent Circuit in Different Switching States [16], [17], [19].

During state I, the inductor voltage can be expressed by:

$$v_L = L_{filter}\frac{di_s}{dt} = v_s - v_{AFE} = v_s - V_{dc1} \tag{3.9}$$

, where i_s is the cell input current, L_{filter} is the filter inductance.

The capacitors charging currents (i_{c1}, i_{c2}) and instantaneous voltages (v_{dc1} and v_{dc2}) are:

$$\begin{aligned} i_{c1} &= i_s - i_l \\ i_{c2} &= -i_l \end{aligned} \tag{3.10}$$

$$v_{dc1} = \frac{1}{C_1}\int i_{c1}dt$$
$$v_{dc2} = \frac{1}{C_2}\int i_{c2}dt \quad (3.11)$$

, where i_l is the input current to the load side H-bridge.

Based on (3.10) and (3.11),

1. Charging and discharging of C_1 depends on i_s - i_l, if i_s - $i_l > 0$, C_1 charges from the grid, if i_s - $i_l < 0$, C_1 discharges.
2. Charging and discharging of C_2 depends entirely on i_l.

In the complementary switching state II, (3.9) is modified to become:

$$v_L = L_{filter}\frac{di_s}{dt} = v_s - v_{AFE} = v_s + V_{dc2} \quad (3.12)$$

In this case, the capacitors charging currents become:

$$i_{c1} = -i_l$$
$$i_{c2} = -i_s - i_l \quad (3.13)$$

Therefore, during switching state II,

1. C_1 charging and discharging depend on i_l.
2. C_2 is charged when $i_s + i_l < 0$, and discharged when $i_s + i_l > 0$.

c) DC-Link ripples

In addition to the second order ripples from the output H-bridge inverter, the DC-link capacitors experience fundamental and second order ripples from the grid side [17]. This can be illustrated by using the average circuit model shown in Fig. 3.9(a).

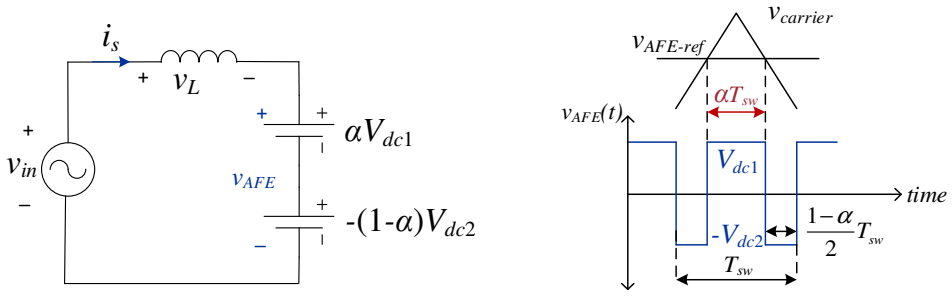

(a) Equivalent Circuit. (b) Modulator and Output Waveform.

Fig. 3.9. Half-Bridge AFE Average Model [17].

α is the duty ratio for the upper switch S_1 while (1-α) is the duty cycle ratio for the complementary switch. From Fig. 3.9(b), the duty ratio is given by [17]:

$$\alpha = \frac{1}{2} + \frac{v_{AFE-ref}}{V_{dc}} \tag{3.14}$$

, where $v_{AFE\text{-}ref}$ is the modulating signal and is expressed by:

$$v_{AFE-ref} = V_{AFE}\sin(\omega_{in}t - \delta) \tag{3.15}$$

, where δ is the AFE output fundamental phase shift from the grid voltage, and depends on the required power and input impedance.

To have unity power factor operation, the input current will be a sinusoidal wave of the same frequency and phase shift as the grid voltage. From Fig 3.9(a), (3.14), and (3.15), the instantaneous active power in each capacitor can be expressed by:

$$\begin{aligned} p_{c1}(t) &= \alpha V_{dc1} * i_s = \alpha V_{dc1} * I_s \sin(\omega_{in}t) \\ &= V_{dc1}\left(\frac{V_{AFE}I_s}{2V_{dc}}\left(\cos(\delta) - \cos(2\omega_{in}t - \delta)\right) + \frac{I_s}{2}\sin(\omega_{in}t)\right) \end{aligned} \tag{3.16}$$

$$\begin{aligned} p_{c2}(t) &= -(1-\alpha)V_{dc2} * i_s \\ &= V_{dc2}\left(\frac{V_{AFE}I_s}{2V_{dc}}\left(\cos(\delta) - \cos(2\omega_{in}t - \delta)\right) - \frac{I_s}{2}\sin(\omega_{in}t)\right) \end{aligned} \tag{3.17}$$

As the voltage harmonics are the same as the power harmonics in a capacitor, both C_1 and C_2 will experience input fundamental and second order voltage ripples. Their fundamental ripples are 180° out of phase. Therefore, the whole DC-link voltage is subjected to second-order harmonic ripples only [17].

d) Capacitors' Voltage Imbalance

As a result of control signals offsets, initial conditions, and manufacturing differences, voltage imbalance between both capacitors can take place. The controller must take care of these imbalances as will be explained in the controller section [16], [17], [19].

e) Cell Input Current Harmonics

Similar to the case of H-H cell, the second-order harmonic ripples are reflected from the capacitors' voltages to the cell input current as lower order harmonics. This is in addition to the higher order harmonic ripples from the SPWM switching [16], [17], [19].

f) AFE Control Scheme

The basic control scheme for the half-bridge AFE is shown in Fig. 3.10. It uses a DC-link voltage controller, a current controller, and a voltage balancing controller [16], [17], [19].

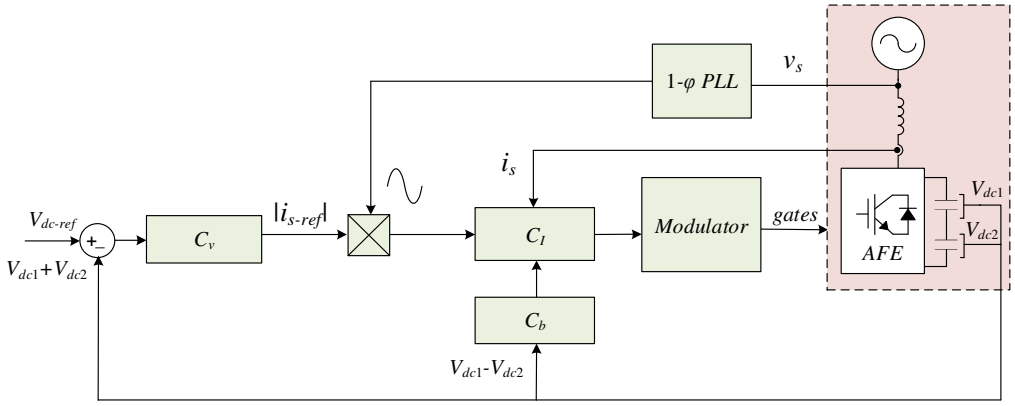

Fig. 3.10. Control Scheme Block Diagram for AFE in Semi-Reduced Cell [16], [17], [19].

The DC-link voltage controller (C_v) regulates the whole DC-link voltage. In [17], a PI controller is used for this purpose. A band-stop filter of cut-off frequency of $2\omega_{in}$ is required at the total DC-link voltage measurement so that it does not propagate through the controller. C_v sets the reference current magnitude ($\left|i_{s-ref}\right|$) required so that the DC-link voltage remains constant. The reference magnitude is then transformed to a vector of the same phase and frequency as the input voltage (v_s) for unity power factor operation.

The current controller (C_I) tracks the measured current to be equal to the reference current. In [16], C_I is chosen to be linear resonant controller at the grid frequency (ω_{in}), in order to have a perfect phase tracking on the current at this frequency.

Both C_v and C_I structures are expressed by [17]:

$$C_v = K_v \frac{s+\alpha_v}{s} \tag{3.18}$$

$$C_I = K_I \frac{s^2+\alpha_I s+\beta_I}{s^2-\omega_{in}^2} \tag{3.19}$$

, where K_v, α_v, K_I, α_I, and β_I are the controller constants. Their calculation depends on the required settling time, overshoot, and bandwidth.

To compensate the capacitors' voltage imbalance, a balancing controller (C_b) is used. A DC offset, depending on the difference between the two voltages ($\Delta V = V_{dc1} - V_{dc2}$), is introduced in the current reference signal ($\left|i_{s-ref}\right|$). This will shift the DC-link neutral point to balance the capacitors' voltages. The controller can be a simple proportional controller [16]. Nevertheless, the fundamental ripples in the two capacitors' voltages will be amplified and consequently propagate through the proportional controller. This will lead to unwanted

phase shift in the input current reference which reduces the input power factor. In order to solve this issue, a notch filter on the ΔV signal is proposed in [16] to attenuate the fundamental frequency components. Another drawback of the proportional controller is the steady state error, therefore a PI controller is recommended [17].

g) Compliance with Grid Connection Standards

In addition to the interconnection used in Fig. 3.6, another interconnection, shown in Fig. 3.11, is used in [17] to cancel lower order harmonics from the primary currents in the semi-reduced cell. The technique is similar to the parallel connection used in the H-H cell. The transformer, however, is a three phase transformer with separate single phase secondary windings.

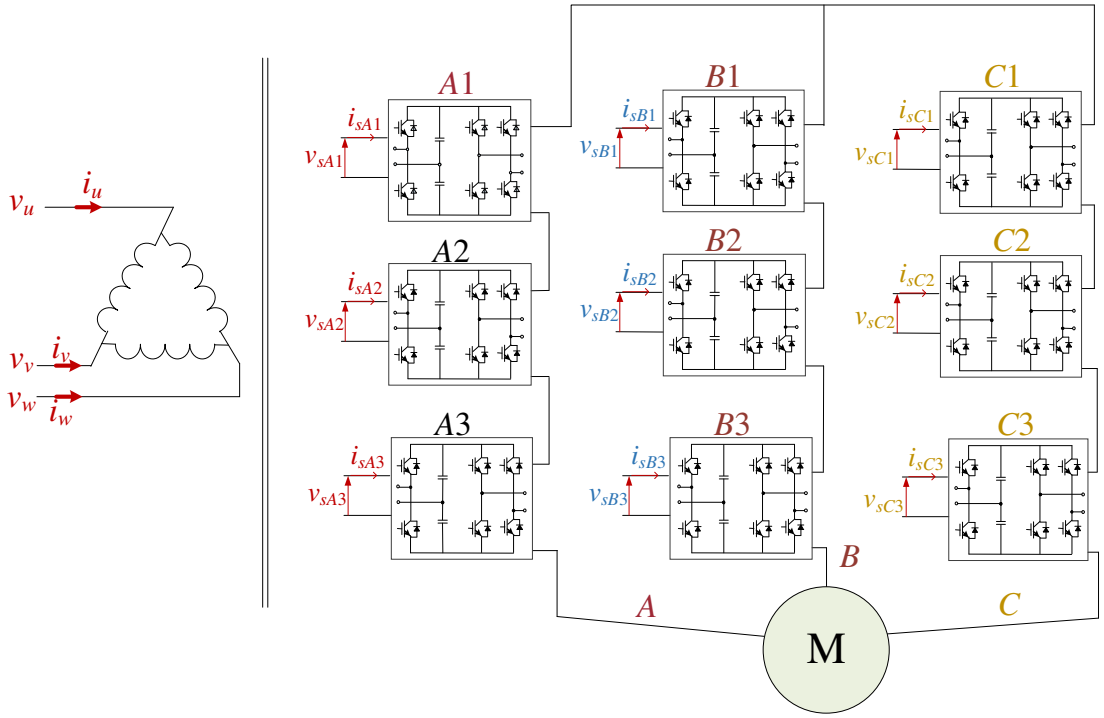

Fig. 3.11. Interconnection of 7-level CHB Semi-Reduced Cells [17].

The secondary voltages for each cell can be expressed as:

$$\begin{aligned} v_{sA1} &= v_{sB1} = v_{sC1} = V_s \sin(\omega_{in} t) \\ v_{sA2} &= v_{sB2} = v_{sC2} = V_s \sin(\omega_{in} t - \frac{2\pi}{3}) \\ v_{sA3} &= v_{sB3} = v_{sC3} = V_s \sin(\omega_{in} t + \frac{2\pi}{3}) \end{aligned} \tag{3.20}$$

The primary currents can be expressed by:

$$\begin{aligned} i_u &= \left[\left(i'_{sA1} + i'_{sB1} + i'_{sC1} \right) - \left(i'_{sA3} + i'_{sB3} + i'_{sC3} \right) \right] \\ i_v &= \left[\left(i'_{sA2} + i'_{sB2} + i'_{sC2} \right) - \left(i'_{sA1} + i'_{sB1} + i'_{sC1} \right) \right] \\ i_w &= \left[\left(i'_{sA3} + i'_{sB3} + i'_{sC3} \right) - \left(i'_{sA2} + i'_{sB2} + i'_{sC2} \right) \right] \end{aligned} \tag{3.21}$$

, where i'_{sx} is the reflected phase secondary current from cell *x*.

As the low frequency ripples in power and accordingly the voltage ripples on the capacitors in the drive output phase cells are phase shifted by 120°, by connecting the cells in the i^{th} row (A_i, B_i, and C_i), to the same primary winding through the secondary windings, the low order ripples will be cancelled at any frequency. However, input transformer saturation can take place at very low frequency operation. Moreover, the cancellation is only effective when the number of cells per phase is a multiple of three [16], [17].

h) Switches Ratings

The same analysis performed to the H-H cell can be applied to the semi-reduced cell by taking in consideration that the H-bridge output is double the half-bridge output [16], [17]. Therefore, having the same DC-link voltage as 2L-VSI, the cell r.m.s input voltage is given by:

$$V_{ph,half-bridge} = 0.35 V_{dc} \tag{3.22}$$

The input power is thus given by:

$$P_{half-bridge} = V_{ph,half-bridge} * I_{ph,half-bridge} \tag{3.23}$$

By equaling (3.23) with the three-phase power of 2L-VSI, the current is:

$$I_{ph,half-bridge} = 3.46 I_{ph,3\phi} \tag{3.24}$$

Therefore, the current rating of the switches in case of semi-reduced cell is increased by 246 % from the 2-L VSI AFE.

3.2.3 Reduced Power Cell

a) Power Cell Structure

A power cell with the least switch-count was proposed in [18]. This power cell, called reduced power cell, is shown in Fig. 3.12. It uses only four switches by employing a half-bridge configuration in both the AFE and the output of the cell with common connection to the DC-link midpoint.

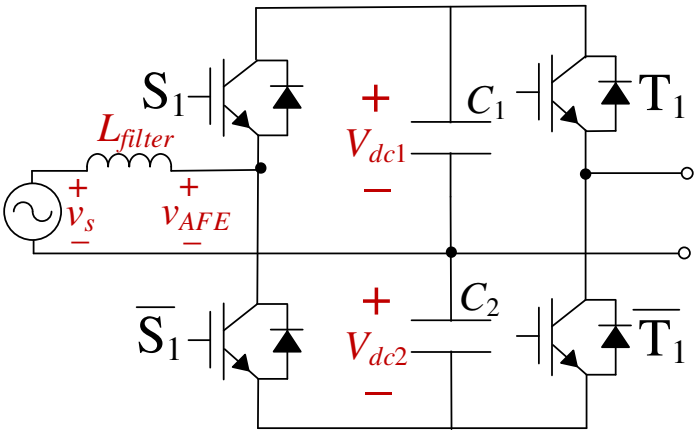

Fig. 3.12 Reduced Cell Power Cell Configuration [18].

b) Output Voltage Analysis

The half-bridge output inverter modulation and operation is the same as discussed in section 3.2.2-b), where the output voltage changes between two values ($+V_{dc1}$ and $-V_{dc2}$). Since the load side inverter is configured as half-bridge as well, the number of voltage levels obtained in the drive output phase is lower than in the case of using H-bridge output inverter. For n cells/phase, the number of drive output voltage levels obtained from the reduced cell is $n+1$ compared with $2n+1$ in case of using H-bridge output inverter. To improve the quality of the drive phase voltage, the carrier signals are shifted by $\frac{2\pi}{n}$ [18].

c) AFE Working Principle

The modulation and governing equations of the reduced cell AFE are the same as discussed in the semi-reduced cell [18].

d) DC-Link Ripples

The same analysis of the semi-reduced cell is applied for both the AFE and output inverters using the corresponding average models as in Fig. 3.9. The two average models can be analyzed separately with their corresponding duty ratios.

Using superposition, the instantaneous powers in both capacitors are given by:

$$\begin{aligned} p_{c1}(t) &= \alpha_{in} V_{dc1} * i_s + \alpha_o V_{dc1} * i_o \\ &= V_{dc1}\left[\begin{array}{l} \left(\frac{V_{AFE} I_s}{2V_{dc}}\left(\cos(\delta_{in}) - \cos(2\omega_{in}t - \delta_{in})\right) + \frac{I_s}{2}\sin(\omega_{in}t)\right) \\ +\left(\frac{V_o I_o}{2V_{dc}}\left(\cos(\phi_o) - \cos(2\omega_o t - \phi_o)\right) + \frac{I_o}{2}\sin(\omega_o t)\right) \end{array}\right] \end{aligned} \tag{3.25}$$

$$p_{C2}(t) = -(1-\alpha_{in})V_{dc2} * i_s - (1-\alpha_o)V_{dc2} * i_o$$
$$= V_{dc2}\left[\begin{array}{l}\left(\frac{V_{AFE}I_s}{2V_{dc}}\left(\cos(\delta_{in}) - \cos(2\omega_{in}t - \delta_{in})\right) - \frac{I_s}{2}\sin(\omega_{in}t)\right) \\ +\left(\frac{V_oI_o}{2V_{dc}}\left(\cos(\phi_o) - \cos(2\omega_o t - \phi_o)\right) - \frac{I_o}{2}\sin(\omega_o t)\right)\end{array}\right] \quad (3.26)$$

, where α_{in} and α_o are the AFE input and inverter output duty ratios respectively, V_o and I_o are the output voltage and current magnitudes, and ϕ_o is the phase shift between the output voltage and current.

From (3.25) and (3.26), it is shown that both capacitors will undergo fundamental and second order harmonic ripples from both the input and output sides of the cell. However, on the total DC-link, only input and output second order harmonics will show.

e) Capacitors' Voltage Imbalance

As in the case of semi-reduced cell, the controller must take care of the capacitors' imbalances resulting from operational and manufacturing differences.

f) Cell Input Current Harmonics

Similar to the case of previous reduced switch-count cells, the second-order harmonic ripples are reflected from the capacitors' voltages to the input current as lower order harmonics. This is in addition to the higher order harmonic ripples from the SPWM switching [18].

g) AFE Control Scheme

The same controller used in case of the semi-reduced cell (Fig. 3.10) can be applied. In [18], PI controller was used in both DC-link voltage and current controlling loops.

h) Compliance with Grid Connection Standards

The same interconnections shown in Fig. 3.6 and Fig. 3.11 can be used to cancel the lower order harmonics in the primary currents. The number of cells per phase must be a multiple of three for these interconnections to be effective [18].

i) Switches Ratings

Due to the presence of half-bridge inverter in the cell output, the DC-link voltage must be 100% more than the case when an H-bridge is used to generate the same output voltage values. That means the voltage ratings of all the switches used in the reduced cell must be doubled.

As the DC-link voltage is doubled, the AFE switches current ratings are now 73% more than the 2L-VSI AFE switches.

3.2.4 Challenges of the Existing Reduced Switch-Count Power Cells

Based on the review of the existing reduced switch-count power cells, the reduction of switches number in these cells is associated by many challenges [15]-[19]:

- Although the single phase interface allows the use of simpler transformer, the control of single phase AFE is more complex than three phase systems as it depends on time varying variables in the stationary *abc*-reference.

- The total DC-link experiences second order harmonics from the grid side as well as the load side. In case of semi-reduced and reduced cells, the individual capacitors experience fundamental voltage ripples from the grid side as well. These ripples on individual capacitors are accompanied by output fundamental ripples in the reduced cell.
- The second order harmonic ripples on the DC-link are reflected in the input currents as low order harmonics. The elimination of these harmonics from the primary is only valid if the number of cells per phase is a multiple of three.
- The capacitors in case of semi-reduced and reduced cells can be subjected to voltage imbalance due to manufacturing and operating differences.
- The number of possible output voltage levels from the reduced cell is n+1 for n cells/phase, compared with 2n+1 levels from other configurations, this lower number of levels results in higher distortion in the output voltage and current.
- The switches voltage ratings are doubled in case of the reduced cell. As for the current ratings, the input current is increased from the conventional cell by 73% in case of H-H cell and reduced cell, and 246% in case of semi-reduced cells.

Accordingly, it can be concluded that among single-phase AFEs, H-H cell is the best candidate. However, complex control in the stationary reference frame, low order harmonics in the input primary current with limitation on their cancellation or reduction, and DC-link ripples of 2nd order input frequency can hinder their practical implementation.

Three-phase AFEs provide simpler control in the rotating *d-q* reference frame. Moreover, they cancel the low order harmonics from the input primary currents without any limitation imposed by the cell numbers. As a result, the first contribution in this work is to reduce the power cell switch-count while having a three-phase interface which allows simpler control, finer harmonic performance, and a better tradeoff.

3.3 Possible Reduced Switch-Count Configurations based on Three-Phase AFE

As CHB power cells are based on low voltage ratings, this enables the adoption of low voltage drives configurations inside the power cell. The following two cell structures are briefly reviewed as possible solutions based on reduced switch-count low voltage drives configurations with three-phase input. The first configuration is chosen as the first proposed solution in this thesis for further analysis hereinafter.

3.3.1 Four-Switch Three-Phase Input–H-Bridge Output Configuration

Fig. 3.13 shows the first proposed cell configuration based on employing a four-switch three-phase inverter (FSTPI) as the active front end. Accordingly, it uses eight switches as the H-H cell instead of ten. FSTPI is a common low-cost solution for low voltage drives [27]-[31]. Detailed analysis of this cell is discussed in the following chapter.

The three-phase interface makes it easy to control in the rotating *d-q* frame. The modulation and control schemes were thoroughly discussed in literature [27]-[31]. It can be modulated using SVM [28]-[31] or SPWM [27], [28] with minor alteration to the modulation signals of the conventional cell AFE.

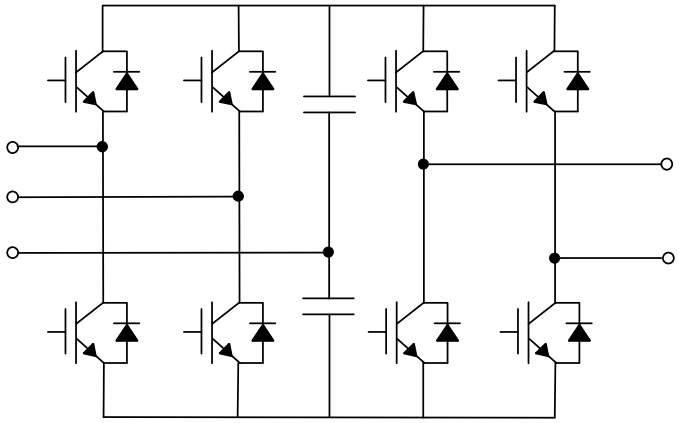

Fig. 3.13. Possible Reduced Switch Count Configuration I:
Four-Switch Three-Phase Input–H-Bridge Output.

In addition to the output 2nd order and switching harmonics ripples, the DC-link capacitors are subjected to fundamental ripples form the input side, due to the midpoint connection to one of the phases [27].

The two capacitors experience voltage imbalance in case of low frequency input or input subharmonics. This imbalance can be compensated by the controller by introducing an offset to the modulation reference [27]-[31].

The r.m.s. line-to-line voltage that can be reached by this configuration is 0.35 V_{dc} [27]-[31]. Accordingly, for the same DC-link voltage and power ratings as 2L-VSI AFE, the input current should be 100% more than the case of 2L-VSI AFE.

3.3.2 2L-VSI Input – H Bridge Output with Shared Leg Configuration

Fig. 3.14 shows another reduced switch-count configuration with a shared leg connection between a 2L-VSI in the input side and an H-bridge in the output side. This configuration is adopted from the low-cost low-voltage drive proposed in [32] which is based on single-phase grid to three-phase motor drive.

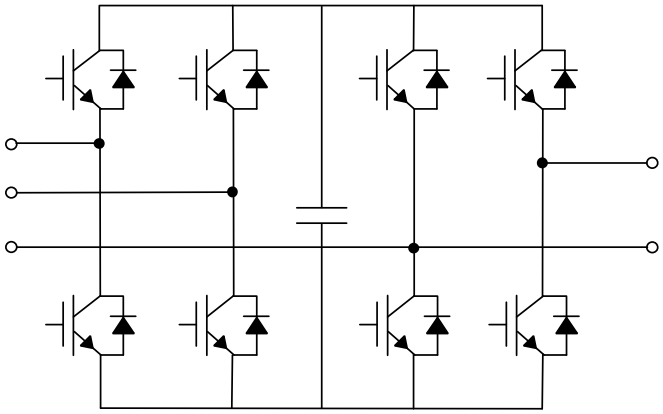

Fig. 3.14. Possible Reduced Switch-Count Configuration II:
2L-VSI Input – H Bridge Output with Shared Leg Configuration.

Due to the presence of a shared leg between the input and output sides, the modulation and control is more complex. In [32], four SVM methods are proposed, which compromise between the AFE and output DC-link utilization factors:

- Method I depends on setting the shared connection point voltage with respect to the three-phase side neutral point (v_{on}) to be equal to zero. Consequently, the AFE is controlled as an FSTPI with DC-link utilization of 35% and the output inverter is controlled as half-bridge inverter with DC-link utilization of 35%.
- Method II aims to have a general solution to increase the output phase voltage of the AFE side by calculating instantaneous values of v_{on} based on the maximum phase voltage in both sides.
- Method III associates v_{on} to a local apportioning factor to achieve the maximum output voltage.
- Method IV uses *d-q* reference frame in the three-phase side to control the voltage and set the switching times, the single phase side modulation is determined after.

The control of the power flow from the single phase side to three phase is presented in [32]. The modification of this controller for power flow from the three-phase to the single-phase side is required for application in a power cell and is a good topic for research.

Due to the absence of DC-link midpoint connection to the grid, the only ripples present are the switching high frequency harmonics and second-order harmonics from the output side.

As previously stated, a trade-off should be made between the input and output sides due to their coupling. According to [32], the minimum AFE DC-link utilization, 35%, corresponds to the maximum output inverter utilization of 35%. On the other hand, the maximum AFE output utilization of 53% corresponds to minimum output inverter utilization of 17.7%. Since higher output DC-link utilization is required in the drive, the first option might be the most suitable. Based on the highest DC-link utilization for the output inverter, the DC-link voltage is increased to $2V_{dc}$ to obtain the same output voltage as the conventional cell, and accordingly the switches' voltage ratings are doubled.

For the current ratings, the following should be considered [32]:

- The input current to keep the power rating the same is the same input current in case of 2L-VSI AFE as the DC-link voltage is doubled.
- The input unshared-leg switches current rating is the same as of input 2L-VSI AFE switches.
- The output unshared-leg switches current rating is the same as the conventional cell output H-bridge switches.

- The shared-leg switches current rating is based on the sum of both the input and output maximum currents.

The analysis of this cell in CHB drives is a very interesting topic for future research.

3.4 Summary

To have more economic regenerative CHB drives, three CHB power cells with reduced switch-count were proposed in the literature that are based on employing single-phase AFEs. Table. 3.3 shows their comparison with the conventional regenerative cell as a benchmark for the required performance. The detailed review of these configurations' pros and cons shows the need for reduced switch-count cell with three-phase AFE. To achieve this, two proposed power cell configurations that are adopted from low voltage drives are briefly reviewed.

The presented work focuses on the first proposed configuration, four-switch three-phase input – H-bridge output cell, since it has simpler control, easier implementation, and avoids the higher current ratings of the shared leg switches. In the following chapter, the proposed cell configuration is analyzed thoroughly. The results show promising performance of the suggested configuration to replace the conventional regenerative cell with lower number of switches.

TABLE 3.3. COMPARISON BETWEEN EXISTING REGENERATIVE CHB POWER CELL REDUCED SWITCH COUNT CONFIGURATIONS WITH CONVENTIONAL REGENERATIVE CELL.

Cell Configuration	Conventional [12], [14]	H-H [15]	Semi-Reduced [16], [17]	Reduced [18]
Number cell switches	10	8	6	4
Output voltage levels for *n* cells/phase	$2n+1$	$2n+1$		$n+1$
AFE interface	Three-phase	Single-phase		
AFE control reference frame	Rotating *d-q* frame	Stationary *abc* -frame More Complex		
Low order harmonic elimination from primay current	Effective for any number of cells/phase	Effective only if number of cells/phase is multiple of three		
Low Order DC-link ripples	Output 2nd order ripples	Output and input 2nd order ripples		
Capacitors ripples	Output 2nd order	Output and input 2nd order		
			Input Fundamental	
				Output fundamental
Capacitors' voltage imbalance	Do not exist	Do not exist	Exists	
AFE Switches current rating	I_{in}	$1.73\ I_{in}$	$3.46\ I_{in}$	$1.73\ I_{in}$
Switches voltage rating	V_{dc}	V_{dc}		$2\ V_{dc}$

Chapter 4

Proposed Reduced Switch-Count Regenerative CHB Power Cell Configuration with New Modulation Techniques

4.1 Introduction

The review and analysis of the existing reduced switch-count power cells, which are based on single-phase AFEs, have highlighted the necessity to have a reduced switch-count configuration based on three-phase AFEs. As discussed in the previous chapter, the fact that CHB power cells are based on low voltage enables the adoption of configurations from

low voltage drives. In this chapter, a new regenerative power cell configuration is proposed to reduce the number of switches by using a four-switch three-phase inverter as AFE. Four-switch three-phase inverter (FSTPI) is a common solution for low cost and low voltage drives [27]-[31]. Detailed study of the configuration is provided in this chapter. The standalone operation of FSTPI has three main challenges:

- Capacitors' voltage imbalance.
- Current triplen harmonics and unbalance.
- Need for very high switching frequency or a trap-filter to comply with the gird connection standards.

These challenges are addressed in this chapter with detailed analysis:

- The capacitors are proved to be inherently balanced in AFE operation.
- A phase alternation connection method is proposed to eliminate the current triplen harmonics and unbalance.
- Also, two carrier shifting techniques are introduced to allow operation at typical switching frequency (2 kHz) using only L-filter.

Simulation studies are conducted to verify the theoretical analysis. Results show the proposed configuration has promising performance to be implemented in a more economic version of regenerative CHB drives.

4.2 Proposed Power Cell Configuration

Fig. 4.1 shows the power cell configuration proposed to be used in regenerative CHB drives. The cell uses eight switches instead of the conventional cell ten switches. A four-

switch three-phase inverter (FSTPI) is used as the AFE. Two phases are connected to controlled legs, while the third is connected to the DC-link midpoint. The AFE is connected to one secondary winding of the phase-shifting or multi-winding transformer through an L-filter. The cell output is an H-bridge inverter as the conventional cell. Consequently, there is no change in the output side operation, control, or number of obtainable voltage levels from the conventional cell configuration. Since the DC-link capacitors are series connected from the output side perspective, each capacitor should be double the value of the required capacitance in the conventional power cell.

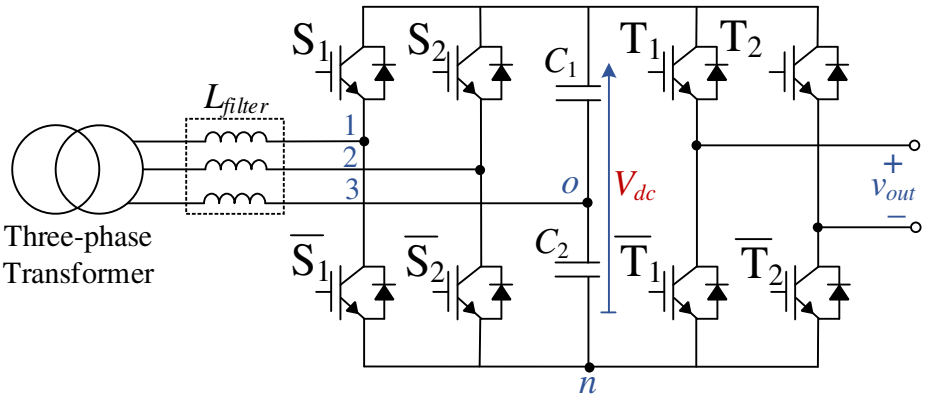

Fig. 4.1. Proposed Regenerative CHB Power Cell with FSTPI AFE.

4.3 FSTPI Standalone Operation

4.3.1 Switching States and Voltages Vectors

In the FSTPI shown in Fig. 4.2(a), as one phase is confined to the DC-link midpoint (*o*), the inverter has two degrees of freedom instead of three as in the 2L-VSI. As a result, only four switching states can exist as shown in Fig. 4.2(b) [27]-[31]. The output voltage vector for each switching state can be expressed by:

$$\bar{v} = \frac{2}{3}\left(S_1 * V_{dc} + S_2 * V_{dc} * e^{i\frac{2\pi}{3}} + \frac{V_{dc}}{2} * e^{-i\frac{2\pi}{3}} \right) \tag{4.1}$$

, where the reference is taken at point (n), the negative rail of the DC-link.

The DC-link average voltage (V_{dc}) is assumed to be equally distributed on the two capacitors (C_1 and C_2). The output voltages of the two controllable phases switch between zero and V_{dc}, while the confined phase is fixed at $\frac{V_{dc}}{2}$. Table 4.1 and Fig. 4.3 show resultant voltage vectors corresponding to each switching state.

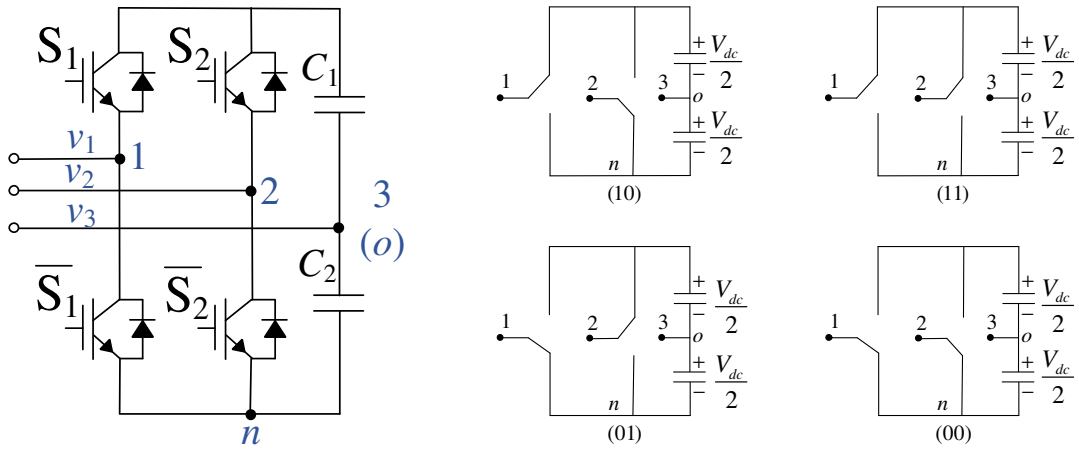

(a) Four-Switch Three-Phase Inverter (b) FSTPI Switching States.

Fig. 4.2. Four-Switch Three-Phase Inverter (FSTPI) Operation [27]-[31].

TABLE 4.1. RESULTING VOLTAGE VECTORS FROM FSTPI SWITCHING STATES [27]-[31].

Vector	Switching State		Voltage Vector	
	S_1	S_2	Magnitude	Angle
V_1	1	0	$V_{dc}/\sqrt{3}$	-30°
V_2	1	1	$V_{dc}/3$	60°
V_3	0	1	$V_{dc}/\sqrt{3}$	150°
V_4	0	0	$V_{dc}/3$	240°

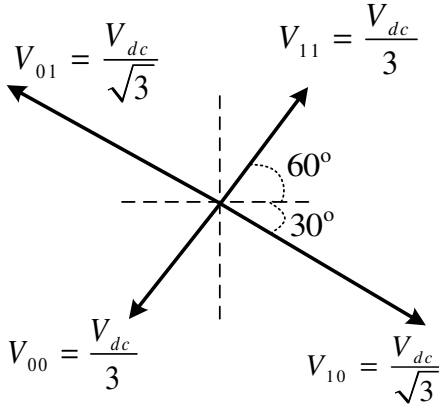

Fig. 4.3. FSTPI Voltage Vectors [27]-[31].

From the previous analysis, the following points are concluded [27]-[31]:

1. Every two complementary states produce two complementary voltage vectors that are equal in magnitude but phase-shifted with 180°.
2. Unlike the 2L-VSI, there is no direct zero voltage vector. Nevertheless, the zero voltage vector can be synthesized using application of two complementary voltage vectors for equal amount of time.
3. As there are now four switching states instead of eight, the switching frequency should be increased to reduce the harmonic distortion.
4. The maximum output line-to-line voltage is $V_{dc}/2$.

4.3.2 FSTPI Modulation

The SPWM and SVM modulation methods of FSTPI has been discussed extensively in literature [27]-[31].

a) SVM

Different implementations of SVM techniques are provided in literature depending on how zero voltage vector is synthesized [28]-[31]. Many combinations were proposed to divide the zero voltage vector switching time (T_o) between the resultant vectors. It can be split between two complementary vectors, or between all the four vectors. Each combination yields a certain harmonic content. However, in all approaches, the switching frequency should be increased.

b) SPWM

SPWM technique was discussed in [27]. The desired FSTPI output phase voltages are:

$$\begin{aligned} v_{1-ref} &= V\sin(\omega t) \\ v_{2-ref} &= V\sin(\omega t - \frac{2\pi}{3}) \\ v_{3-ref} &= V\sin(\omega t + \frac{2\pi}{3}) \end{aligned} \tag{4.2}$$

, where V is the required output phase voltage amplitude, and ω is the required FSTPI output frequency.

Since, as shown in Fig. 4.2(a), phase 3 is connected to the DC-link midpoint (o), the reference point can be shifted to point o instead of n. The modulation now can be achieved with respect to this new reference. The modified required set of voltages becomes:

$$\begin{aligned} v_{1o-ref} &= v_{13} = v_{1-ref} - v_{3-ref} = \sqrt{3}V\sin(\omega t - \frac{\pi}{6}) \\ v_{2o-ref} &= v_{23} = v_{2-ref} - v_{3-ref} = \sqrt{3}V\sin(\omega t - \frac{\pi}{2}) \end{aligned} \tag{4.3}$$

Since the system is balanced for fundamental components, the third line-to-line voltage fundamental component (v_{12}) can be calculated from these two voltages by:

$$v_{12-ref} = v_{13-ref} - v_{23-ref} = \sqrt{3}V \sin(\omega t + \frac{\pi}{6}) \tag{4.4}$$

The FSTPI modulator in [27] is shown in Fig. 4.4. The modulation scheme can be easily implemented by modifying the existing typical required phase modulation to line-to-line modulation using (4.3). It should be noted that carrier signals magnitude should be multiplied by $\sqrt{3}$.

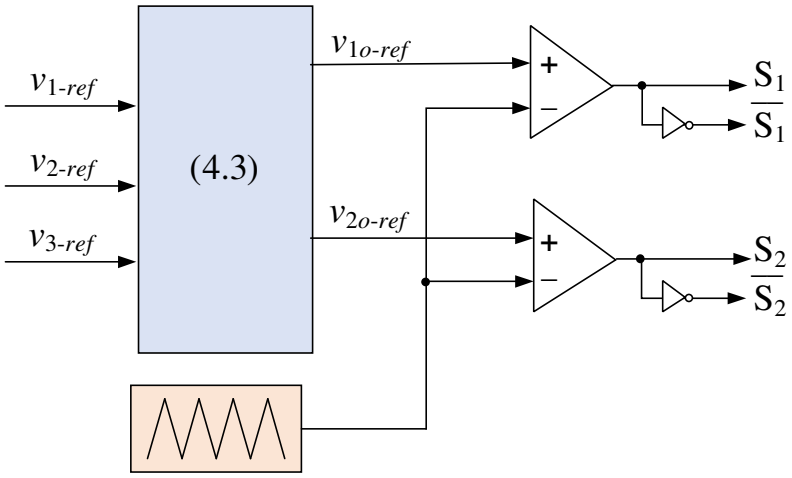

Fig. 4.4. SPWM Scheme Implementation for FSTPI [27].

The following points can be concluded for the SPWM technique:

1. The line-to-line voltage will switch between two levels: $\pm\frac{V_{dc}}{2}$. This results in higher harmonic distortion than the 2L-VSI. Therefore, higher switching frequency is required.
2. Since line-to-line voltage is directly modulated, triplen harmonics will not be cancelled if third order harmonic injection SPWM is used.

In this work, SPWM scheme is used for modulation due to its simplicity and ease of implementation.

4.3.3 Capacitors' Voltages Imbalance

Average voltages on both capacitors can become imbalanced due to control signals offsets, initial conditions, and manufacturing differences. In [27], this imbalance is compensated by inserting a DC-offset to the modulating signals. The offset depends on the average voltage difference between the two capacitors.

However, the grid connection in the CHB structure will lead to inherent balancing of these capacitors as will be explained later.

4.4 Single Power Cell Performance

4.4.1 Capacitors Ripples

To understand the capacitors' voltage ripples, analysis of capacitor currents in a power cell is provided. For the FSTPI connected to an H-bridge in the power cell shown in Fig. 4.5, capacitors currents can be divided into two components: input side components ($i_{dc\text{-}in1}$, and $i_{dc\text{-}in2}$) and output side component ($i_{dc\text{-}o}$).

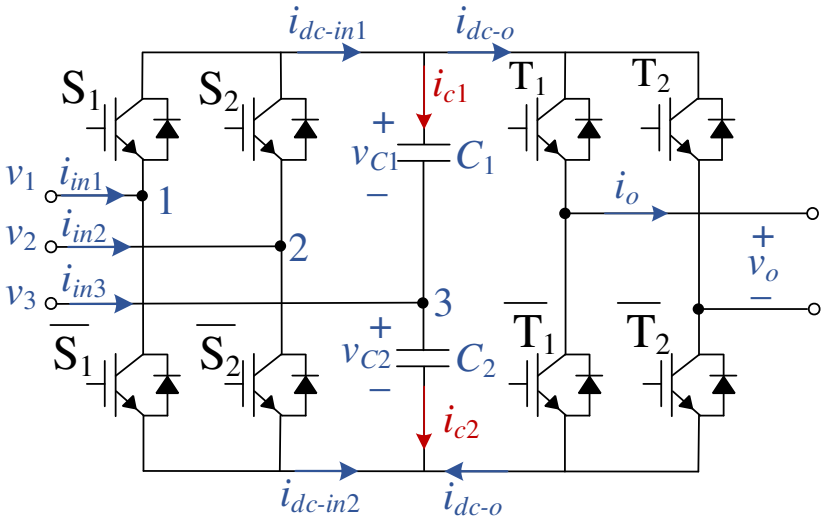

Fig. 4.5. FSTPI in a CHB Power Cell.

From the input side, the line voltages of the FSTPI in (4.3) can be expressed in terms of the switching states by [27]:

$$\begin{bmatrix} v_{1n} \\ v_{2n} \end{bmatrix} = \begin{bmatrix} S_1 & \overline{S_1} \\ S_2 & \overline{S_2} \end{bmatrix} \begin{bmatrix} V_{c1} \\ -V_{c2} \end{bmatrix} = \begin{bmatrix} S_1 & \overline{S_1} \\ S_2 & \overline{S_2} \end{bmatrix} \begin{bmatrix} \frac{V_{dc}}{2} \\ -\frac{V_{dc}}{2} \end{bmatrix} \tag{4.5}$$

, where V_{c1} and V_{c2} are average capacitors voltages and are assumed to be equal to half of the DC-link voltage.

The switching states must verify the following conditions [27]:

$$\begin{aligned} S_1 + \overline{S_1} &= 1 \\ S_2 + \overline{S_2} &= 1 \\ 0 \le S_x &\le 1, x = 1,2 \end{aligned} \tag{4.6}$$

From (4.3), (4.5), and (4.6), the fundamental switching states can be expressed as [27]:

$$\begin{aligned} S_1 &= 0.5\left[1 + m_{in}\sin\left(\omega_{in}t - \frac{\pi}{6}\right)\right] \\ \overline{S_1} &= 0.5\left[1 - m_{in}\sin\left(\omega_{in}t - \frac{\pi}{6}\right)\right] \\ S_2 &= 0.5\left[1 + m_{in}\sin\left(\omega_{in}t - \frac{\pi}{2}\right)\right] \\ \overline{S_2} &= 0.5\left[1 - m_{in}\sin\left(\omega_{in}t - \frac{\pi}{2}\right)\right] \end{aligned} \tag{4.7}$$

, where ω_{in} is the input angular frequency, and m_{in} is the modulation index given by:

$$\begin{aligned} m_{in} &= 2\sqrt{3}\frac{V_{dc}}{2} \\ |m_{in}| &\le 0 \end{aligned} \tag{4.8}$$

The input fundamental currents are expressed in time domain as [27]:

$$\begin{aligned} i_1 &= I_{in}\sin(\omega_{in}t-\theta) \\ i_2 &= I_{in}\sin(\omega_{in}t-\frac{2\pi}{3}-\theta) \\ i_3 &= I_{in}\sin(\omega_{in}t+\frac{2\pi}{3}-\theta) \end{aligned} \tag{4.9}$$

, where I_{in} is the input current fundamental magnitude, and θ is the phase shift between the FSTPI output fundamental phase voltage and current.

By using Kirchhoff's current law, the DC-link input currents ($i_{dc\text{-}in1}$ and $i_{dc\text{-}in2}$) are given in terms of the switching states by:

$$\begin{bmatrix} i_{dc-in1} \\ i_{dc-in2} \end{bmatrix} = \begin{bmatrix} S_1 & S_2 \\ \overline{S_1} & \overline{S_2} \end{bmatrix} \begin{bmatrix} i_1 \\ i_2 \end{bmatrix} \tag{4.10}$$

By substitution with (4.7) in (4.10), the DC-link input currents are:

$$\begin{aligned} i_{dc-in1} &= \frac{I_{in}}{2}\sin\left(\omega_{in}t-\theta-\frac{\pi}{3}\right)+\frac{\sqrt{3}}{4}m_{in}*I_{in}*\cos\theta \\ i_{dc-in2} &= \frac{I_{in}}{2}\sin\left(\omega_{in}t-\theta-\frac{\pi}{3}\right)-\frac{\sqrt{3}}{4}m_{in}*I_{in}*\cos\theta \end{aligned} \tag{4.11}$$

By applying the same approach in the output side, the output fundamental switching states are given by:

$$\begin{aligned} T_1 &= 0.5\left[1+m_o\sin\left(\omega_o t\right)\right] \\ \overline{T_1} &= 0.5\left[1-m_o\sin\left(\omega_o t\right)\right] \\ T_2 &= 0.5\left[1+m_o\sin\left(\omega_o t-\pi\right)\right] \\ \overline{T_2} &= 0.5\left[1-m_o\sin\left(\omega_o t-\pi\right)\right] \end{aligned} \tag{4.12}$$

, where m_o is the output modulation index, ω_o is the output frequency.

The output fundamental current is given by:

$$i_o = I_o \sin(\omega_o t - \phi_o) \tag{4.13}$$

, where I_o is the fundamental output current magnitude, ϕ_o is the phase-shift between the fundamental output phase voltage and current.

From (4.12) and (4.13), the DC-link output current ($i_{dc\text{-}o}$) to the H-bridge inverter is given by:

$$\begin{aligned} i_{dc-o} &= [T_1 - T_2] * i_o \\ &= [2m_o \sin(\omega_o t)] * I_o \sin(\omega_o t - \phi_o) \\ &= m_o * I_o [\cos\phi_o + \cos(2\omega_o t - \phi_o)] \end{aligned} \tag{4.14}$$

By applying Kirchhoff's current law at the DC-link positive and negative rails, the capacitors currents i_{c1} and i_{c2} are given by:

$$\begin{aligned} i_{c1} &= i_{dc-in1} - i_{dc-o} \\ &= \frac{\sqrt{3}}{4} m * I_{in} * \cos\theta + \frac{I_{in}}{2} \sin\left(\omega_{in} t - \theta - \frac{\pi}{3}\right) \\ &\quad - m_o * I_o [\cos\phi_o + \cos(2\omega_o t - \phi_o)] \\ i_{c2} &= -i_{dc-in2} - i_{dc-o} \\ &= \frac{\sqrt{3}}{4} m * I_{in} * \cos\theta - \frac{I_{in}}{2} \sin\left(\omega_{in} t - \theta - \frac{\pi}{3}\right) \\ &\quad - m_o * I_o [\cos\phi_o + \cos(2\omega_o t - \phi_o)] \end{aligned} \tag{4.15}$$

The voltages across the capacitors are given as:

$$\begin{aligned} v_{c1} &= \frac{1}{C_1} \int i_{c1} dt \\ v_{c2} &= \frac{1}{C_2} \int i_{c2} dt \end{aligned} \tag{4.16}$$

From (4.15) and (4.16), it is clear that in addition to switching harmonics from the input and output sides, the capacitors experience the following voltage ripples:

1. Voltages ripples of input fundamental frequency (ω_{in}), due to the connection of the DC-link midpoint to one of the input phases. The ripples across the two capacitors are out of phase by 180°. As a result, these ripples can cancel each other when added and do not show on the whole DC-link voltage.
2. Voltage ripples of output second-order harmonic frequency ($2\omega_o$), due to the single-phase pulsating power required by the H-bridge inverter. Since these components are in phase, they appear on the total DC-link voltage.

4.4.2 Cell Input Current Harmonics

The FSTPI input line currents contain lower order harmonics due to capacitors ripples. The DC-link ripples of $2\omega_o$ frequency injects ripples of $(\omega_{in} \pm 2\omega_o)$ frequencies into the input current. The ripples magnitude is inversely proportional to the output frequency and capacitors values. Nevertheless, these ripples will not show on the primary side because of the three-phase interface as will be explained hereinafter.

4.4.3 Cell Input Current Unbalance

The instantaneous difference between the two capacitors' voltages, due to the complementary ripples of the input fundamental frequency, leads to line current unbalance [27]. This unbalance is inversely proportional to the input frequency. Due to the grid connection in CHB power cell, the unbalance will be low. However, to comply with grid

connection standards (IEEE std. 519-2014) [33], a phase alternation method is proposed in the next section to eliminate this unbalance from the primary currents.

4.5 Challenges in Single-Cell Operation

From the previous analysis, the standalone and single-cell operation of FSTPI challenges can be summarized in the following:

1. Probability of capacitors' voltages imbalance.
2. Low order harmonics in the line currents.
3. No tolerance for third-order harmonic injection.
4. Line current unbalance.
5. The need for high switching frequency to have acceptable current distortion.

4.6 Integration into CHB Structure

The previous challenges of FSTPI standalone operation can be solved through integration in the modular CHB structure as will be shown hereinafter.

4.6.1 Capacitors' Voltages Inherent Balance

In AFE operation, the FSTPI is connected to a fixed-voltage three-phase source; i.e. the grid. This connection causes inherent balancing capability for the DC-link capacitors' average voltages in case of any dynamic disturbance or deviation in the control signals, initial states, or manufacturing differences.

In the grid-connected FSTPI shown in Fig. 4.6, as the same output inverter current ($i_{dc\text{-}o}$) is drawn from both capacitors, it does not affect their imbalance. Therefore, the analysis will focus on AFE side operation.

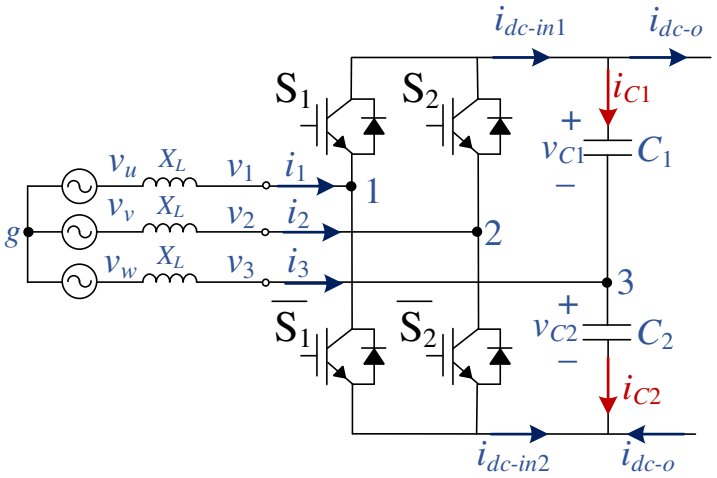

Fig. 4.6. Grid-Connected FSTPI.

The line currents i_1 and i_2 can be expressed by:

$$i_1 = \frac{v_{ug} - v_{1g}}{X_L}$$
$$i_2 = \frac{v_{vg} - v_{2g}}{X_L} \tag{4.17}$$

, where v_{ug}, v_{vg} are the grid phase voltages, X_L is the filter inductor, v_{1g} and v_{2g} are the inverter phase voltages.

The line-to-line FSTPI voltages are given by:

$$v_{13} = S_1 * V_{C1} - \overline{S_1} * V_{C2}$$
$$v_{23} = S_2 * V_{C1} - \overline{S_2} * V_{C2} \tag{4.18}$$
$$v_{12} = v_{13} - v_{23}$$

, where V_{C1} and V_{C2} are the average DC voltages across C_1 and C_2 respectively.

Accordingly, the converter output phase voltage can be expressed by:

$$v_{1g} = \frac{v_{12} + v_{13}}{3} = \frac{1}{3}\left[\left(2S_1 - S_2\right) * V_{C1} + \left(\overline{S_2} - 2\overline{S_1}\right) * V_{C2}\right]$$
$$v_{2g} = \frac{v_{23} + v_{12}}{3} = \frac{1}{3}\left[\left(2S_2 - S_1\right) * V_{C1} + \left(\overline{S_1} - 2\overline{S_2}\right) * V_{C2}\right] \tag{4.19}$$

V_{C1} and V_{C2} are given by:

$$\begin{aligned} V_{C1} &= V_{Co} + \Delta V_{C1} \\ V_{C2} &= V_{Co} + \Delta V_{C2} \end{aligned} \tag{4.20}$$

, where V_{Co} is the half of the reference DC-voltage ($V_{Co} = {V_{dc}}/{2}$), ΔV_{C1} and ΔV_{C2} are the deviation of the capacitors' average voltages from V_{Co}.

Since the whole DC-link average voltage is kept constant, the deviation in both voltages can be related to each other by the following relation:

$$\Delta V_{C1} = -\Delta V_{C2} \tag{4.21}$$

By substitution with (4.19) and (4.20) in (4.17), the controlled phase currents are:

$$\begin{aligned} i_1 &= I\sin(\omega_{in}t + \phi) - K_I * \Delta V_{C1} \\ i_2 &= I\sin(\omega_{in}t + \phi - 120^o) - K_I * \Delta V_{C2} \end{aligned} \tag{4.22}$$

, where I is the maximum phase current output, ϕ is arbitrary current phase angle, K_I is a constant that depends on the line filter inductor internal resistance.

Using Kirchhoff's current law, the capacitors currents are given by:

$$\begin{aligned} i_{C1} &= i_{dc-in1} - i_{dc-o} \\ &= \left(S_1 * i_1 + S_2 * i_2\right) - i_{dc-o} \\ &= \left(-K_I \Delta V_{C1} + \frac{\sqrt{3}}{4} m * I * \cos\theta - I_C \sin\left(\omega_{in}t - \theta - \frac{\pi}{3}\right)\right) - i_{dc-o} \\ i_{C2} &= i_{dc-in2} - i_{dc-o} \\ &= \left(-\overline{S_1} * i_1 - \overline{S_2} * i_2\right) - i_{dc-o} \\ &= \left(-K_I \Delta V_{C2} + \frac{\sqrt{3}}{4} m * I * \cos\theta + I_C \sin\left(\omega_{in}t - \theta - \frac{\pi}{3}\right)\right) - i_{dc-o} \end{aligned} \tag{4.23}$$

, where I_C is the magnitude of capacitor current ripples at input fundamental frequency.

In (4.23), each capacitor charging current contains an extra DC component that is directly proportional to the negative of the capacitor voltage deviation. Consequently, this will result in opposition of any tendency to deviate from the reference value of V_{Co}.

4.6.2 Inherent Low Order Harmonic Cancellation from the Primary Currents

Unlike single-phase AFEs, the three-phase interface of FSTPI allows the cancellation of low order harmonics of $(\omega_{in} \pm 2\omega_o)$ for any number of cells/phases. This can be illustrated for the regenerative CHB drive with *n* cells/phase with FSTPI AFE shown in Fig. 4.7. For the sake of simplification, the transformer configuration is assumed to be *Y/Y* with unity turns ratio, the primary currents can be expressed by:

$$I_{p-k} = \sum_{j=1}^{n} I_{sk-Aj} + I_{sk-Bj} + I_{sk-Cj} \tag{4.24}$$

, where *k* is the grid phase index (*u, v,* and *w*), *j* is the row number index, *p* stands for primary, and *s* stands for secondary.

As previously discussed, the resulting low order harmonic ripples in the secondary input currents for each drive phase cells will be phase-shifted by 120°. As a result, in (4.24), their summation in the primary windings will be equal to zero for any number of cells.

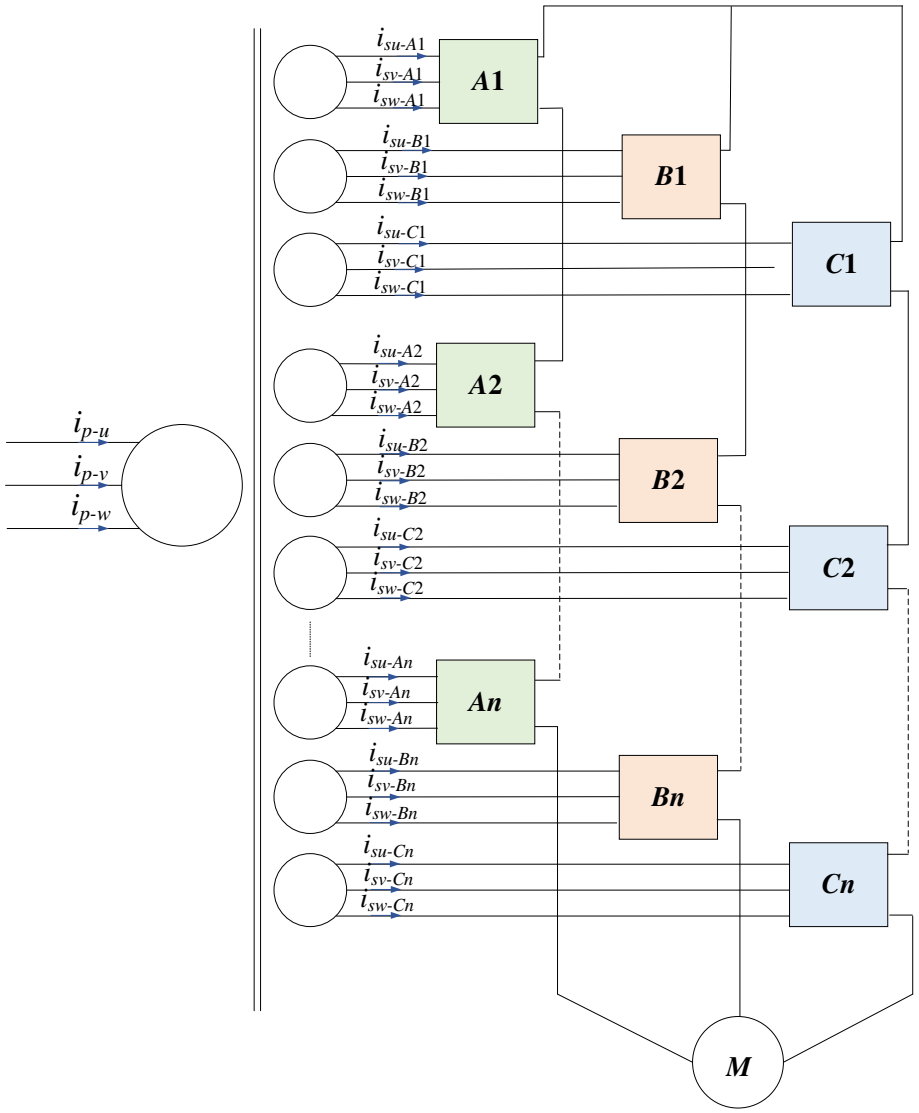

Fig. 4.7. Low Order Harmonics Cancellation in Proposed FSTPI-AFE Based CHB.

4.6.3 Proposed Phase Alternation Connection for Unbalance, Triplen Harmonics, and Carrier Harmonics Elimination

As discussed in the previous sections, the capacitors' fundamental ripples will cause the input current to be unbalanced. The input current will also include triplen harmonics due to these capacitors' ripples or if third order harmonic injection is used. This is in addition to

the carrier harmonics caused by high switching frequency. In this section, the unbalance and harmonic components are analyzed, and a phase alternation connection is proposed to eliminate these harmonics from the primary currents.

a) Analysis of Unbalance and Harmonic Components

- ***Unbalance Analysis:*** The cause of current unbalance is the fundamental ripples on the two capacitors. From (4.15) and (4.16), the phase shift of these fundamental ripples is a function of the phase shift of the first leg input current.
- ***Triplen Harmonics Analysis*****:** In the FSTPI shown in Fig. 4.6, as legs 1 and 2 are modulated according to two line-to-line voltages with respect to the same reference point, the phase shift between the leg modulations is always 60°. The triplen harmonic components in the line-to-line voltages for the FSTPI are expressed by:

$$\begin{aligned} v_{13-triplen} &= \sum_{k=3,9,15..} V_k \sin\left(k\left(\omega t+\varphi_{13}\right)\right) \\ v_{23-triplen} &= \sum_{k=3,9,15..} V_k \sin\left(k\left(\omega t+\varphi_{13}\right)-\pi\right) \\ &\text{Consequently,} \\ v_{12-triplen} &= \sum_{k=3,9,15..} 2V_k \sin\left(k\left(\omega t+\varphi_{13}\right)\right) \end{aligned} \tag{4.25}$$

, where k is the triplen harmonic order, V_k is the maximum triplen order line-to-line voltage, and φ_{13} is the fundamental phase-shift for the first line-to-line.

The triplen order harmonic phase voltages are then calculated to be:

$$\begin{aligned} v_{1g-triplen} &= \sum_{k=3,9,15..} V_k \sin\left(k\left(\omega t+\varphi_{13}\right)\right) \\ v_{2g-triplen} &= v_{1g-triplen} = \sum_{k=3,9,15..} V_k \sin\left(k\left(\omega t+\varphi_{13}\right)-\pi\right) \\ v_{3g-triplen} &= 0 \end{aligned} \tag{4.26}$$

Two points can be concluded from (4.26):

- For two controlled legs, that are fundamentally modulated with phase shift of 60° between them, their triplen order harmonic phase voltages and currents will be equal in magnitude but opposite in direction.
- The triplen order harmonics in the phase connected to DC-link midpoint are always zero.

– ***Carrier Harmonics Analysis*:** Carrier harmonics from switching an inverter leg with SPWM are expressed by [34]:

$$v_{carrier} = \sum_{m_c=1}^{\infty} V_{m_c} * \sin\left(m_c \frac{\pi}{2}\right) * \sin\left[m\left(\omega_c t + \theta_c\right)\right] \tag{4.27}$$

, where ω_c and θ_c are the carrier angular frequency and phase shift respectively, and m_c is the carrier index.

For the FSTPI operation, the switching harmonics for the line-to-line and phase voltages are:

$$\begin{aligned} v_{13-carrier} &= \sum_{m_c=1}^{\infty} V_{m_c} * \sin\left(m_c \frac{\pi}{2}\right) * \sin\left[m\left(\omega_c t + \theta_c\right)\right] \\ v_{23-carrier} &= \sum_{m_c=1}^{\infty} V_{m_c} * \sin\left(m_c \frac{\pi}{2}\right) * \sin\left[m\left(\omega_c t + \theta_c\right)\right] \\ v_{12-carrier} &= 0 \end{aligned} \tag{4.28}$$

$$\begin{aligned} v_{1g-carrier} &= \sum_{m_c=1}^{\infty} \frac{V_{m_c}}{3} * \sin\left(m_c \frac{\pi}{2}\right) * \sin\left[m_c\left(\omega_c t + \theta_c\right)\right] \\ v_{2g-carrier} &= \sum_{m_c=1}^{\infty} \frac{V_{m_c}}{3} * \sin\left(m_c \frac{\pi}{2}\right) * \sin\left[m_c\left(\omega_c t + \theta_c\right)\right] \\ v_{3g-carrier} &= \sum_{m_c=1}^{\infty} \frac{-2V_{m_c}}{3} * \sin\left(m_c \frac{\pi}{2}\right) * \sin\left[m_c\left(\omega_c t + \theta_c\right)\right] \end{aligned} \tag{4.29}$$

The carrier harmonics voltages in the two controlled phases are equal in magnitude and phase-shift, while the phase connected to the DC-link midpoint contains carrier harmonics of double the magnitude and opposite direction of the voltage in the controlled legs.

– ***Reflection of Unbalance and Harmonic Components in the Primary Currents:***

The phase sequence of the source connection to FSTPI input affects the magnitude and the phase shift in the unbalance, the triplen and carrier harmonics phase voltage components and consequently the currents. If the FSTPI legs are connected to the same phase sequence in all CHB cells as the example shown in Fig 4.8, the triplen harmonics, carrier harmonics, and the current unbalance will be reflected into the primary side.

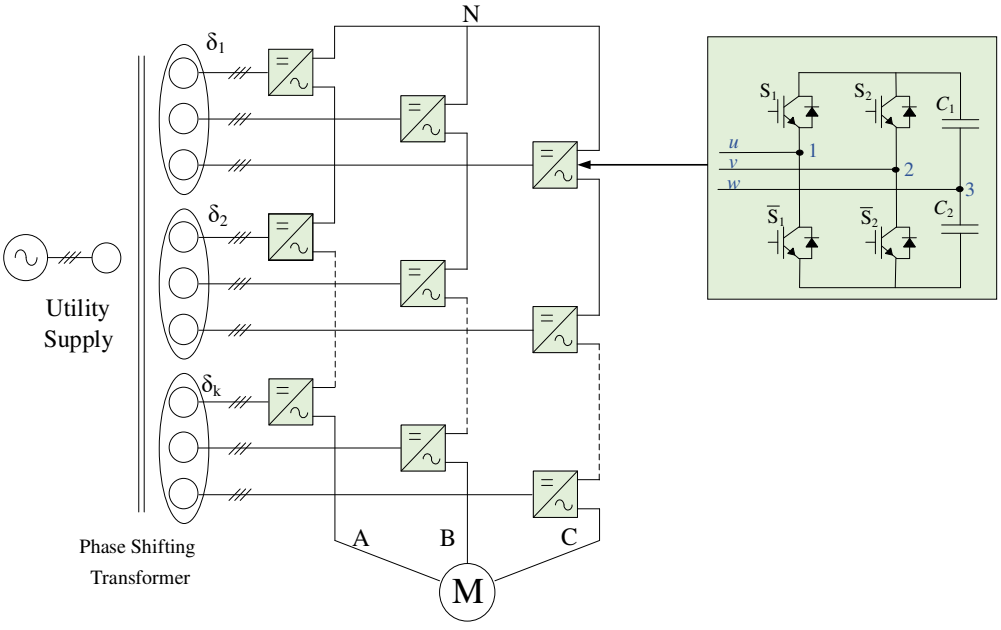

Fig. 4.8. Proposed CHB drive with All FSTPI-AFE Connected to the Same Phase Sequence.

b) Proposed Phase Alternation Connection for Unbalance, Triplen Harmonics, and Carrier Harmonics Cancellation

From the previous harmonic analysis, the cell input current unbalance, triplen, and carrier harmonics phase shift and magnitude depend on the phase sequence being controlled. This fact can be used to cancel the unbalance, triplen and carrier harmonics from the primary currents.

In this work, phase alternation connection between different cells is proposed as a solution. An example for the proposed phase alternation connection is shown in Fig. 4.9, where for the same secondary winding set supplying three row cells, the phase connected to the DC-link midpoint is alternated between the three cells

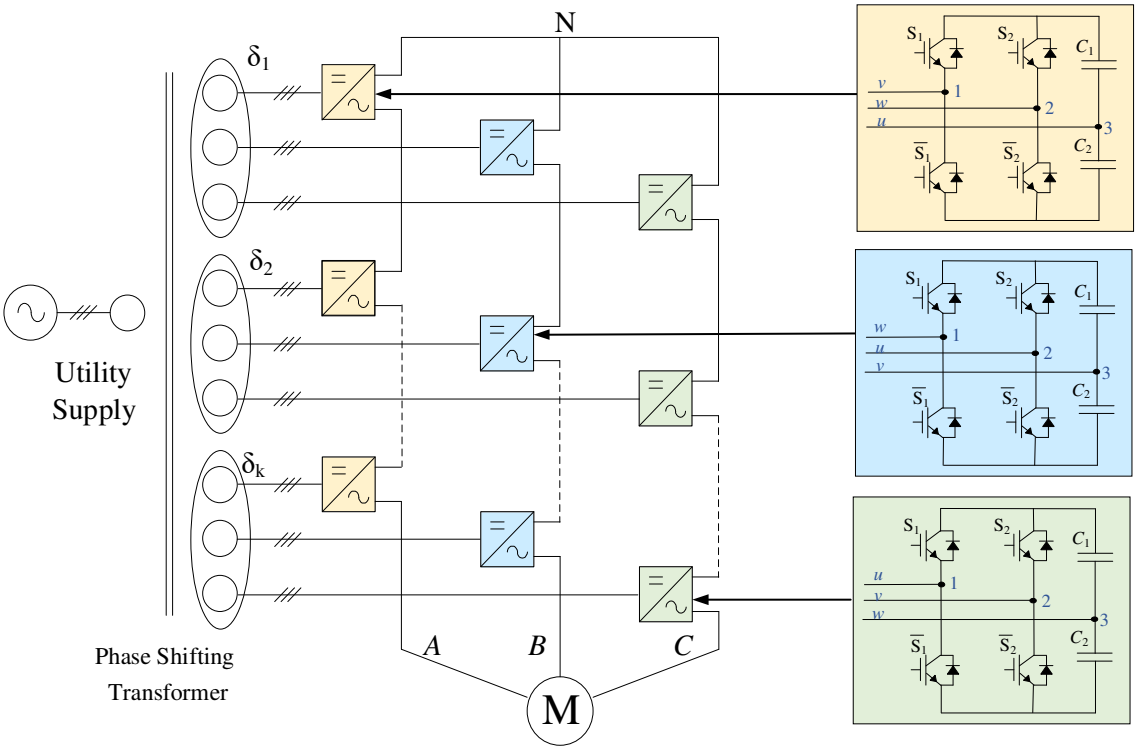

Fig. 4.9. Proposed Phase Alternation Example for Unbalance, Triplen and Carrier Harmonics Elimination.

In Fig. (4.9), the following connection is employed, however any equivalent connection is valid:

- For phase *A* drive cells, the DC-link midpoint connection (point 3) is connected to input phase *u*. The first and second leg midpoints (point 1 and 2) are chosen to be connected to phases *v* and *w* respectively. Thus, the two legs will be modulated to follow V_{vu} and V_{wu} respectively. As a result, the input currents triplen and carrier components for cell *x* in phase *A* are given by:

$$\begin{aligned} i_{3rd,u-Ax} &= 0 \\ i_{3rd,v-Ax} &= I_{3rd}\sin\left(3\omega t - \phi_{I-3rd} - \frac{\pi}{2}\right) \\ i_{3rd,w-Ax} &= I_{3rd}\sin\left(3\omega t - \phi_{I-3rd} + \frac{\pi}{2}\right) \end{aligned} \tag{4.30}$$

$$\begin{aligned} i_{m_c,u-Ax} &= \sum_{m_c=1}^{\infty}\frac{-2I_{m_c}}{3}\sin\left(m_c(\omega_c t - \theta_{cI})\right) \\ i_{m_c,v-Ax} &= \sum_{m_c=1}^{\infty}\frac{I_{m_c}}{3}\sin\left(m_c(\omega_c t - \theta_{cI})\right) \\ i_{m_c,w-Ax} &= \sum_{m_c=1}^{\infty}\frac{I_{m_c}}{3}\sin\left(m_c(\omega_c t - \theta_{cI})\right) \end{aligned} \tag{4.31}$$

- For phase *B* drive cells, the DC-link midpoint is connected to input phase *v*. The first and second leg midpoints (point 1 and 2) are connected to phases *w* and *u* respectively. The two legs will be modulated to follow V_{wv} and V_{uv} respectively. As a result, the input triplen and carrier harmonic currents for cell *x* in phase *B* is given by:

$$\begin{aligned} i_{3rd,u-Bx} &= I_{3rd}\sin\left(3\omega t-\phi_{I-3rd}+\frac{\pi}{2}\right) \\ i_{3rd,v-Bx} &= 0 \\ i_{3rd,w-Bx} &= I_{3rd}\sin\left(3\omega t-\phi_{I-3rd}-\frac{\pi}{2}\right) \end{aligned} \tag{4.32}$$

$$\begin{aligned} i_{m_c,u-Bx} &= \sum_{m_c=1}^{\infty}\frac{I_{m_c}}{3}\sin\left(m_c(\omega_c t-\theta_{cI})\right) \\ i_{m_c,v-Bx} &= \sum_{m_c=1}^{\infty}\frac{-2I_{m_c}}{3}\sin\left(m_c(\omega_c t-\theta_{cI})\right) \\ i_{m_c,w-Bx} &= \sum_{m_c=1}^{\infty}\frac{I_{m_c}}{3}\sin\left(m_c(\omega_c t-\theta_{cI})\right) \end{aligned} \tag{4.33}$$

- For phase *C* drive cells, the DC-link midpoint is connected to input phase *w*. The first and second leg midpoints (point 1 and 2) are connected to phases *u* and *v* respectively. The two legs will be modulated to follow V_{uw} and V_{vw} respectively. As a result, the input triplen and carrier harmonic currents for cell *x* in phase *C* is given by:

$$\begin{aligned} i_{3rd,u-Cx} &= I_{3rd}\sin\left(3\omega t-\phi_{I-3rd}-\frac{\pi}{2}\right) \\ i_{3rd,v-Cx} &= I_{3rd}\sin\left(3\omega t-\phi_{I-3rd}+\frac{\pi}{2}\right) \\ i_{3rd,w-Cx} &= 0 \end{aligned} \tag{4.34}$$

$$\begin{aligned} i_{m_c,u-Cx} &= \sum_{m_c=1}^{\infty}\frac{I_{m_c}}{3}\sin\left(m_c(\omega_c t-\theta_{cI})\right) \\ i_{m_c,v-Cx} &= \sum_{m_c=1}^{\infty}\frac{I_{m_c}}{3}\sin\left(m_c(\omega_c t-\theta_{cI})\right) \\ i_{m_c,w-Cx} &= \sum_{m_c=1}^{\infty}\frac{-2I_{m_c}}{3}\sin\left(m_c(\omega_c t-\theta_{cI})\right) \end{aligned} \tag{4.35}$$

From (4.24), and (4.30) – (4.35), the triplen and carrier harmonic components from each row cells group will cancel each other in the primary. Additionally, from (4.15) and (4.16), the fundamental capacitors' ripples and their resulting unbalance will be shifted in every cell by 120°. Therefore, they will cancel each other when summed in the primary.

4.6.4 Proposed Carrier Phase Shifting Techniques for Typical Switching Frequency Operation

a) Grid Connection Standards

Table 4.2 shows the current harmonic limits in the IEEE Std. 519-2014 [33] for general systems rated from 120 V to 69 kV. For systems that use phase-shifting or multi-pulse rectifier with pulse number higher than 6, a multiplier value is applied to the limits mentioned in Table 4.2. The multiplier value is given by:

$$Multiplier = \sqrt{\frac{q}{6}} \tag{4.36}$$

, where q is the number of pulses.

Table 4.3 shows the corresponding multiplier for the number of pulses and the non-characteristic harmonics. The multiplier can be applied as long as the non-characteristic current harmonics are kept below 25% of their limits in table 4.2.

TABLE 4.2. CURRENT HARMONIC DISTORTION LIMITS FOR SYSTEMS RATED FROM 120V TO 69KV [33].

	$3 \le h < 11$	$11 \le h < 17$	$17 \le h < 23$	$23 \le h < 35$	$35 \le h < 50$	TDD
Max. % from fundamental	4.0	2.4	1.5	0.6	0.3	5

- *h: is the individual odd harmonic order.*
- *Even harmonics are limited to 25% of the odd harmonic limits above.*
- *Current distortions that results in DC offset, e.g. half wave converters are not allowed.*

TABLE 4.3. RECOMMENDED MULTIPLIER FOR THE INCREASE OF HARMONIC LIMITS [33].

q	**Multiplier**	**Harmonics orders limited to 25% of values given in table 4.2.**
12	1.4	5, 7
18	1.7	5, 7, 11 ,13
24	2.0	5, 7, 11 ,13, 17, 19
30	2.2	5, 7, 11 ,13, 17, 19, 23, 25
↓	↓	↓

Since the FSTPI has 4 switching states instead of 8, its current harmonic distortion will be higher than that of 2L-VSI for the same switching frequency. The use of the proposed phase alternation method can improve the resultant THD. However, the switching side band harmonics with typical switching frequencies (~2 kHz) may exceed the standards given in Tables 4.2 and 4.3. As a result, much higher switching frequency (~10 kHz) is needed. However, since IGBTs are the most common switches in MV drives [2], very high switching frequencies will result in higher switching losses, lower efficiency, and more complicated and expensive heat sink design. Another way to cancel these harmonics is by using trap filters [35], which in turn increases the complexity, cost, and size of the system, and affects the system stability.

As discussed in chapter 2, different carrier shifting techniques are employed between the cells' output H-bridges to cancel the switching harmonics [2]. Emerging from this concept, two proposed methods based on phase shifting of the FSTPI carriers in different cells are proposed in this work to cancel the switching harmonics sidebands from the primary currents and to comply with the standards limits using typical switching frequency and the typical grid connecting inductor. The analysis of these harmonics is first presented to construct the necessary background.

b) Side Band Harmonics Analysis

In [34], the output waveform per leg resulting from SPWM is expressed as:

$$\begin{aligned} v_{leg} &= V_1 \sin(\omega_f t + \theta_f) \\ &+ \sum_{m_c=1}^{\infty} V_{m_c} * \sin\left(m_c \frac{\pi}{2}\right) * \cos\left[m_c(\omega_c t + \theta_c)\right] \\ &+ \sum_{m_c=1}^{\infty} \sum_{\substack{n_c=-\infty \\ n_c \neq 0}}^{\infty} V_{m_c n_c} * \sin\left[(m_c + n_c)\frac{\pi}{2}\right] * \cos\left[m_c(\omega_c t + \theta_c) + n_c(\omega_f t + \theta_f)\right] \end{aligned} \quad (4.37)$$

, where ω_f and ω_c are the fundamental and carrier angular frequencies respectively, θ_f and θ_c are the fundamental and carrier angles, and m_c and n_c are the carrier and sideband indices.

The first term in (4.37) is the desired fundamental voltage. The second term is the carrier harmonics discussed before, they contain only odd harmonics. They can be cancelled using the proposed phase alternation connection to the cells. The third term is the sideband harmonics, their phase-shift depends on the fundamental angle as well as the carrier angle. In the FSTPI AFE shown in Fig. 4.5, the two legs are always controlled with fundamental phase shift of 60 degrees. Therefore, the carrier sidebands terms for the two legs become:

$$\begin{aligned} v_{13-m_c n_c} &= \sum_{m_c=1}^{\infty} \sum_{\substack{n_c=-\infty \\ n_c \neq 0}}^{\infty} V_{m_c n_c} * \sin\left[(m_c + n_c)\frac{\pi}{2}\right] * \cos\left[m_c(\omega_c t + \theta_c) + n_c(\omega_f t + \theta_{f13})\right] \\ v_{23-m_c n_c} &= \sum_{m_c=1}^{\infty} \sum_{\substack{n_c=-\infty \\ n_c \neq 0}}^{\infty} V_{m_c n_c} * \sin\left[(m_c + n_c)\frac{\pi}{2}\right] * \cos\left[m_c(\omega_c t + \theta_c) + n_c(\omega_f t + \theta_{f13} - 60^o)\right] \\ v_{12-m_c n_c} &= v_{13-m_c n_c} - v_{23-m_c n_c} \end{aligned} \quad (4.38)$$

, where θ_{f13} is the first leg fundamental angle.

The first harmonic group side bands with m_c=1, and n_c= ±2 are the highest in magnitude. In this case (4.38) becomes:

$$\begin{aligned} v_{13(1,\pm2)} &= V_{1,\pm2}\cos\left[\left(\omega_c \pm 2\omega_f\right)t + \theta_c \pm 2\theta_{f13}\right] \\ v_{23(1,\pm2)} &= V_{1,\pm2}\cos\left[\left(\omega_c \pm 2\omega_f\right)t + \theta_c \pm 2\theta_{f13} \mp 120^o\right] \\ v_{12(1,\pm2)} &= \sqrt{3}V_{1,\pm2}\cos\left[\left(\omega_c \pm 2\omega_f\right)t + \theta_c \pm 2\theta_{f13} \pm 30^o\right] \end{aligned} \tag{4.39}$$

The resulting phase harmonics from (4.39) are calculated as:

$$\begin{aligned} v_{1(1,\pm2)} &= \frac{v_{13(1,\pm2)} + v_{12(1,\pm2)}}{3} \\ &= \frac{\sqrt{7}}{3}V_{1,\pm2}\cos\left[\left(\omega_c \pm 2\omega_f\right)t + \theta_c \pm 2\theta_{f13} \pm 19.1^o\right] \\ v_{2(1,\pm2)} &= \frac{v_{23(1,\pm2)} - v_{12(1,\pm2)}}{3} \\ &= \frac{\sqrt{7}}{3}V_{1,\pm2}\cos\left[\left(\omega_c \pm 2\omega_f\right)t + \theta_c \pm 2\theta_{f13} \mp 139.1^o\right] \\ v_{3(1,\pm2)} &= \frac{-v_{13(1,\pm2)} - v_{12(1,\pm2)}}{3} \\ &= \frac{1}{3}V_{1,\pm2}\cos\left[\left(\omega_c \pm 2\omega_f\right)t + \theta_c \pm 2\theta_{f13} \pm 120^o\right] \end{aligned} \tag{4.40}$$

From (4.40), the following can be concluded for m_c=1, n_c = ±2 phase sideband harmonics voltages and resulting currents:

- The system is balanced per one cell and for the same θ_{f13}. However, their dependency on $2\theta_{f13}$ hinders the cancellation capability using phase alternation. This is because θ_{f13} in phase alternated cells is shifted by $\pm 120^o$. This additional phase shift violates the system balancing equations.
- Their angle depends on the carrier angle θ_c.

For the second harmonic group side bands (m_c=2, n_c= ±1), (4.38) becomes:

$$\begin{aligned} v_{13(2,\pm1)} &= V_{2,\pm1}\cos\left[\left(2\omega_c \pm \omega_f\right)t + 2\theta_c \pm \theta_{f13}\right] \\ v_{23(2,\pm1)} &= V_{2,\pm1}\cos\left[\left(2\omega_c \pm \omega_f\right)t + 2\theta_c \pm \theta_{f13} \mp 60^o\right] \\ v_{12(1,\pm1)} &= V_{2,\pm1}\cos\left[\left(2\omega_c \pm \omega_f\right)t + 2\theta_c \pm \theta_{f13} \pm 60^o\right] \end{aligned} \tag{4.41}$$

The resulting phase harmonics from (4.41) are:

$$\begin{aligned} v_{1(2,\pm1)} &= \frac{v_{13(2,\pm1)} + v_{12(2,\pm1)}}{3} = \frac{1}{\sqrt{3}}V_{1,\pm2}\cos\left[\left(2\omega_c \pm \omega_f\right)t + 2\theta_c \pm \theta_{f13} \pm 30^o\right] \\ v_{2(2,\pm1)} &= \frac{v_{23(1,\pm2)} - v_{12(1,\pm2)}}{3} = \frac{1}{\sqrt{3}}V_{1,\pm2}\cos\left[\left(2\omega_c \pm \omega_f\right)t + 2\theta_c \pm \theta_{f13} \mp 90^o\right] \\ v_{3(2,\pm1)} &= \frac{-v_{13(1,\pm2)} - v_{12(1,\pm2)}}{3} = \frac{1}{\sqrt{3}}V_{1,\pm2}\cos\left[\left(2\omega_c \pm \omega_f\right)t + 2\theta_c \pm \theta_{f13} \pm 150^o\right] \end{aligned} \tag{4.42}$$

From (4.42), the following can be concluded for m_c=1, n_c= ±2 phase voltage and current sideband harmonics

- The system is balanced per one cell. The currents are phase shifted by $\mp 120^o$ However, as their angle also depends on θ_{f13}, they cannot be cancelled using the phase alternation method.
- Their angle also depends on the double of the carrier angle $2\theta_c$.

The previous analysis examples show that phase alternation connection alone cannot cancel the sidebands harmonics. Nevertheless, their carrier angle dependency adds another degree of freedom that can be used.

c) Proposed Method I for Switching Sidebands Cancellation:

Carrier Phase-Shifting in case of Phase-Shifting Transformer Interface

For a (2*k*+1) level CHB that uses a phase-shifting transformer in its interface with the grid, each secondary winding set of index *x* has a different fundamental phase shifting angle of δ_x. The reflected current sideband harmonics from arbitrary cell in the primary phase *j* are given by:

$$i_{jx(m_c,n_c)} = \sum_{m_c=1}^{\infty} \sum_{\substack{n_c=-\infty \\ n_c \neq 0}}^{\infty} I_{jx(m,n)} \sin\left[\left(m_c\omega_c + n_c\omega_f\right)t + m_c\theta_{cx} + n_c(\theta_{Ix} + \delta_{Ix})\right] \tag{4.43}$$

, where $I_{jx(m_c,n_c)}$ is the magnitude of the reflected current harmonics from cell *x* to the primary phase j, θ_{cx} is the carrier angle used for cell *x*, θ_{Ix} is the current fundamental phase angle depending on the phase sequence used for the cell, and δ_{Ix} is the current fundamental phase angle depending on the secondary winding group phase shift.

For *k* cells/phase, the total primary sideband harmonics in phase *j* are given by:

$$i_{pj} = \sum_{x=1}^{3k} i_{jx} \tag{4.44}$$

Based on the harmonic analysis and from (4.43) and (4.44), for *S* considered cells, sidebands can only be cancelled from the primary current under three conditions:

1. The same phase sequence connection is used for the considered cells (same θ_{Ix}).
2. The cells are connected to the same secondary winding set to have the same phase-shift (same δ_{Ix}).

3. The carrier signals are phase shifted by $360^o/S$, so that the sum of their vectors is equal to zero in primary.

These conditions can be achieved by using the proposed cell arrangement shown in Fig. 4.10. The first two conditions are satisfied by connecting the three row cells to the same phase sequence and the same secondary windings set. To satisfy the third condition, the carrier signals for row cells are phase-shifted by 120°. The phase sequence is alternated between different column cells to minimize the triplen order harmonics.

The proposed carrier shifting technique and cell arrangement can:

- Cancel carrier and sideband harmonics for any harmonic group of index (m_c) not a multiple of three.
- Reduce the triplen harmonics and the unbalance effect, since the phase alternation is now between cells with different fundamental phase-shifts.

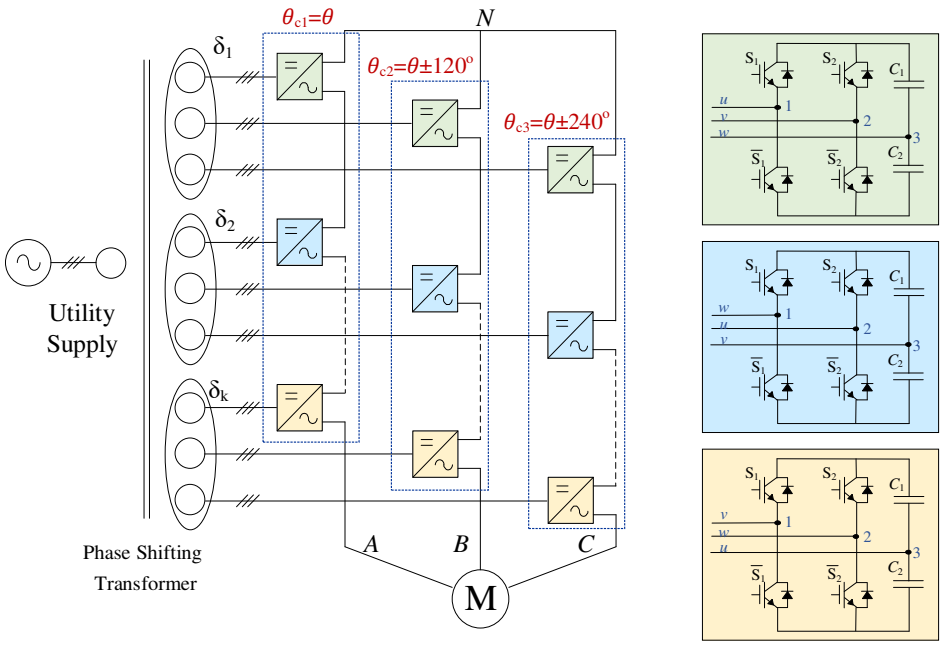

Fig. 4.10. Proposed Method I for Sideband Harmonics Cancellation in case of Phase-Shifting Transformer Interface.

d) Proposed Method II for Switching Sidebands Cancellation:

Carrier Phase-Shifting in case of Multi-Winding Transformer Interface

The limitation of the previous method was originally caused by the different phase-shifting angles between the secondary winding sets. However, the use of AFE instead of DFE dismisses the necessity of using phase-shifting transformer due to the absence of low order harmonics (5^{th}, 7^{th}, etc…). As a result, a multi-winding transformer can be used, where all the secondary winding sets have the same phase shift.

The reflected currents in (4.43) now become:

$$i_{jx(m_c,n_c)} = \sum_{m_c=1}^{\infty} \sum_{\substack{n_c=-\infty \\ n_c \neq 0}}^{\infty} I_{jx(m,n)} \sin\left[\left(m_c\omega_c + n_c\omega_f\right)t + m_c\theta_{cx} + n_c(\theta_{Ix} + \delta_I)\right] \tag{4.45}$$

In (4.45), the fundamental phase-shift only depends on the phase-sequence used. Fig. 4.11 shows the proposed cell arrangement for $2k$+1 level CHB drive and carrier shifting required to cancel the sideband harmonics. It is the same cell arrangement as Fig. 4.9. Hence, the column cells will have the same phase sequence and fundamental phase angle, while the carriers are phase-shifted by $360^o/k$.

As a result, this technique can:

- Cancel side band harmonics for any harmonic group of index (m_c) not a multiple of three.
- Cancel all carrier harmonics.
- Cancel triplen low order harmonics for any number of cells.
- Eliminate the unbalance from the primary currents for any number of cells.

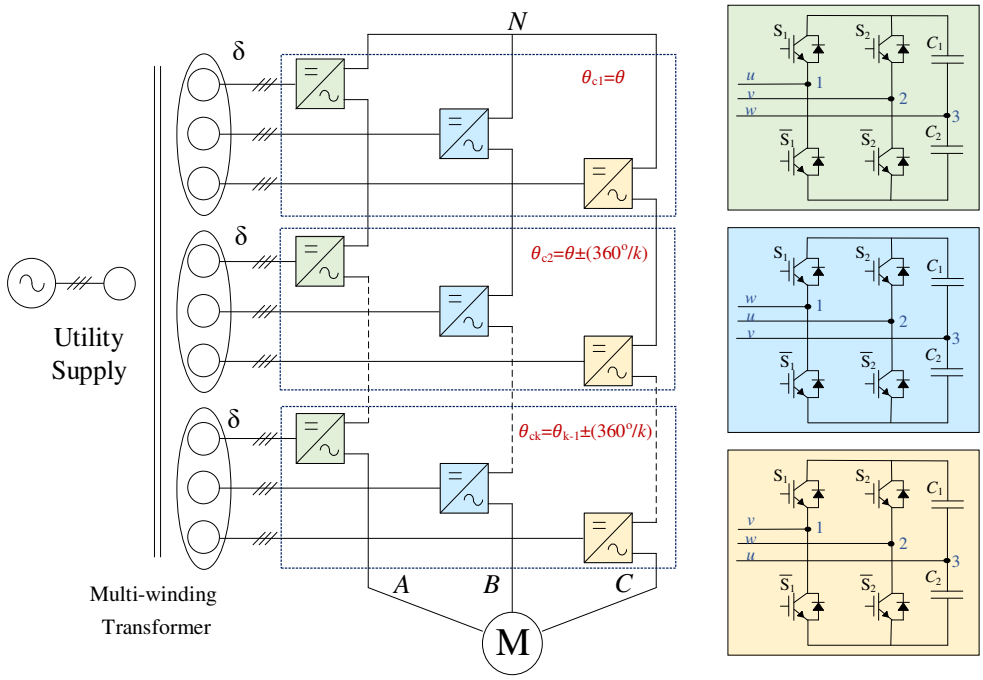

Fig. 4.11. Proposed Method II for Sideband Harmonics Cancellation in case of Multi-Winding Transformer Interface.

4.6.5 Third Order Harmonic Injection Capability

The cancellation of triplen harmonics using the phase-alternation method has paved the way for SPWM with third order harmonic injection in the FSTPI. Like 2L-VSI, it can increase the DC-link utilization by 15.5%. Following is the analysis of the proposed configuration AFE performance using SPWM with third order harmonic injection.

a) Modulation and Switching

For the FSTPI shown in Fig. 4.12, the switching states in (4.7) are modified to be:

$$\begin{aligned} S_{1'} &= 0.5\left[1+m\sin\left(\omega t-\varphi_{13}\right)+k_3 m\sin(3\omega t-3\varphi_{13})\right] \\ \overline{S_{1'}} &= 1-S_{1'} \\ S_{2'} &= 0.5\left[1+m\sin\left(\omega t-\varphi_{23}-\frac{\pi}{3}\right)+k_3 m\sin(3\omega t-3\varphi_{23}-\pi)\right] \\ \overline{S_{2'}} &= 1-S_{2'} \end{aligned} \tag{4.46}$$

, where k_3 is the per unit of third order harmonic injected with respect to the fundamental.

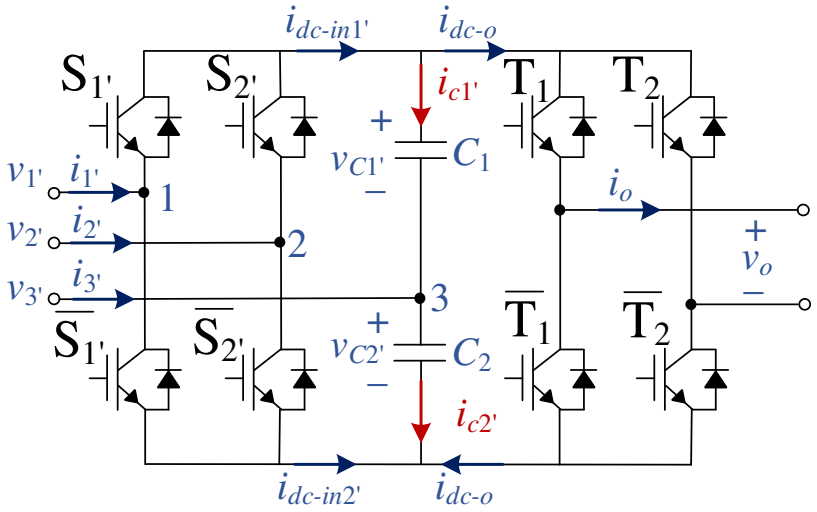

Fig. 4.12. Power Cell with FSTPI-AFE Third Order Harmonic Injection Modulation.

From (4.9) and (4.26), the corresponding phase currents will be:

$$\begin{aligned} i_{1'} &= I_1 \sin\left(\omega t - \theta_{I1}\right) + I_{3rd} \sin(3\omega t - \theta_{I3rd}) \\ i_{2'} &= I_1 \sin\left(\omega t - \theta_{I1} - \frac{2\pi}{3}\right) + I_{3rd} \sin(3\omega t - \theta_{I3rd} - \pi) \\ i_{3'} &= I_1 \sin\left(\omega t - \theta_{I1} + \frac{2\pi}{3}\right) \end{aligned} \tag{4.47}$$

, where I_1 and I_{3rd} are the magnitudes of the current fundamental and third order harmonic components, and θ_{I1} and θ_{I3rd} are their corresponding phase shift.

b) Capacitors' Ripples

In case of third order harmonic injection, (4.10) is modified to become:

$$\begin{bmatrix} i_{dc-in1'} \\ i_{dc-in2'} \end{bmatrix} = \begin{bmatrix} S_{1'} & S_{2'} \\ \overline{S_{1'}} & \overline{S_{2'}} \end{bmatrix} \begin{bmatrix} i_{1'} \\ i_{2'} \end{bmatrix} \tag{4.48}$$

However, the third order harmonic current component effect on the capacitors is much lower than the fundamental component due to the effective capacitor impedance at high frequencies.

As a result, (4.48) can be simplified to be:

$$\begin{bmatrix} i_{dc-in1'} \\ i_{dc-in2'} \end{bmatrix} = \begin{bmatrix} S_{1'} & S_{2'} \\ \overline{S_{1'}} & \overline{S_{2'}} \end{bmatrix} \begin{bmatrix} i_1 \\ i_2 \end{bmatrix} \tag{4.49}$$

, where i_1 and i_2 are the fundamental input currents.

By substitution with (4.46) and (4.47) in (4.48), the DC-link input currents are:

$$\begin{aligned} i_{dc-in1'} &= i_{dc-in1} + I_{2\omega}\cos(2\omega t + 3\varphi_{13} + \theta_{I,2\omega}) + I_{4\omega}\cos(4\omega t + 3\varphi_{13} + \theta_{I,4\omega}) \\ i_{dc-in2'} &= i_{dc-in2} + I_{2\omega}\cos(2\omega t + 3\varphi_{13} + \theta_{I,2\omega}) + I_{4\omega}\cos(4\omega t + 3\varphi_{13} + \theta_{I,4\omega}) \end{aligned} \tag{4.50}$$

, where i_{dc-in1} and i_{dc-in2} are the DC-link input current in case of no third order harmonic injection, $I_{2\omega}$ and $I_{4\omega}$ are the magnitudes of the second and fourth order harmonics, and $\theta_{I,2\omega}$ and $\theta_{I,4\omega}$ are the second and fourth harmonics phase shifts, they depend on θ_{I1}.

The capacitor voltages are:

$$\begin{aligned} v_{c1'} &= \frac{1}{C_1}\int i_{c1'}dt \\ v_{c2'} &= \frac{1}{C_2}\int i_{c2'}dt \end{aligned} \tag{4.51}$$

From (4.50) and (4.51), the DC-link capacitors will contain additional ripples of second and fourth harmonic orders due to third order harmonic injection. Unlike the fundamental ripples, these capacitors even harmonics are in phase and will not cancel each other from the DC-link voltage.

c) Cell Input Current Ripples

The line-to-line voltages are given by:

$$\begin{bmatrix} v_{13'} \\ v_{23'} \end{bmatrix} = \begin{bmatrix} S_{1'} & \overline{S_{1'}} \\ S_{2'} & \overline{S_{2'}} \end{bmatrix} \begin{bmatrix} v_{C1'} \\ v_{C2'} \end{bmatrix} \tag{4.52}$$

The interaction between switching states with the 2nd and 4th harmonic DC-link ripples will result in additional 3rd, 5th and 7th order current harmonics. From (4.46), (4.50), (4.51) in (4.52), the additional 3rd, 5th and 7th phase harmonics are:

$$\begin{aligned} v_{1'-3rd} &= V_{3rd'} \sin(3\omega t + 4\varphi_{13} + \theta_{I,2\omega} - 19.1^o) \\ v_{2'-3rd} &= V_{3rd'} \sin(3\omega t + 4\varphi_{13} + \theta_{I,2\omega} + 139.1^o) \\ v_{3'-3rd} &= V_{3rd'} \sin(3\omega t + 4\varphi_{13} + \theta_{I,2\omega} - 120^o) \end{aligned} \tag{4.53}$$

$$\begin{aligned} v_{1'-5th} &= V_{5th-1} \sin(5\omega t + 4\varphi_{13} + \theta_{I,4\omega} - 19.1^o) \\ &\quad + V_{5th-3} \sin(5\omega t + 6\varphi_{13} + \theta_{I,2\omega} - 30^o) \\ v_{2'-5th} &= V_{5th-1} \sin(5\omega t + 4\varphi_{13} + \theta_{I,4\omega} + 139.1^o) \\ &\quad + V_{5th-3} \sin(5\omega t + 6\varphi_{13} + \theta_{I,2\omega} + 150^o) \\ v_{3'-5th} &= 1/\sqrt{7}\, V_{5th-1} \sin(5\omega t + 4\varphi_{13} + \theta_{I,4\omega} - 120^o) \end{aligned} \tag{4.54}$$

$$\begin{aligned} v_{1'-7th} &= V_{7th} \sin(7\omega t + 6\varphi_{13} + \frac{\pi}{6} + \theta_{I,4\omega}) \\ v_{2'-7th} &= V_{7h} \sin(7\omega t + 6\varphi_{13} - \frac{5\pi}{6} + \theta_{I,4\omega}) \\ v_{3'-7th} &= 0 \end{aligned} \tag{4.55}$$

, where $V_{3rd'}$ is the additional 3rd order harmonic magnitude resulting from the interaction between the fundamental modulation components and 2nd order harmonic capacitors' ripples, $V_{5th\text{-}1}$ is the 5th order harmonic magnitude from the interaction between fundamental modulation components and 4th order harmonic capacitors' ripples, $V_{5th\text{-}3}$ is the 5th order

harmonic magnitude from the interaction between 3rd order harmonic modulation component and 2nd order harmonic capacitors' ripples, and V_{7th} is the 7th order harmonic magnitude from the interaction between 3rd order harmonic modulation component and 4th order harmonic capacitors' ripples.

(4.53) shows the additional 3rd harmonics resulted from the interaction between the fundamental switching states and the 2nd order harmonic capacitors' ripples. These components cannot be cancelled using phase alternation due to their angle dependency on $\theta_{I,2\omega}$, which in turn depends on the first leg fundamental current angle, and $4\varphi_{13}$. However, the use of typical phase-shifting transformer along with phase alternation method can minimize these harmonics to fall below the standards limits. The first term in (4.54) is the 5th harmonic component resulting from the interaction between the fundamental switching states and the 4th order capacitors' ripples. It follows the same analysis as the additional 3rd order harmonics aforementioned.

The second term in (4.54) represents the 5th order harmonics resulting from the interaction between 3rd order harmonics switching states with 2nd order harmonic capacitors' ripples. (4.55) represents the 7th order harmonics due to interaction of 3rd order harmonic switching states with 4th order harmonic capacitors' ripples. The dependency of these two components on the current angles violates their cancellation using phase alternation method. Since the current angles $\theta_{I,2\omega}$ and $\theta_{I,4\omega}$ depend on the fundamental current angle in leg 1 (θ_{I1}), the phase shift in θ_{I1} by 120° in phase alternated cells will oppose the cancellation of these harmonics vectors in the primary. However, due to their dependency on $6\varphi_{13}$, these harmonics can be cancelled using the phase shifting transformer

concept, similar to the DFE harmonics cancellation. Therefore, phase-shifting transformer is needed to cancel these harmonics in case of using SPWM with third order harmonic injection.

d) Harmonic Cancellation

From the previous analysis, the following points can be concluded for harmonic cancellation in the primary currents when third order harmonic injection is used:

1. To eliminate third order harmonics, the proposed phase alternation connection illustrated in Fig. 4.9 must be used.
2. To cancel odd non-tiplen order harmonics, phase-shifting transformer must be used.
3. Total sideband harmonics cancellation cannot be satisfied using the proposed carrier phase-shifting methods. This is because the cancellation conditions are now violated due to different shifting angles in the transformer. However, research into minimization of these harmonics using optimization methods is good topic for future research.

4.6.6 FSTPI AFE Controller

Fig. 4.13 shows the controller scheme used. As the 2L-VSI controller, it comprises DC-link voltage controlling loop, and current controlling loop.

The measured average DC-link voltage V_{dc} is compared with the reference value $V_{dc\text{-}ref}$, the error is fed to the DC-voltage controller block. A PI controller is used to eliminate the error to zero by setting the reference active power (P_{ref}) to be supplied from or to the AFE. The reference reactive (Q_{ref}) power is set to be zero for unity power factor operation.

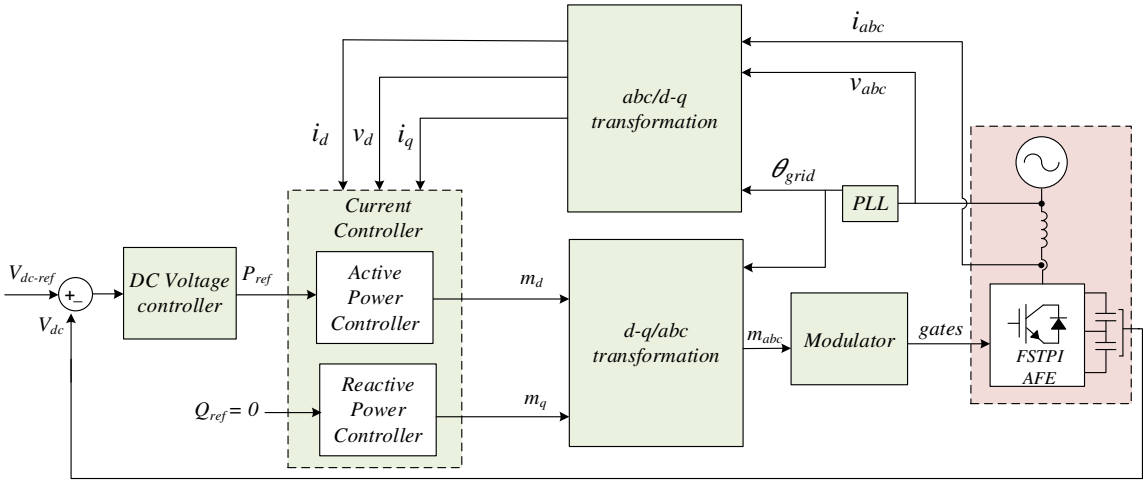

Fig. 4.13. FSTPI AFE Controller.

As it is a three-phase system, using DC-components in the rotating *d-q* reference frame is applicable. PLL is used to estimate the grid angle (θ_{grid}) from the measured line voltages. This angle is then used to transform the AC grid voltages and line currents to DC components in *d-q* frame (v_d, v_q, i_d, and i_q). In this transformation, v_d is aligned with the grid voltage. Therefore, there is no v_q component for the grid voltage ($v_q = 0$). The reference active and reactive power values are used to set the reference current components using the following active and reactive power equations in *d-q* frame [13]:

$$P_{ref} = \frac{3}{2}(v_d * i_{d-ref} + v_q * i_{q-ref})$$
$$Q_{ref} = \frac{3}{2}(v_q * i_{d-ref} - v_d * i_{q-ref}) \quad (4.56)$$

The measured currents are then compared with the reference values. The error of each comparison is fed to a PI controller that sets the required modulation components (m_d and m_q) to make the error equal to zero. The *d-q* modulation components are then fed to *d-q* to *abc* transformation block to have balanced three-phase modulating signals.

As shown, the controller scheme is the same used for 2L-VSI AFE. The only difference is in the modulator. The three-phase modulating signals are transformed to two line-to-line modulating signals using (4.3) before the comparison with the carrier signals.

4.6.7 Switches Ratings

The voltage ratings of the FSTPI-AFE switches will be the same as the 2L-VSI inverter, since both power cells employ H-bridge inverter in the output. However, to keep the same power rating, equation (4.57) must be satisfied.

$$\begin{aligned} P_{2L-VSI} &= P_{FSTPI} \\ \sqrt{3}V_{l-l,2L-VSI}I_{2L-VSI} &= \sqrt{3}V_{l-l,FSTPI}I_{FSTPI} \end{aligned} \tag{4.57}$$

The current rating of FSTPI switches must be increased to compensate for the lower DC-link utilization, which depends on the modulation method used:

- **In SPWM,** the maximum FSTPI output voltage is:

$$V_{l-l,FSTPI} = 0.35V_{dc} \tag{4.58}$$

  By substitution in (4.57), the current should be double the 2L-VSI current.

- **In SPWM with third order harmonic injection,** the maximum FSTPI output voltage is:

$$V_{l-l,FSTPI} = 0.4V_{dc} \tag{4.59}$$

The fundamental current rating should be increased by 77% from the 2L-VSI. However, due to the existing odd harmonics, the rating should be kept at double the 2L-VSI current.

4.7 Simulation Studies

To verify the theoretical analysis, simulation studies for a seven level 3kV/160A regenerative FSTPI-AFE based CHB drive model were conducted. The load is an FOC-controlled induction motor. Table 4.4 shows the system parameters, per unit values are based on system base values.

TABLE 4.4. PROPOSED REDUCED SWITCH-COUNT CONFIGURATION SIMULATION STUDIES SYSTEM PARAMETERS.

Grid Voltage	3 kV
Rated output current	160 A
Nominal frequency	60 Hz
Switching frequency	1980 Hz (33* 60)
Grid-connecting filter	5%
DC reference voltage	1300 V
FSTPI input voltage	• 300 V (SPWM) • 300*1.15 (3rd harmonic injection)
Capacitor value	8000 µF (50 µF/A)
Number of motor pole pairs	3
Motor rated speed	1192 rpm

4.7.1 Inherent Capacitors Voltage Balancing

To first test the inherent voltage balancing capability against induced changes, a resistance is connected across C_2 in one of the power cells to induce dynamic disturbance and then it was removed. Fig. 4.14 shows the inherent voltage balancing capability of the proposed configuration. The two capacitors converged to their nominal values right after the resistance removal.

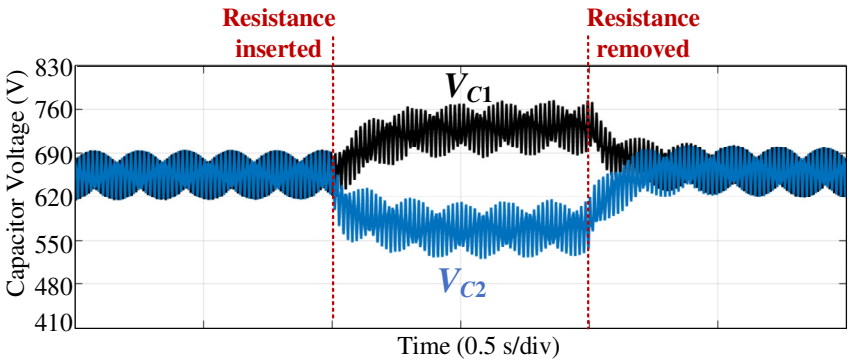

Fig. 4.14. Proposed Configuration Inherent Capacitors' Voltage Balance.

4.7.2 Inherent Low Order Harmonic Cancellation

Low order harmonics show considerably in the input current harmonics in case of low speed operation. To investigate their inherent cancellation, the motor was run at 0.2 p.u. speed which corresponds to output frequency of 12 Hz. Fig. 4.15 shows the secondary and primary current harmonics at this condition. The secondary currents contain low order harmonic of $\omega_{in} \pm 2\omega_{out}$. However, the low order harmonics are inherently cancelled in the primary current due to the three-phase interface.

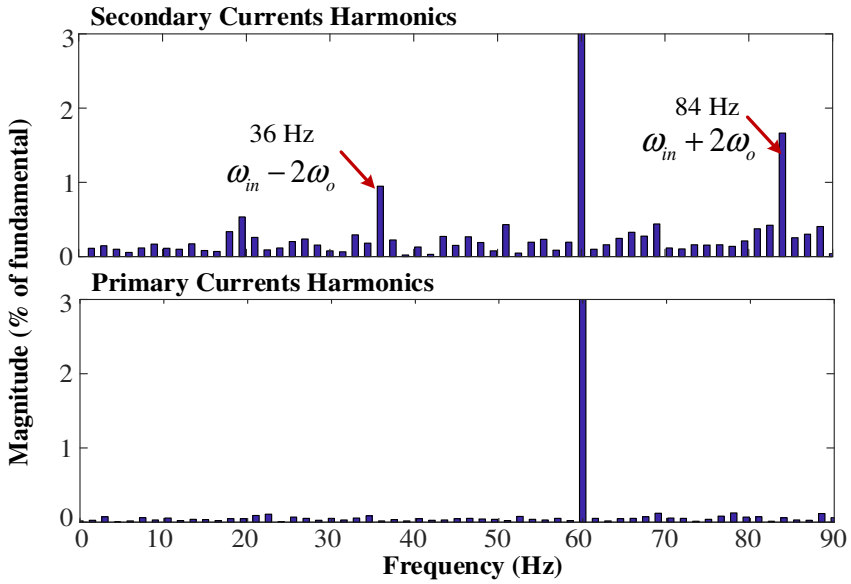

Fig. 4.15. Proposed Configuration Secondary and Primary Currents Low Order Harmonics at 0.2 p.u. Speed.

4.7.3 Regular SPWM Modulation Operation

Fig. 4.16 shows overall system performance using regular SPWM modulation. The motor was operated in rated motoring and regeneration conditions using FOC scheme. Input reactive power is zero indicating unity power factor. Input cell current has very good dynamic response during transitions. DC-link voltage is controlled during the whole operation at the reference value of 1300V, while the two capacitor's voltages are at 650V.

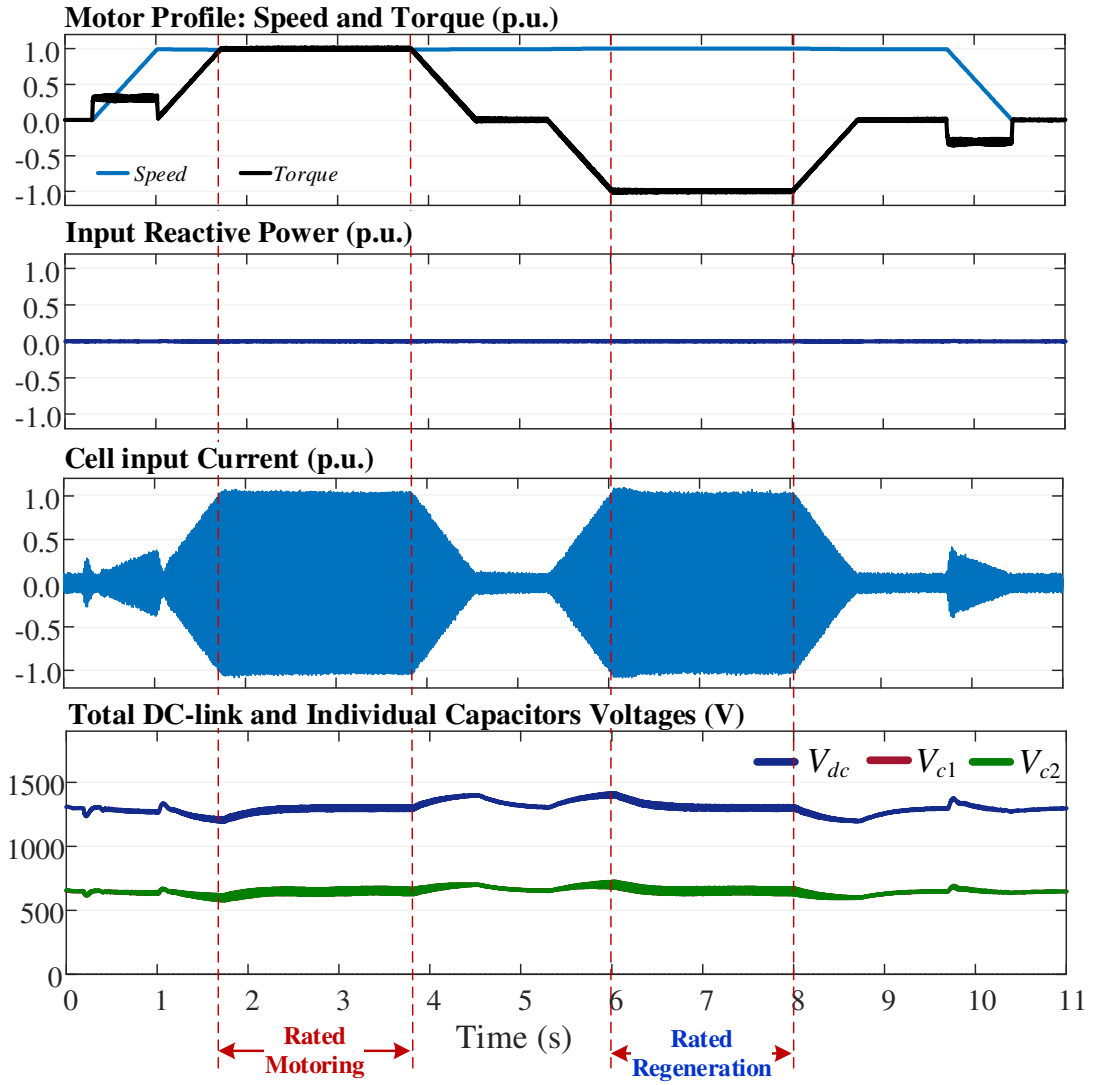

Fig. 4.16. Motor Profile, Input Reactive Power, Cell Input Current, Total DC-Link and Individual Capacitors' Voltages in Proposed Regenerative CHB Drive with Regular SPWM.

a) DC-Link Capacitors Ripples

Fig. 4.17 and 4.18 focus on the total DC-link and capacitors' voltages in case of SPWM during rated motoring and regeneration. Their harmonic spectra is shown in Fig. 4.19. Both of them contain input fundamental harmonics and output second order harmonics around 120 Hz at rated speed. The individual capacitors input fundamental ripples will cancel each other when added and do not show on the whole DC-link voltage. The DC-link ripples magnitude is 0.8%.

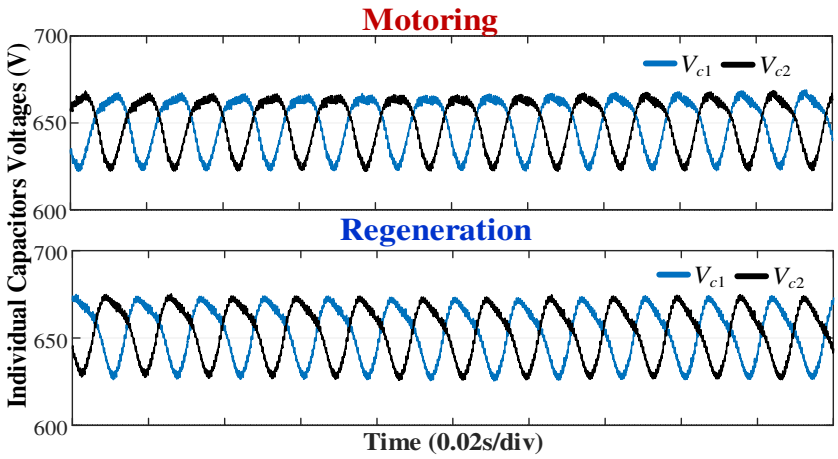

Fig. 4.17. Capacitor Voltages during Motoring and Regeneration in Proposed Regenerative CHB Drive with Regular SPWM.

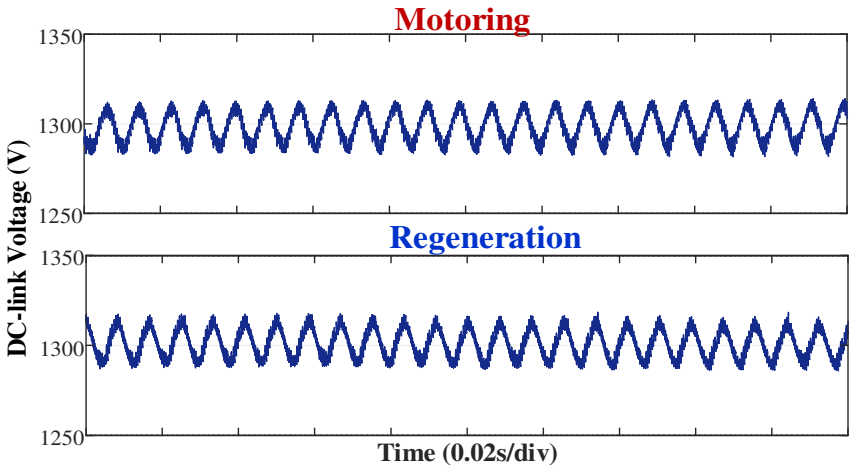

Fig. 4.18. DC-Link Voltage during Motoring and Regeneration in Proposed Regenerative CHB Drive with Regular SPWM.

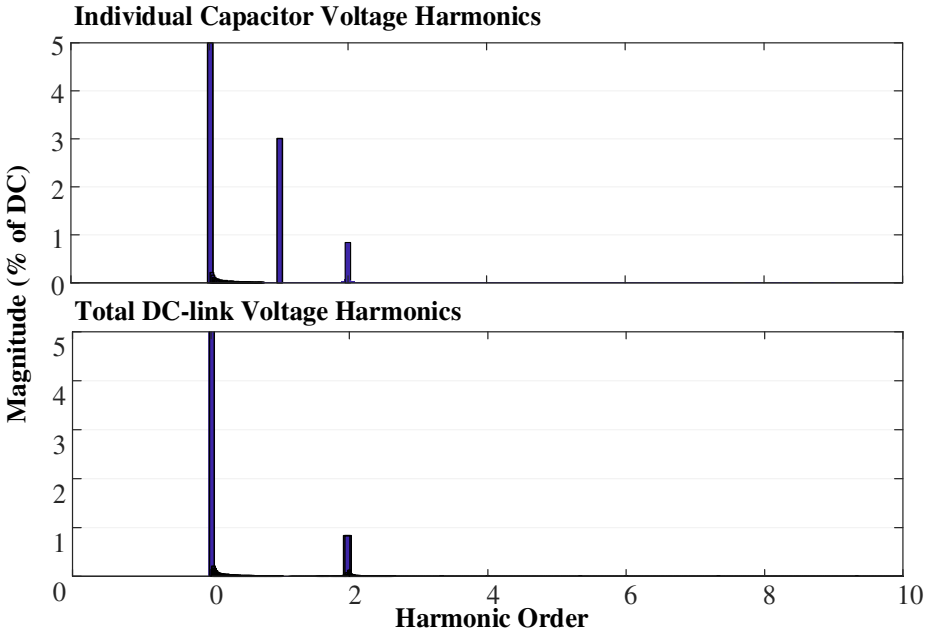

Fig. 4.19. Capacitors and DC-Link Voltages Harmonics in Proposed Regenerative CHB Drive with Regular SPWM.

b) Secondary and Primary Currents Harmonic Analysis

Fig. 4.20 and 4.21 show the harmonic waveforms and spectra of rated secondary and primary currents using phase-shifting transformer when no phase alternation or carrier phase-shifting is used. The DC-link midpoint connection is to phase *w*. The switching frequency is 1980 Hz (33*60 Hz).As discussed, the unbalance, third order harmonic component due to DC-link ripples and carrier harmonics are reflected in the primary. The switching harmonics exceeds the standards mentioned in tables 4.2 and 4.3, hence they need to be cancelled. The secondary current THD is 6% while the primary current THD is 5%.

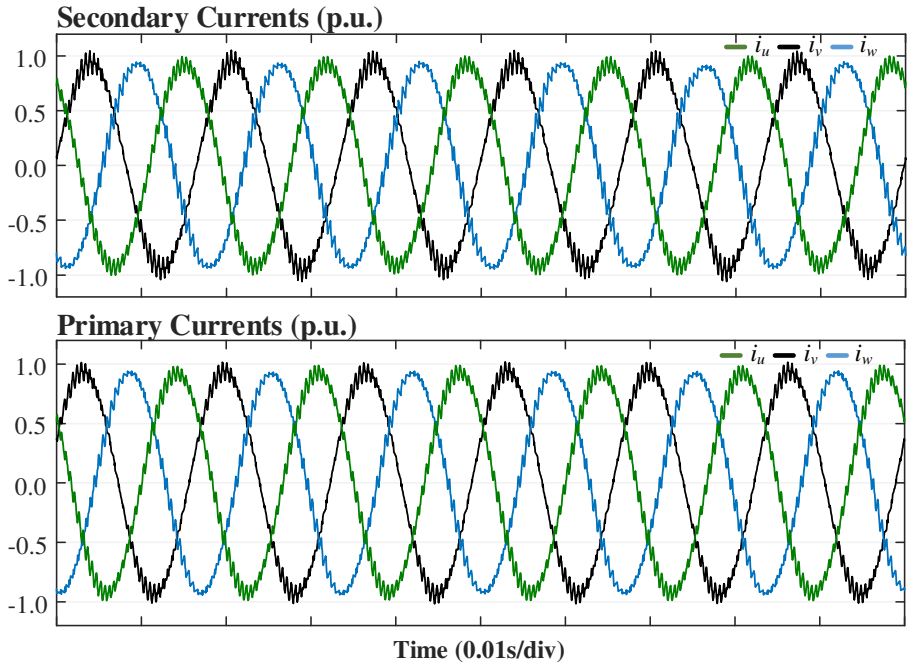

Fig. 4.20. Secondary and Primary Currents in case of No Phase Alternation or Carrier Phase Shifting in Proposed Regenerative CHB Drive with Regular SPWM.

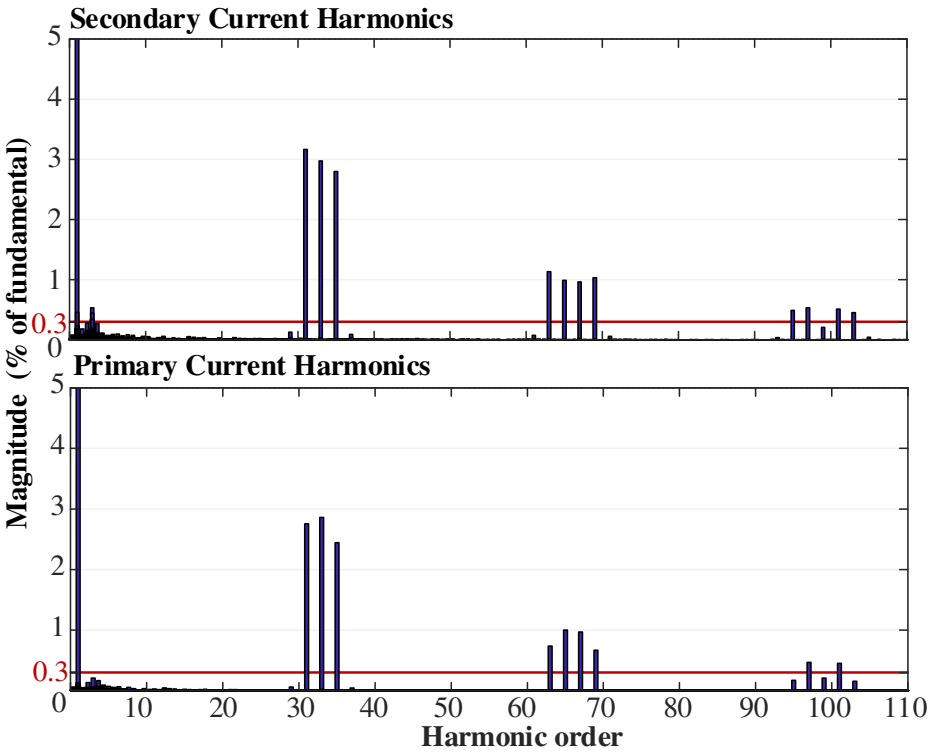

Fig. 4.21. Secondary and Primary Harmonics in case of No Phase Alternation or Carrier Phase Shifting in Proposed Regenerative CHB Drive with Regular SPWM.

c) Proposed Phase Alternation for Unbalance, Third Order Harmonics, and Carrier Harmonics Elimination from the Primary Currents

Fig. 4.22 shows the primary current harmonics using SPWM with the phase alternation method proposed in Fig. 4.9. In comparison with the primary harmonics in Fig. 4.21, the third order harmonics and carrier harmonics are eliminated. Hence, the THD drops from 5% to 2.4%. The sideband harmonics are not eliminated though and exceed the standards limits, as discussed. The primary currents waveforms are shown in Fig. 4.23, indicating the three currents to be balanced.

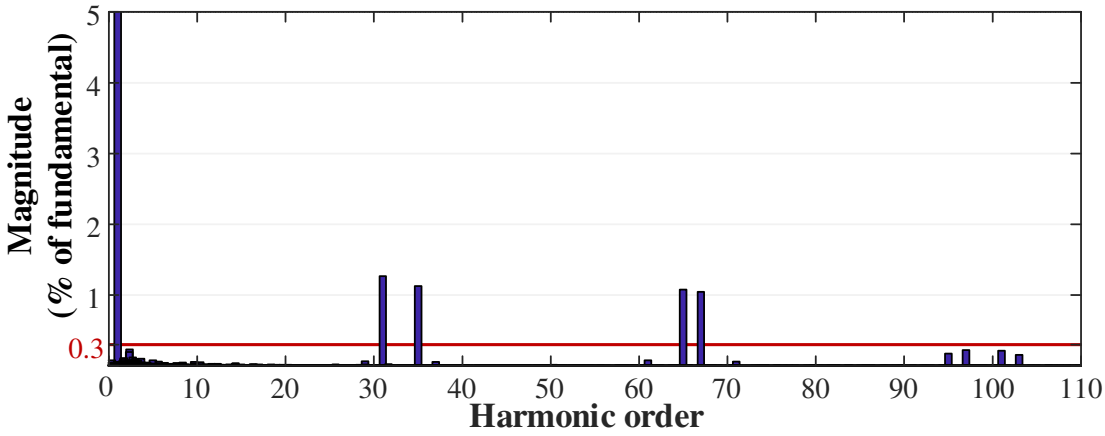

Fig. 4.22. Primary Currents Harmonics using Proposed Phase Alternation Method in Proposed Regenerative CHB Drive with Regular SPWM.

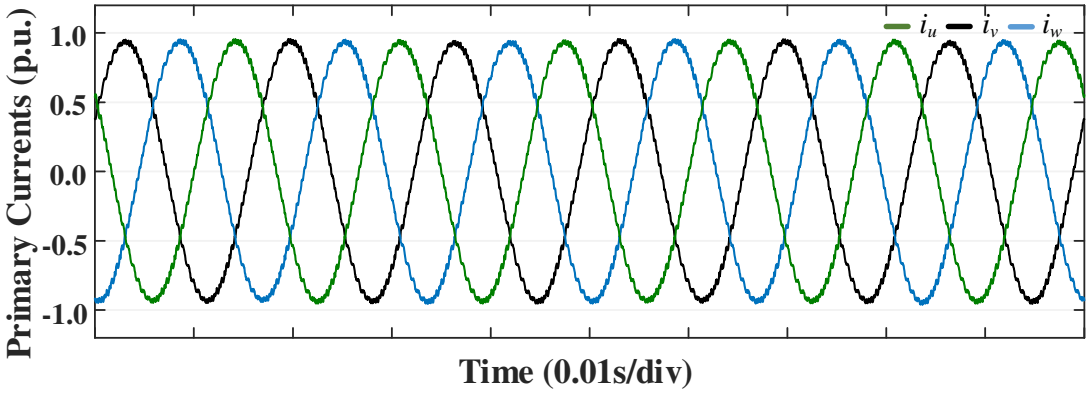

Fig. 4.23. Primary Currents using Proposed Phase Alternation Method in Proposed Regenerative CHB Drive with Regular SPWM.

d) Proposed Carrier Shifting Method I for Sideband Harmonics Elimination

Fig. 4.24 shows the primary harmonics when the proposed carrier shifting method I is used with SPWM technique for phase-shifting transformer interface. As discussed, the first harmonic group to appear is for m_c=3, and is kept below the standard limits (<0.3%). Third order harmonics due to DC-link ripples are not cancelled but reduced to be much lower than the standards limits. The THD is improved to be 0.67%.

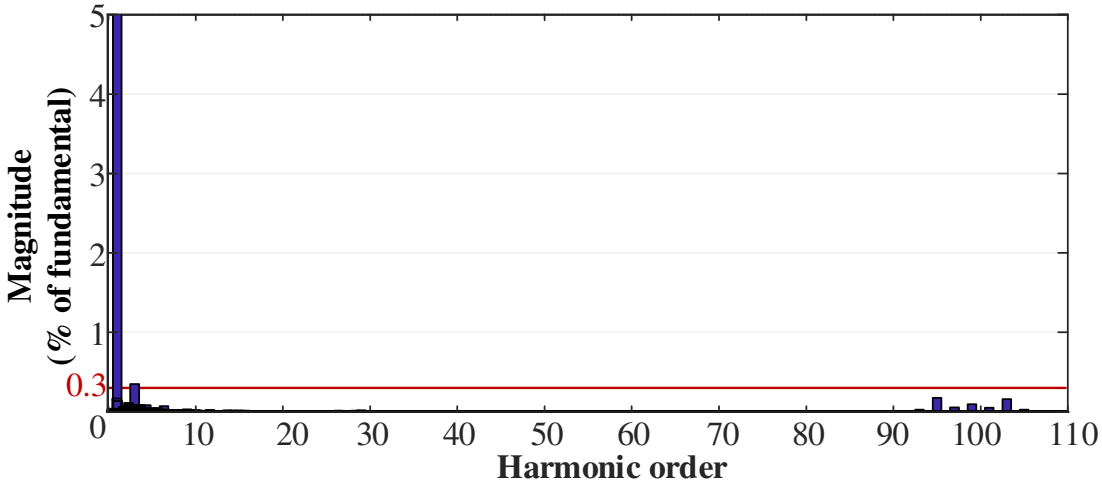

Fig. 4.24. Primary Currents Harmonics using Carrier Shifting Proposed Method I in Proposed Regenerative CHB Drive with Regular SPWM.

e) Proposed Carrier Shifting Method II for Sideband Harmonics Elimination

The harmonic spectrum for the primary current when using proposed method II with multi-winding transformer is shown in Fig. 4.25 As discussed, the first sideband harmonics to emerge are of carrier index equal to 3 with magnitudes less than the standards limits (<0.3%). There is no third order harmonics. THD is improved to 0.61%.

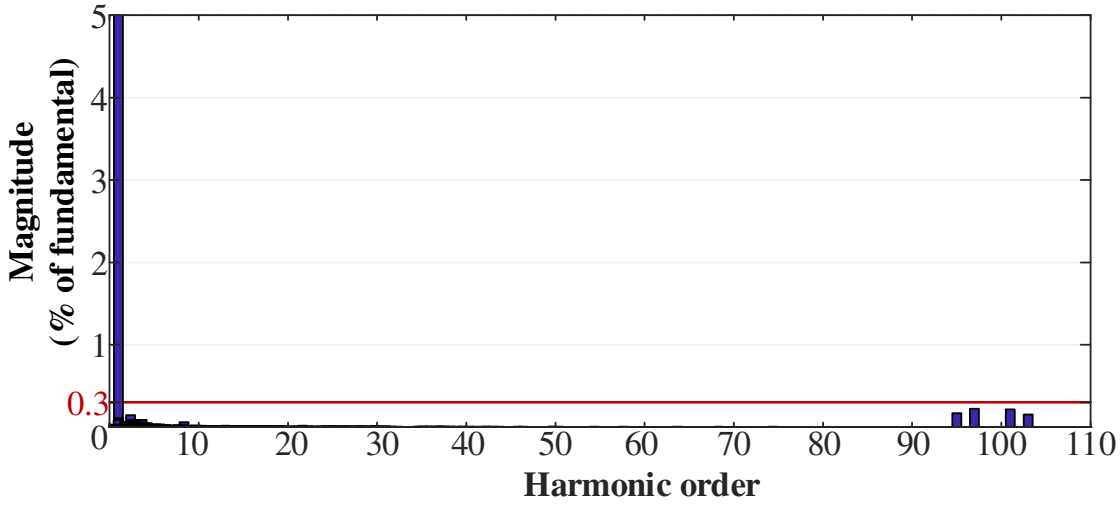

Fig. 4.25. Primary Currents Harmonics using Carrier Shifting Proposed Method II in Proposed Regenerative CHB Drive with Regular SPWM.

4.7.4 Third Order Harmonic Injection SPWM Modulation

Fig. 4.26 shows overall system performance using SPWM with 15% third order harmonic injection modulation. The motor was operated in both rated motoring and regeneration conditions using FOC scheme. Input reactive power is zero indicating unity power factor. Input cell current low order harmonics (3^{rd}, 5^{th}, and 7^{th}) are evident at light loading operation. DC-link voltage is controlled during the whole operation at the reference value of 1300V, while the two capacitor's voltages are kept at 650V.

a) DC-Link Capacitors Ripples

Fig. 4.27 and 4.28 show the DC-link capacitors' and the total DC-link voltage ripples in case of SPWM with 3^{rd} order harmonic injection during rated motoring and regeneration. Fig. 4.29 shows their harmonic spectra. As discussed, 2^{nd} and 4^{th} order harmonics appear in addition to the regular SPWM harmonics. DC-link ripples magnitude is around 1.5%.

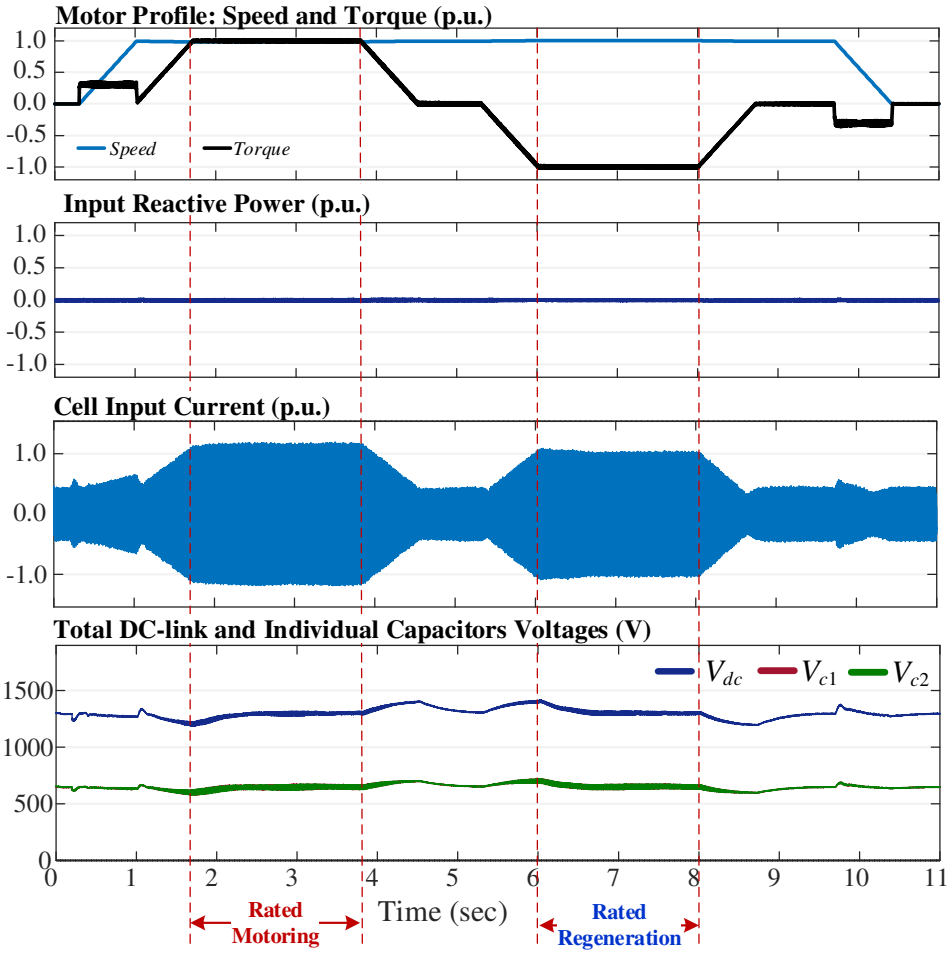

Fig. 4.26. Motor Profile, Input Reactive Power, Cell Input Current, Total DC-Link and Individual Capacitors' Voltages in Proposed Regenerative CHB Drive with 3rd Order Harmonic Injection.

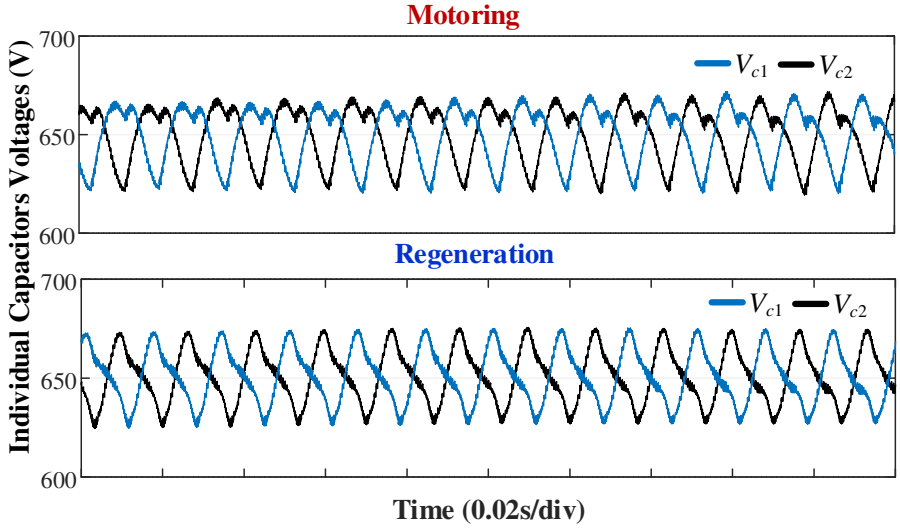

Fig. 4.27. Capacitor Voltages during Motoring and Regeneration in Proposed Regenerative CHB Drive with 3rd Order Harmonic Injection.

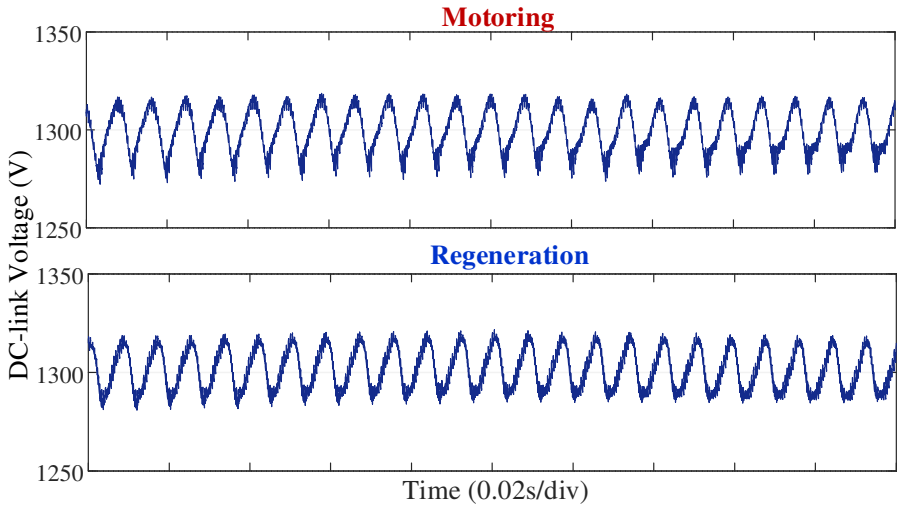

Fig. 4.28. DC-Link Voltage during Motoring and Regeneration
in Proposed Regenerative CHB Drive with 3rd Order Harmonic Injection.

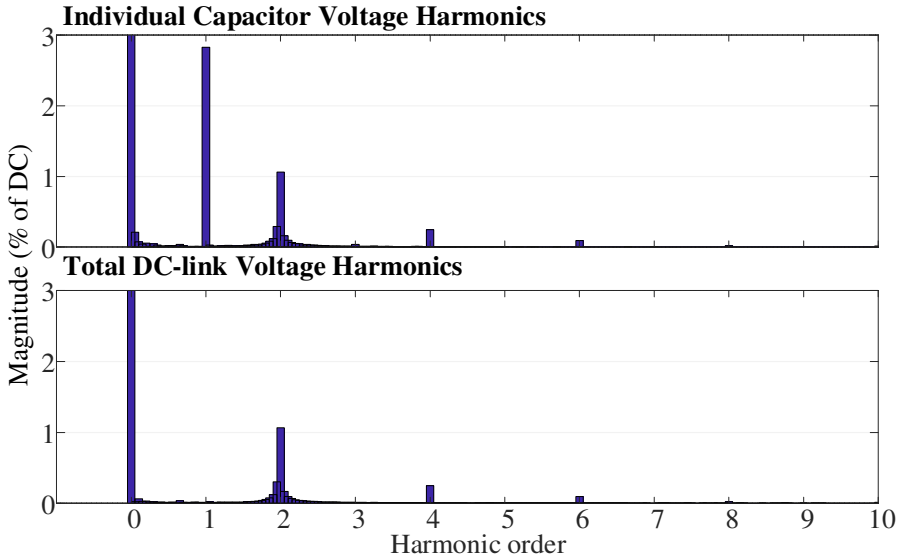

Fig. 4.29. Capacitors and DC-Link voltages Harmonics
in Proposed Regenerative CHB Drive with 3rd Order Harmonic Injection.

b) Secondary and Primary Currents Harmonic analysis

Fig. 4.30 shows the waveforms and one harmonic spectrum of rated secondary currents when using 3rd order harmonic injection of 15%. In addition to high switching harmonics, the currents contain 3rd, 5th, and 7th harmonics that exceed the standards limit. As discussed, phase-shifting transformer must be used in the interface connection.

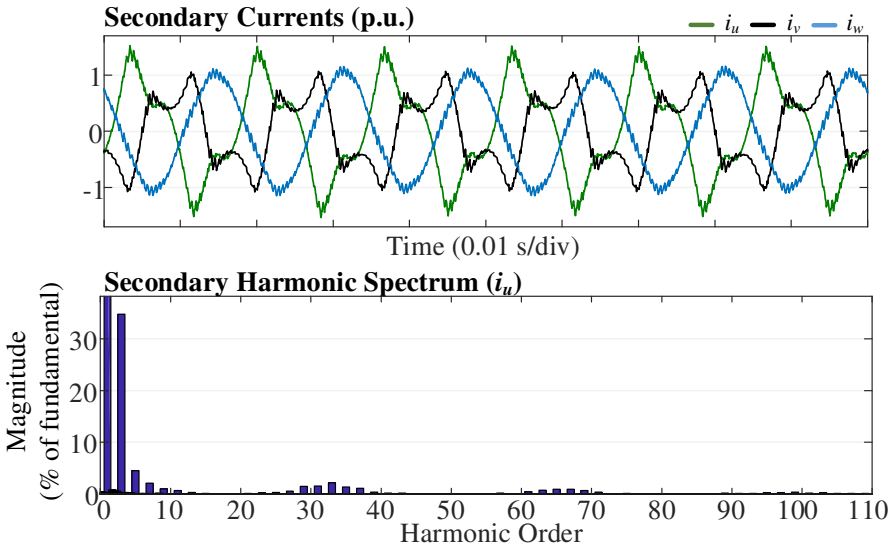

Fig. 4.30. Secondary Currents Waveforms and Harmonic Spectrum in Proposed Regenerative CHB Drive with 3rd Order Harmonic Injection.

Fig. 4.31 shows the waveforms and one harmonic spectrum of the primary currents with phase-shifting transformer. The 5th harmonics are highly reduced due to the cancellation of the second term in (4.54). The seventh harmonics are completely cancelled. However, third order harmonics are still reflected as indicated in the theoretical analysis.

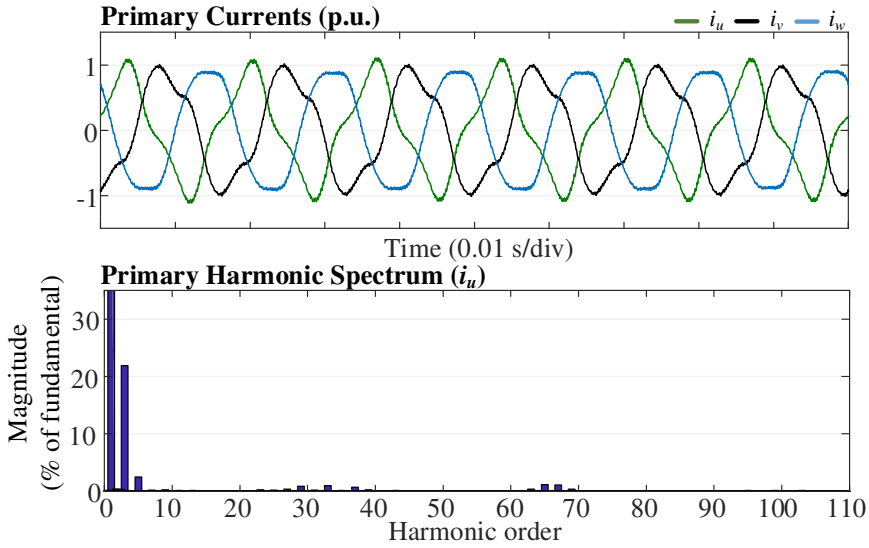

Fig. 4.31. Secondary Currents Waveforms and Harmonic Spectrum in Proposed Regenerative CHB Drive with 3rd Order Harmonic Injection and Phase-Shifting Transformer.

c) Proposed Phase Alternation for Third Order Harmonics and Carrier Harmonics Elimination from the Primary Currents

Fig. 4.32 shows the primary current waveforms and harmonics with application of the phase alternation method on using SPWM with 3rd order harmonic injection of 15%. The proposed method highly improves the primary harmonics. The currents are now balanced. Third order harmonics are eliminated. Additional third, fifth, and seventh harmonics are highly reduced (< 0.5%) using phase-shifting transformer and proposed arrangement. Carrier harmonics are cancelled. The only harmonics exceeding the standard limits are the sideband harmonics (>0.3%).

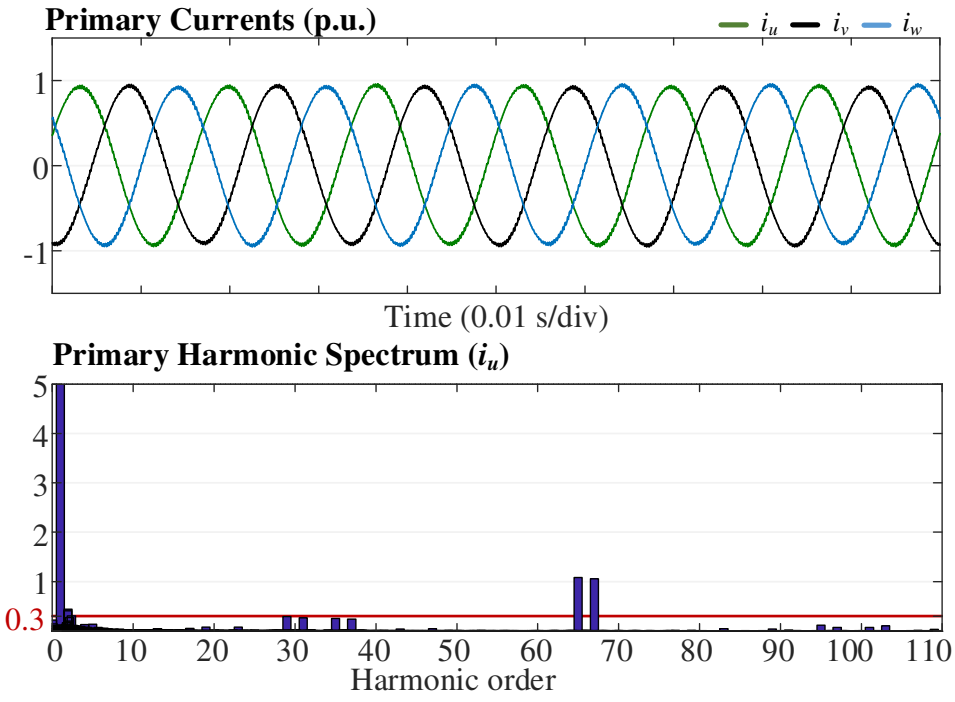

Fig. 4.32. Primary Currents Waveforms and Harmonics using Proposed Phase Alternation Method with Phase-Shifting Transformer in Proposed Regenerative CHB Drive with 3rd Order Harmonic Injection.

d) Proposed Carrier Shifting Method I for Sideband Harmonics Elimination

Fig. 4.33 shows the primary harmonics when proposed carrier shifting method I is used with 3rd order harmonic injection technique for phase-shifting transformer interface. The harmonic groups where m_c is not a multiple of three are cancelled as expected. The third order harmonics are not cancelled due to the violation of phase-alternation in this connection as discussed. Fifth harmonics are reduced and seventh harmonics are cancelled due to the use of phase-shifting transformer.

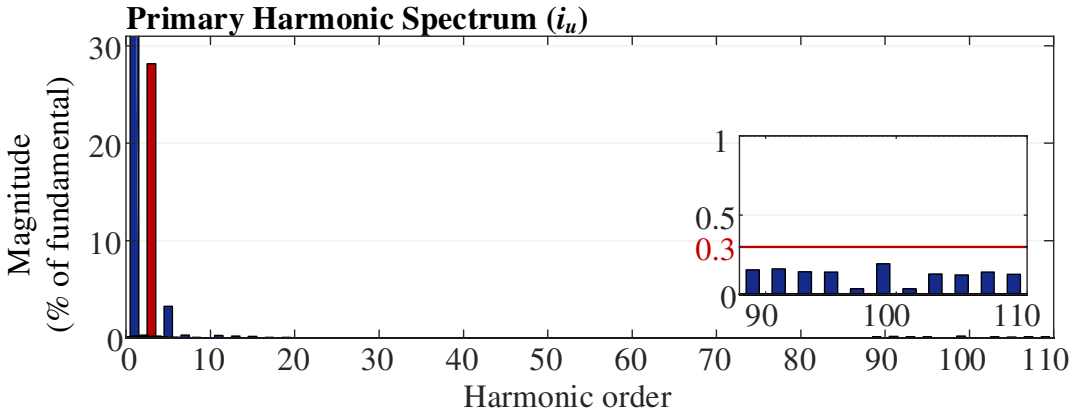

Fig. 4.33. Primary Currents Harmonics using Carrier Shifting Proposed Method I in Proposed Regenerative CHB Drive with 3rd Order Harmonic Injection.

e) Proposed Carrier Shifting Method II for Sideband Harmonics Elimination

Proposed method II harmonic performance is shown in Fig. 4.34. Third order harmonics are cancelled as well as the harmonic groups where m_c is not divisible by 3. However, fifth and seventh harmonics are not cancelled due to the use of multi-winding transformer where all the secondary winding sets have the same phase-shift. As expected, the proposed carrier shifting techniques will violate the cancellation of third, fifth, and seventh harmonics. The research on another carrier-shifting method is a good topic for future work.

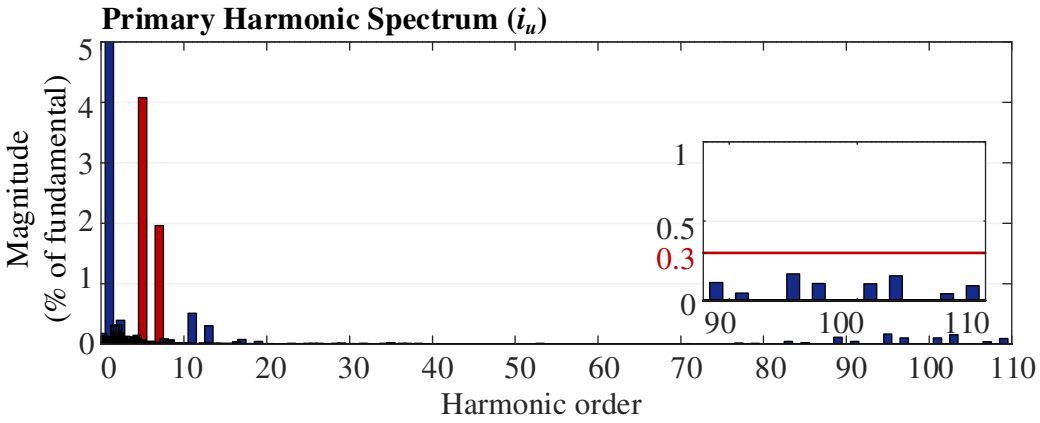

Fig. 4.34. Primary Currents Harmonics using Carrier Shifting Proposed Method II in Proposed Regenerative CHB Drive with 3rd Order Harmonic Injection

4.7.5 General Conclusion

From the previous analysis, it is clear that using regular SPWM with the proposed FSTPI-AFE based power cells is more suitable for better overall harmonic performance.

4.8 Summary

A new configuration for regenerative CHB power cell with reduced switch-count is proposed. The cell uses an FSTPI as an AFE instead of the 2L-VSI, thus it reduces the number of required switches per cell by two switches, which reduces system cost, size, and complexity. The cell is studied thoroughly, and analysis is verified using simulation studies with an FOC-controlled motor load in both motoring and regeneration modes.

As a three-phase AFE configuration, the proposed configuration eliminates the low order harmonics cancellation limit that exists in the single phase AFEs. Moreover, AFE modulation is simple through using SPWM by changing the phase modulating signals into line-to-line modulating signals.

To address the challenges of FSTPI AFE operation, two solutions are proposed. First, a phase alternation connection is proposed to eliminate unbalance, triplen harmonics, and carrier harmonics from the primary current. The use of phase alternation method allows third order harmonic injection.

Moreover, to comply with the grid connection standards, two proposed methods based on carrier phase shifting are used to cancel the sideband harmonics for regular SPWM. More investigation to cancel the sideband harmonics in case of third order harmonic injection is an interesting topic for future research.

The analysis and simulation studies show that regular SPWM technique with no third order harmonic injection seems to have the best performance with this configuration.

Table 4.5 shows the comparison between the proposed configuration using SPWM and the existing regenerative CHB power cells. The benchmark is the 2L-VSI AFE modulated with SPWM with third order harmonic injection. Compared with other existing reduced switch-count cells, the proposed configuration offers simple control structure, low order harmonics cancellation for any number of cells, and no input ripples on the DC-link voltage. However, higher current rating is always the price to be paid in all reduced switch-count solutions.

TABLE 4.5. COMPARISON BETWEEN PROPOSED REGENERATIVE CHB POWER CELL WITH THE EXISTING REGENERATIVE CHB POWER CELLS.

Cell Configuration	2L-VSI with 3rd order harmonic injection	FSTPI-AFE Cell	H-H Cell	Semi-Reduced Cell	Reduced Cell
Number cell switches	10	8	8	6	4
Output voltage levels for n cells/phase	$2n+1$	$2n+1$	$2n+1$		$n+1$
AFE interface	Three-phase	Three-Phase	Single-phase		
AFE control reference frame	Rotating d-q frame	Rotating d-q frame	Stationary abc-frame (more complex)		
Low order harmonic elimination from input current	Effective for any number of cells/phase	Effective for any number of cells/phase	Effective only if number of cells/phase is multiple of three		
Low Order DC-link ripples	Output 2nd order ripples	Output 2nd order ripples	Output and input 2nd order ripples		
Capacitors ripples	Output 2nd order	Output 2nd order ripples	Output and input 2nd order		
		Input Fundamental		Input Fundamental	
			Output fundamental		
AFE Switches current rating	I_{in}	$2\,I_{in}$	$1.73\,I_{in}$	$3.46\,I_{in}$	$1.73\,I_{in}$
Switches voltage rating	V_{dc}	V_{dc}	V_{dc}		$2\,V_{dc}$

Chapter 5

Proposed New Control Strategy for Fundamental Frequency End (FFE) Converters

5.1 Introduction

As mentioned in Chapter 2, the addition of AFEs to allow regeneration in CHB motor drives adds more complexity, losses, and cumbersomeness, which can hinder the economic viability of regenerative motor drives. One way to overcome this hindrance is the reduction of the AFE switch-count as discussed in Chapters 3 and 4.

In this thesis work, a second solution is proposed which is to lower the front-end switching frequency by employing fundamental frequency ends (FFEs) where the switches are triggered at fundamental frequency. This approach can lower the switching power losses, and lead to more compact heat sink design. In this chapter, the review of existing AFEs and FFEs modulations and controllers is first discussed to establish the necessary background. A new proposed FFE controller is then presented. The controller is based on the active and reactive power flow dependencies on power angle and voltage magnitude variations respectively. The performance of the proposed controller was first verified through simulation studies on a grid-connected 2L-VSI FFE. It provides high DC-link voltage utilization, active and reactive power control, and inherent current protection. Application of FFEs in regenerative CHB drives using the proposed controller is discussed in the following chapter.

5.2 AFE Converters Modulation and Control

5.2.1 Modulation

Active front ends is the common name for controlled rectifiers that are modulated by sinusoidal PWM (SPWM) [2], space vector PWM (SV-PWM) [2], or selective harmonic elimination (SHE) modulation techniques [36]. The following is a brief description for each of these techniques.

a) SPWM

SPWM is a carrier-based modulation [2]. For each leg, a modulating signal of the desired fundamental frequency and phase-shift is compared with a triangular carrier of high frequency as shown in Fig. 5.1.

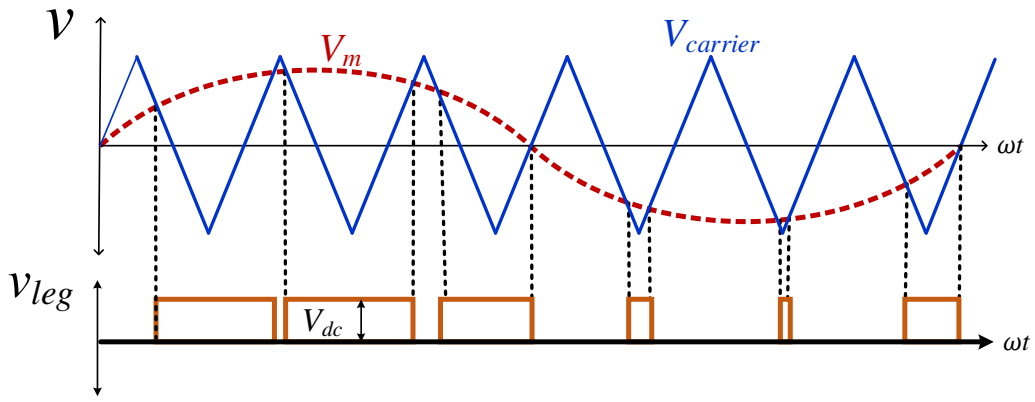

Fig. 5.1. SPWM Technique in One Converter Leg [2].

The comparison result is different-width pulses to synthesize the modulating signal. The fundamental component amplitude is given by the amplitude modulation index (m_a) expressed by:

$$m_a = \frac{|V_m|}{|V_{cr}|} \tag{5.1}$$

, where $|V_m|$ is the modulation signal amplitude, and $|V_{cr}|$ is the carrier signal amplitude.

The harmonic content of SPWM output is centered around the carrier frequency and its multiples. The ratio between the carrier signal frequency and the modulation signal frequency is given by the frequency modulation index (m_f) in:

$$m_f = \frac{f_{cr}}{f_m} \tag{5.2}$$

In case of SPWM application in 2L-VSI, the harmonic orders lower than $(m_f - 2)$ are eliminated [2]. The DC-link voltage utilization in SPWM is 61.2% for output line-to-line voltage. However, third order harmonic injection can increase this utilization to 70.7% [2].

b) SV-PWM

For the 2L-VSI AFE shown in Fig. 5.2, each leg has two switching states [2]: [P] when the upper switch is conducting, and [O] when the lower switch is conducting as shown in Table 5.1. This results in a total of eight switching states combinations for the 2L-VSI [2].

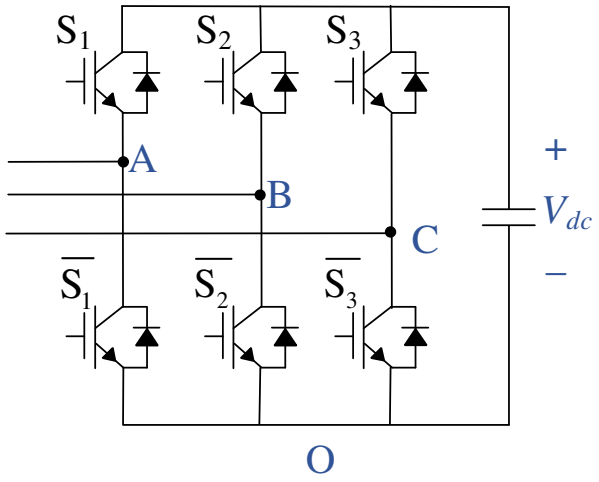

Fig. 5.2. Two-level Voltage Source Inverter AFE.

TABLE 5.1. 2L-VSI SWITCHING STATES.

Switching State	Leg A		Leg B		Leg C	
	S_1	v_{AO}	S_2	v_{BO}	S_3	v_{CO}
[P]	1	V_{dc}	1	V_{dc}	1	V_{dc}
[O]	0	0	0	0	0	0

SV-PWM depends on the concept of space vector representation in the $\alpha-\beta$ reference frame for the three-phase system [2]. The space vector voltage for each switching state can be calculated by:

$$\vec{v}(t)=\frac{2}{3}\left[v_{AO}(t)*e^{j0}+v_{BO}(t)*e^{j\frac{2\pi}{3}}+v_{CO}(t)*e^{-j\frac{2\pi}{3}}\right] \tag{5.3}$$

, where v_{AO}, v_{BO}, and v_{CO} are the output phase voltages in terms of DC-link voltage.

Fig. 5.3(a) shows the resulting eight voltage vectors from the corresponding switching states. Two of these vectors ($\vec{V}_0$ and $\vec{V}_7$) have zero magnitude and are called "zero voltage vectors" or $\vec{V}_z$. The remaining active six vectors divide the space into six sectors.

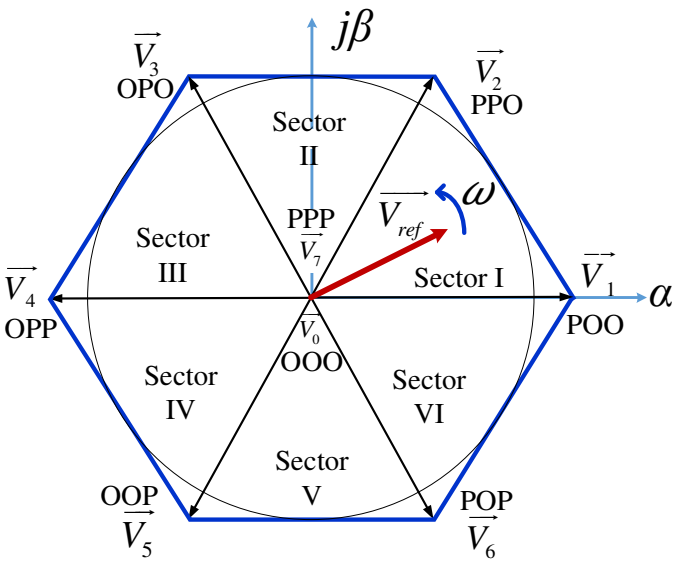

(a) Switching Vectors.

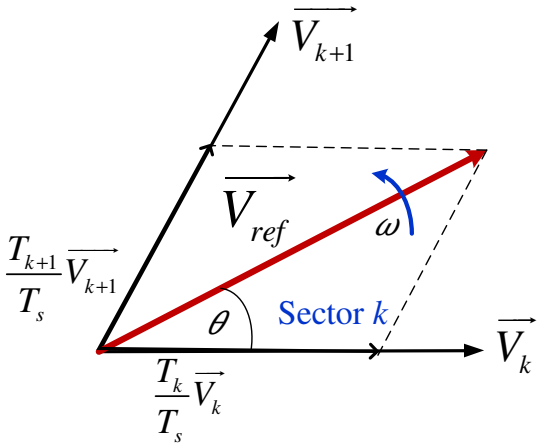

(b) Synthesis of Reference Voltage Using Voltage Vectors.

Fig. 5.3. Space Vector Pulse Width Modulation [2].

For any given reference set of three balanced voltages, it can be represented by a reference space vector which is rotating in the $\alpha-\beta$ frame by the desired angular frequency (ω). The rotating reference vector can by synthesized by boundary vectors of the sector in which it is located and the two zero vectors as shown in Fig. 5.3(b). The switching time for each vector is calculated for each instant using the instantaneous voltage balancing concept in (5.4) and trigonometric analysis of Fig. 5.3(b) [2].

$$\overrightarrow{V_{ref}} * T_s = \overrightarrow{V_k} * T_k + \overrightarrow{V_{k+1}} * T_{k+1} + \overrightarrow{V_z} * T_z \tag{5.4}$$

, where T_s is the sampling time, T_k, T_{k+1}, and T_z are the switching times for each vector.

To have output voltage with low distortion, the sampling time should be small. The harmonic content of SV-PWM output voltages contains low order harmonics with small magnitudes in addition to the switching harmonics [2]. The DC-link utilization for line to line voltage is 70.7%, which is equal to the SPWM with third order harmonic injection DC-link utilization [2].

c) SHE

SHE is a special type of PWM where undesired harmonics, usually low order harmonics, are eliminated by introducing of switching at certain angles [36]. As the output voltage is always quarter-wave symmetric, it is enough to calculate the firing angles in the first quarter cycle. For the 2L-VSI shown in Fig. 5.2, the output voltage for phase *x* using SHE is shown in Fig. 5.4.

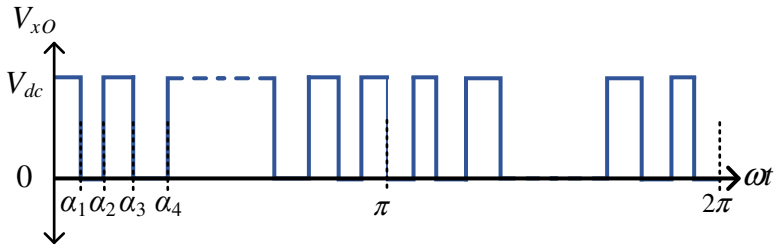

Fig. 5.4. Output Waveform using Selective Harmonic Elimination [36].

Using Fourier analysis, the magnitude of each harmonic component of order (n) is:

$$V_n = \frac{2V_{dc}}{n\pi}\left[1+2\sum_{k=1}^{N}(-1)^k \cos n\alpha_k\right] \tag{5.5}$$

, where N is the number of firing angles in each quarter cycle (4 in this example), and k is the firing angle order.

Based on (5.5), to control the fundamental frequency and eliminate M harmonics, $M+1$ non-linear equations are needed to be solved. These equations are solved numerically offline and the angles are then stored for generating the switching sequence during operation [36].

5.2.2 AFE Control

The control of AFEs was discussed earlier in Chapter 3 [13]. A DC-voltage controller is used to regulate the DC-link voltage while a current control loop is used to control the active and reactive power flow. These two control loops offer DC-link voltage stability and non-vulnerability to grid disturbances such as voltage sags. Moreover, the current control loop adds an inherent overcurrent protection.

5.3 Effect of Switching Frequency on Switches Power Losses

In an IGBT module, both the IGBT switch and the free-wheeling diode (FWD) contribute to the total power losses. In [37], the average power losses of the IGBT switch and diode are given by:

$$P_{loss-IGBT} = u_{CE0} \cdot I_{cav} + r_c \cdot I_{crms}^2 + (E_{onT} + E_{offT}) \cdot f_{sw} \tag{5.6}$$

$$P_{loss-Diode} = u_{D0} \cdot I_{Dav} + r_D \cdot I_{Drms}^2 + E_{onD} \cdot f_{sw} \tag{5.7}$$

, where I_{cav} and I_{Dav} are the IGBT and diode average currents. I_{crms} and I_{Drms} are the r.m.s. values of the IGBT and diode currents. u_{ce0} and u_{D0} are the IGBT zero-current collecter-emitter voltage and the diode threshold voltage. r_c and r_d are the IGBT collector-emitter on-resistance and the diode on- resistance. E_{onT} and E_{offT} are the IGBT turn-on and turn-off energies while E_{onD} is the diode turn-on energy. f_{sw} is the switching frequency.

The first two terms in (5.6) and (5.7) represent the conduction losses, they can be considered constant as long as the current does not change. The switching losses are represented by the last terms and are directly proportional to the switching frequency.

One of the main drawbacks of AFEs is their high switching frequency. This results in high power losses, more complexity, and higher cost of the cooling and heat sink design.

5.4 FFE Converters Modulation and Control Prior Art

To overcome high switching power losses, fundamental frequency ends (FFEs) were introduced in 2L-VSI based regenerative low voltage drives. In FFEs, the power switches are triggered only once per cycle. Hence, the switching losses are almost eliminated.

In literature, the following different approaches and control schemes [38]-[44] were presented to implement 2L-VSI FFE.

5.4.1 Natural Triggering of Power Switches

In [38] and [39], 2L-VSI switches are triggered at their natural triggering instants, i.e. based on the intersection points between the supply line voltages, to mimic diode operation during regeneration. For the 2L-VSI FFE shown in Fig. 5.5, each switch is turned on for 120^o as shown in Fig. 5.6. The firing angle can be after the point of intersection (delayed firing) or before it (advanced firing) [39]. During the power flow into the DC-link (motoring operation), the diodes will carry the load current and the switches are deactivated. Conversely, when the power flow is from the DC-link to the grid (regeneration operation), the diodes are reverse-biased and only one path through the switches is available. The maximum DC-link voltage utilization for 2L-VSI line-to-line voltage is 68%.

The implementation of this controller is shown in Fig. 5.7. Since the triggering instants depend on the input voltage angle, a PLL block is required. The angle estimation in PLL can be achieved either using voltage measurements, or the current measurements used for overcurrent protection [38]. The estimated grid angle is then fed to a modulator which generates the gating pulses based on the natural triggering instants.

Although this method is simple, it has two main disadvantages. The reactive power required is high during no load or weak loading. In addition, the DC-link voltage is not controlled, this results in vulnerability to the grid voltage sags and loss of the stored energy in case of grid disturbances [40].

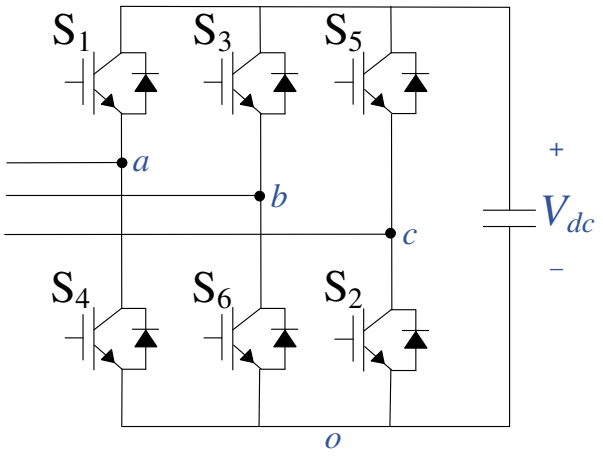

Fig. 5.5. Two-Level Voltage Source Inverter FFE.

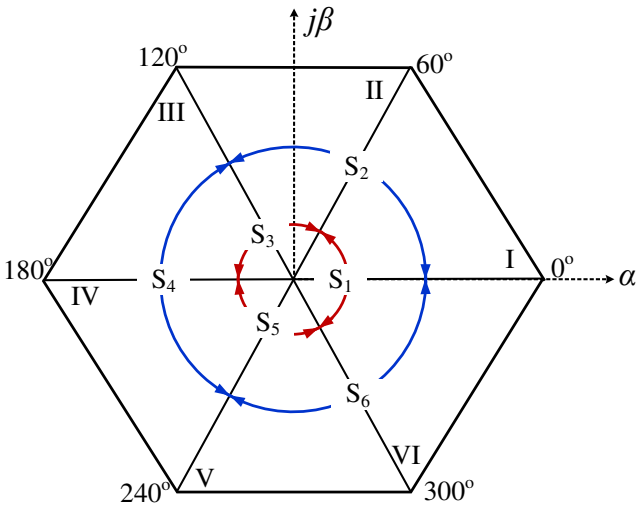

Fig. 5.6. Natural Triggering for 2L-VSI FFE [38].

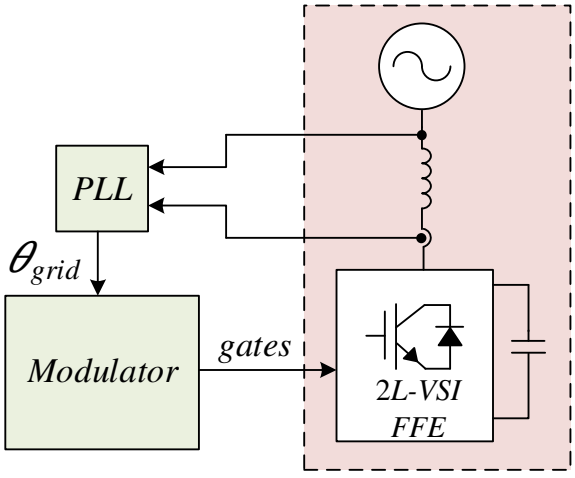

Fig. 5.7. FFE Natural Triggering Controller [38].

5.4.2 Natural triggering with addition of DC-Link Voltage Regulation

In order to provide a stable operation, several modifications were introduced to improve the natural triggering performance and add some degree of DC-link voltage regulation. One simple approach is to allow regeneration based on DC-link voltage predetermined maximum and minimum limits. If the voltage exceeds the maximum limit, the switches are turned on following the natural triggering scheme and the power flows from the DC-link to the grid. When the DC-link voltage falls below the minimum limit, the switches are turned off, and the power is allowed only to flow into the DC-link to charge it. To achieve an efficient result of this method, the two threshold limits must be far from each other, which results in high voltage fluctuations on the DC-link. One way to solve this is by using either a large commutation inductance or a large DC-link capacitance. However, both approaches will increase the cost of the system [40].

In [41], the converter is switched from uncontrolled natural triggering to controlled PWM switching in case of any grid disturbance, high reactive current, or DC-link voltage decline. The transition between the two modes should be achieved without interruption.

An FFE temporary DC-link voltage boost mode was presented in [42]. In this method, the 2L-VSI is operated as follows: one leg is operated through fundamental frequency switching, one leg is switched with high frequency (of 4 kHz), while the last leg is completely switched ON in case of regeneration or OFF in case of motoring.

In [40], a switching sector reduction method is proposed to control the feedback power to have a smoother regulation in the DC-link voltage. In this method, the switching sector is controlled based on a predetermined profile for the DC-link voltage. As a result,

instead of natural triggering, the switches are turned on later and turned off sooner than the normal switching as shown in Fig. 5.8. The two controlling angles φ_1 and φ_2 are determined based on the DC-link voltage profile. The same switching sector reduction method is used in [43] to reduce reactive power in case of no load or light loading.

The switching sector reduction FFE controller is shown in Fig. 5.9. The DC-link voltage (V_{dc}) is measured and compared with the desired DC-link voltage value ($V_{dc\text{-}ref}$). The difference is fed to a DC-link voltage controller (e.g. PI controller), which sets the required firing angles to regulate the DC-link voltage. However, this method reduces the DC-link voltage utilization to be below 68%.

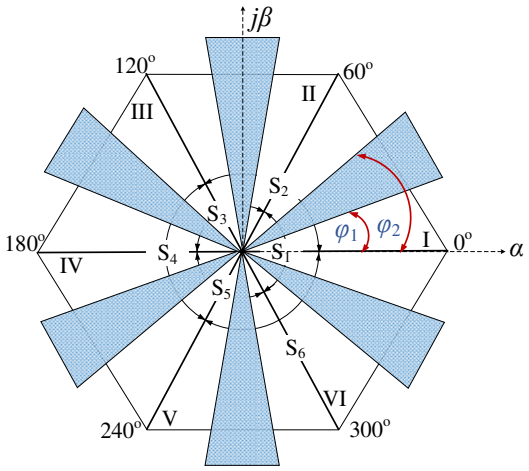

Fig. 5.8. FFE Switching Sector Reduction [40], [43].

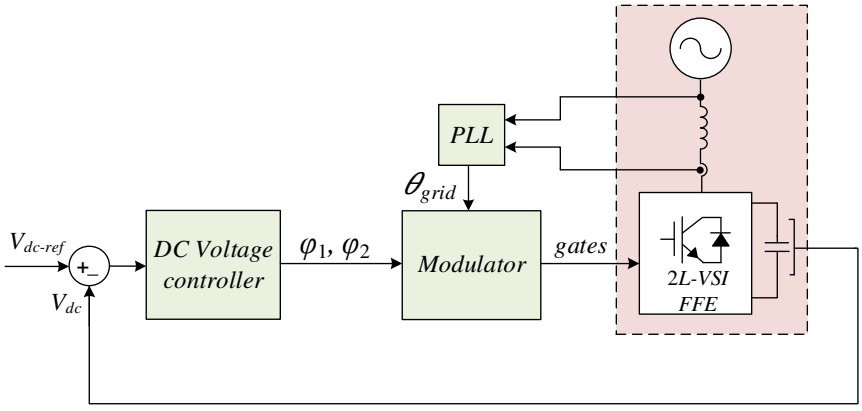

Fig. 5.9. Switching Sector Reduction Controller [40].

5.4.3 Voltage Angle Control

Voltage angle control method is presented in [44] to regulate the DC-link voltage. It consists of a DC-link voltage regulator and a voltage angle controller as shown in Fig. 5.10.

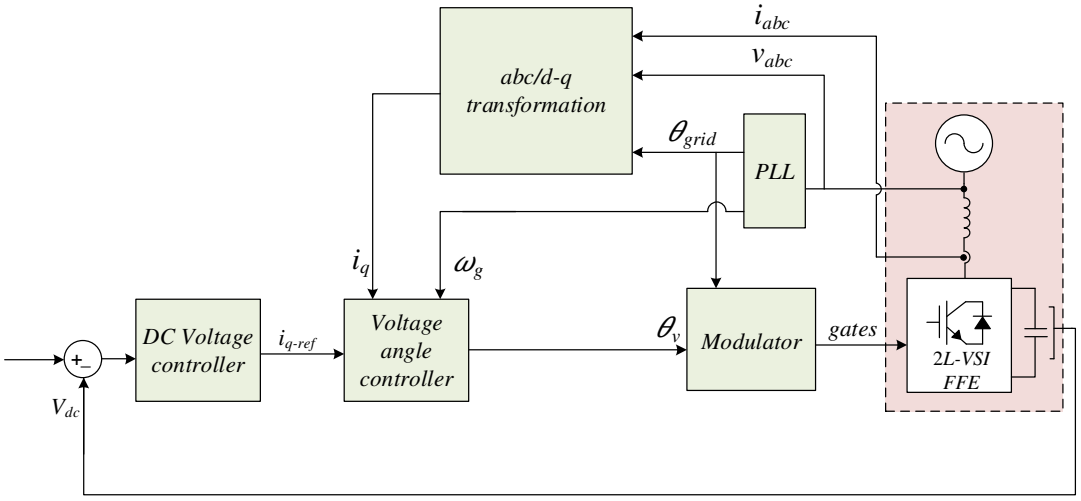

Fig. 5.10. FFE Voltage Angle Control Structure [44].

A PLL is needed to provide the grid angle and frequency used in control and *d-q* transformation. Based on the comparison between the reference and measured values of the DC-link voltage, the regulator sets the required *q*-axis current reference value. The *q*-axis current is then fed to the controller, which compares it with the current measurement from the grid. The error is fed to PI controller which generates a control signal (*M*) as a transfer function of the proportional-integral input. A canceling function then uses the control signal (*M*) to generate the required output voltage angle (θ_v) as a function of *M*, the grid frequency (ω_g), the grid voltage (v_g), the commanded output voltage magnitude ($|v_s|$), and the lumped resistance (R_s) and filter inductance (L_s) between the converter and the grid [44]. The aim of using this angular canceling function is to cancel the angular control part from the grid dynamic response and control the grid as a second-order quadrant axis current. The

angular canceling function is expressed by [44]:

$$\theta_v = \sin^{-1}\left(\frac{M + \frac{R_s}{L_s} v_g}{|v_s|\sqrt{\left(\frac{R_s}{L_s}\right)^2 + \omega_g{}^2}}\right) + \sin^{-1}\left(\frac{\omega_g}{\sqrt{\left(\frac{R_s}{L_s}\right)^2 + \omega_g{}^2}}\right) \tag{5.8}$$

The resulting angle is then added to the grid angle and fed to a modulator which generates the gating signals to the converter. The converter is switched to operate in six-step mode. As a result, the DC-link voltage utilization for line-to-line voltage is 78%.

From (5.8), one of the drawbacks of this controller is the dependence on the system parameters. Another drawback is that there is no reactive power compensation.

5.4.4 Challenges of existing FFE controllers

Review of the existing FFE controllers shows that compromise between DC-link voltage utilization factor, reactive power compensation, and DC-link voltage control is the main challenge in these schemes. In this work, a new approach to implement FFE controller is presented to be convenient for application in the regenerative CHB drives. The proposed controller can control both the active and reactive power flow, and regulates the DC-link voltage while using the highest FFE DC-link utilization factor of 78%.

5.5 Proposed FFE Controller

The proposed controller is mainly based on six-step operation for maximum DC-link utilization, and the power flow equations between two voltage sources in a power system for active and reactive power control [45].

5.5.1 Theoretical Background

Fig. 5.11 shows an FFE-Grid interface with its the corresponding vector diagram.

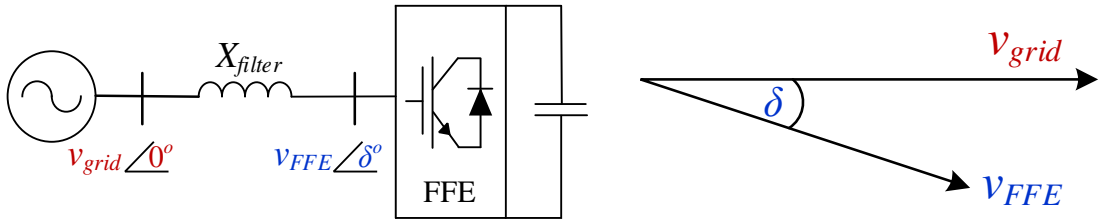

(a) Single-Line Diagram. (b) Vector Diagram.

Fig. 5.11. FFE-Grid Interface.

The per unit active and reactive powers from the grid to the FFE can be expressed by [45]:

$$P = \frac{\left|v_{grid(p.u.)}\right| \cdot \left|v_{FFE(p.u.)}\right|}{X_{filter(p.u.)}} \sin\delta$$
$$Q = \frac{\left|v_{grid(p.u.)}\right| \cdot \left|v_{FFE(p.u.)}\right|}{X_{filter(p.u.)}} \cos\delta - \frac{\left|v_{grid(p.u.)}\right|^2}{X_{filter(p.u.)}} \quad (5.9)$$

, where $\left|v_{grid(p.u.)}\right|$ and $\left|v_{FFE(p.u.)}\right|$ are the per unit magnitudes of the grid and FFE voltages, $X_{filter(p.u.)}$ is the grid connection per unit inductance, and δ is the angle between the grid and FFE voltage vectors (power angle).

The dependencies of active and reactive powers on power angle and FFE voltage can be found by differentiation of (5.9) which yields [45]:

$$\Delta P = \frac{\partial P}{\partial \delta} \cdot \Delta\delta + \frac{\partial P}{\partial v_{FFE}} \cdot \Delta v_{FFE} = \frac{\left|v_{grid(p.u.)}\right| \cdot \left|v_{FFE(p.u.)}\right|}{X_{filter(p.u.)}} \cos\delta \cdot \Delta\delta + \frac{\left|v_{grid(p.u.)}\right|}{X_{filter(p.u.)}} \sin\delta \cdot \Delta v_{FFE}$$
$$\Delta Q = \frac{\partial Q}{\partial \delta} \cdot \Delta\delta + \frac{\partial Q}{\partial v_{FFE}} \cdot \Delta v_{FFE} = \frac{\left|v_{grid(p.u.)}\right| \cdot \left|v_{FFE(p.u.)}\right|}{X_{filter(p.u.)}} \sin\delta \cdot \Delta\delta + \frac{\left|v_{grid(p.u.)}\right|}{X_{filter(p.u.)}} \cos\delta \cdot \Delta v_{FFE} \quad (5.10)$$

Since δ , $\Delta\delta$, and Δv_{FFE} are small , (5.10) approximated to be:

$$\Delta P \approx \frac{\left|v_{grid(p.u.)}\right| \cdot \left|v_{FFE(p.u.)}\right|}{X_{filter(p.u.)}} \cos\delta \cdot \Delta\delta$$
$$\Delta Q \approx \frac{\left|v_{grid(p.u.)}\right|}{X_{filter(p.u.)}} \cos\delta \cdot \Delta v_{FFE} \quad (5.11)$$

(5.11) shows that the change in active power is highly affected by change in the power angle, while reactive power is highly affected by change in the voltage magnitude. Consequently, the power angle can be used to control the active power, while the voltage magnitude can be used to control the reactive power [45].

Tables 5.2 and 5.3 show how the active and reactive power flows are affected by changing the corresponding power angle and voltage magnitude. These relations are used in the proposed controller strategy to control both active and reactive powers between the FFE and the grid.

TABLE 5.2. RELATION BETWEEN POWER ANGLE AND ACTIVE POWER FLOW.

Power Angle (δ)	**Active Power Flow**
$\delta = 0$	No flow
$\delta > 0$	Flow from grid to FFE
$\delta < 0$	Flow from FFE to grid

TABLE 5.3. RELATION BETWEEN VOLTAGE MAGNITUDE AND REACTIVE POWER FLOW.

VOLTAGE MAGNITUDE	**REACTIVE POWER FLOW**
$\left\|v_{grid}\right\| = \left\|v_{FFE}\right\|$	No flow
$\left\|v_{grid}\right\| > \left\|v_{FFE}\right\|$	Flow from grid to FFE
$\left\|v_{grid}\right\| < \left\|v_{FFE}\right\|$	Flow from FFE to grid

5.5.2 Proposed Controller Structure

The proposed controller structure is shown in Fig. 5.12. It comprises DC-link voltage control loop, current control loop, and a modulator.

The system is controlled in *d-q* reference frame, therefore, a PLL is used to obtain the grid angle. The voltage *d*-component (v_d) is aligned with the grid voltage, thus, the voltage *q*-component (v_q) is set to zero. This ensures that the current *d*-component (i_d) is linked to the active power flow, while the current *q*-component (i_q) is linked to the reactive power flow.

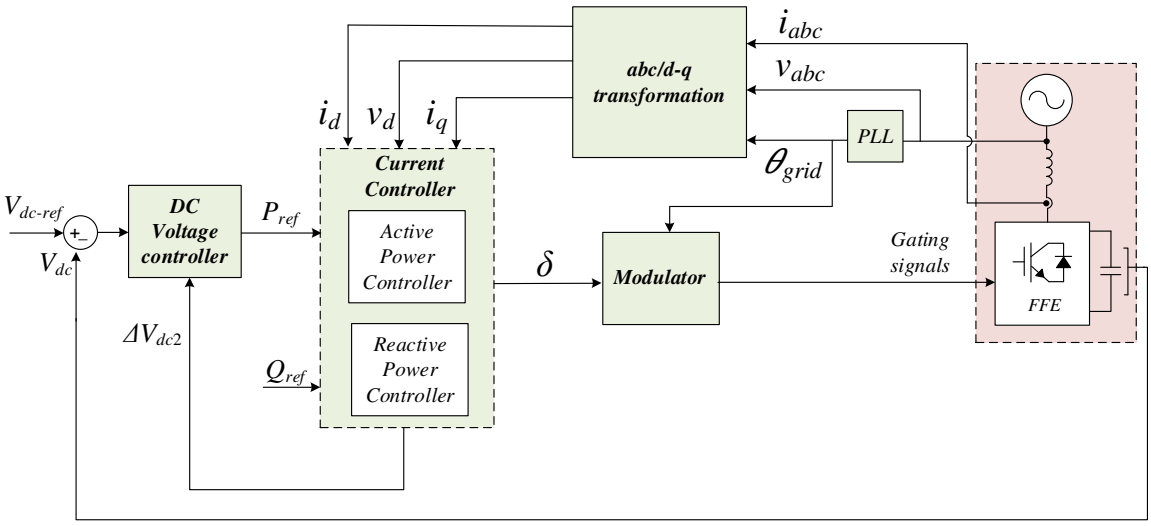

Fig. 5.12. Proposed FFE Controller Structure.

a) DC-link Voltage Controller

The DC-link voltage controller loop is shown in more detail in Fig. 5.13. Unlike in the case of AFE, the DC-link voltage reference is not set to a constant voltage due to the absence of modulation concept, instead a very small change of DC-link voltage around a nominal value is allowed to control the FFE output voltage magnitude and consequently the reactive power flow.

The reference voltage is composed of three parts:

- *Constant voltage part based on the grid voltage ($V_{dc\text{-}nominal}$):*

  Nominal voltage reference to satisfy the equalization of FFE fundamental output voltage to the grid voltage in case of synchronization, so that there is no reactive power flow. The nominal value is based on the DC-link utilization by:

$$V_{dc\text{-}nominal} = \frac{v_{grid}}{m} \tag{5.12}$$

  , where m is the DC-link voltage utilization factor based on the FFE topology.

- *Reactive power compensation feed forward component (ΔV_{dc1}):*

  In case of loading, there will be a voltage drop across the grid filter leading to reactive power consumption. This voltage component depends on the grid filter and current. In per unit calculation, the load power (P_{Load}) can be used as a measure for the loading value instead of the current as shown in (5.13).

$$\Delta V_{dc1} = P_{Load-p.u}.* X_{filter-p.u.} * V_{dc\text{-}nominal} \tag{5.13}$$

- *Reactive power compensation component (ΔV_{dc2}):*

  This voltage component is set by the current controller to ensure the control of reactive power based on current q-component.

These three voltage components are summed to compose the DC-link voltage reference. The DC-link voltage reference is then compared with the measured DC-link voltage, the error is fed to a PI controller that sets the reference active power. For better dynamic response, a feed forward power component based on the load power is added to the PI controller output.

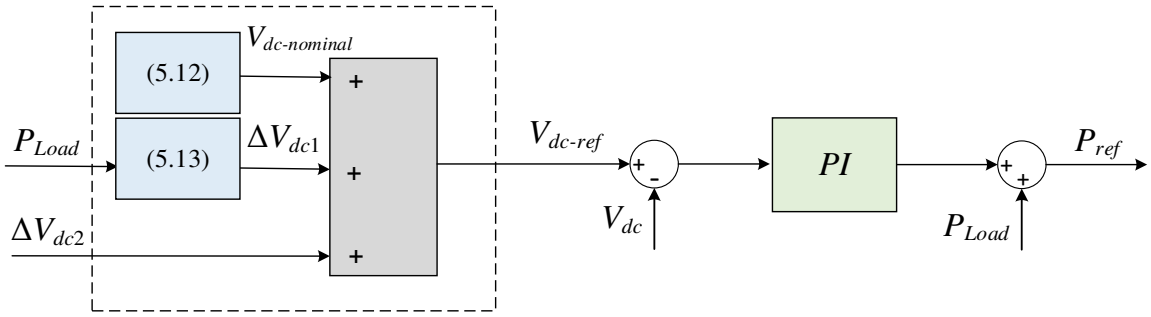

Fig. 5.13. Proposed FFE DC-Link Voltage Controller.

b) Current Controller

Fig. 5.14 shows the details of the current controller. The reference active and reactive power values set the reference current *d* and *q* components respectively using the system power equations in *d-q* reference frame in (2.6). The measured currents are filtered and transformed from *abc* to *d-q* reference frame. The reference and the measured components are compared. The error from the current *d*-component comparison is fed to a PI controller to set the power angle needed for active power flow. The difference between the measured and reference *q*-components is fed to another PI controller to set the third voltage part in the reference DC-link voltage (ΔV_{dc2}) to compensate the reactive power.

c) Modulator

The required power angle is added to the grid angle and is fed to a waveform generator to synthesize three-phase sinusoidal waveforms based on the resulted angle. The sinusoidal waveforms are then compared with zero reference inside the modulator to switch the converter in six-step mode where each switch conducts for 180^{o}.

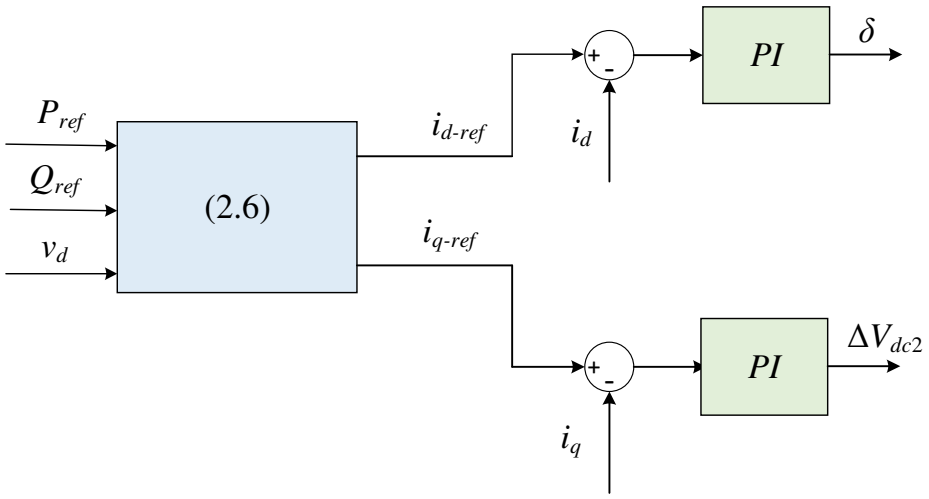

Fig. 5.14. Proposed FFE Current Controller.

5.5.3 Application of the Proposed Controller on Two-Level Voltage Source Inverter

Fig. 5.15 shows the output voltage for arbitrary phase *x*, where *x* is *a*, *b*, or *c*, with the six-step operation of the proposed controller on the 2L-VSI FFE shown in Fig. 5.5.

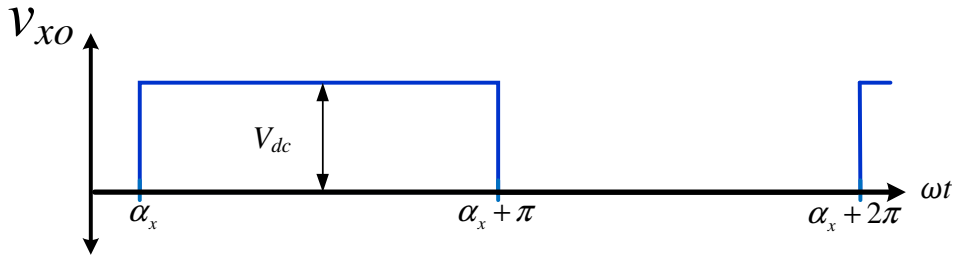

Fig. 5.15. 2L-VSI Phase Output Voltage using Six-Step Operation.

The Fourier series of the output voltage is given by:

$$V_{xo} = \frac{V_{dc}}{2} + \sum_{n=1}^{\infty} \frac{2V_{dc}}{\pi} \sin\left(n\omega_g t + n\alpha_x\right) \tag{5.14}$$

, where ω_g is the grid frequency, α_x is the arbitrary fundamental phase shift, and *n* is the harmonic order.

The line-to-line voltage (V_{ab}) is shown in Fig. 5.16, and expressed by:

$$V_{ab} = \sum_{k=0}^{\infty} \frac{2\sqrt{3}V_{dc}}{\pi} \sin\left((6k \pm 1)\left(\omega_g t + (\alpha_x + \frac{\pi}{6})\right)\right) \tag{5.15}$$

From (5.15), the DC-link voltage utilization factor for fundamental line-to-line voltage (n=1) is 78%. The DC-offset and triplen harmonics are cancelled from the line-to-line voltage.

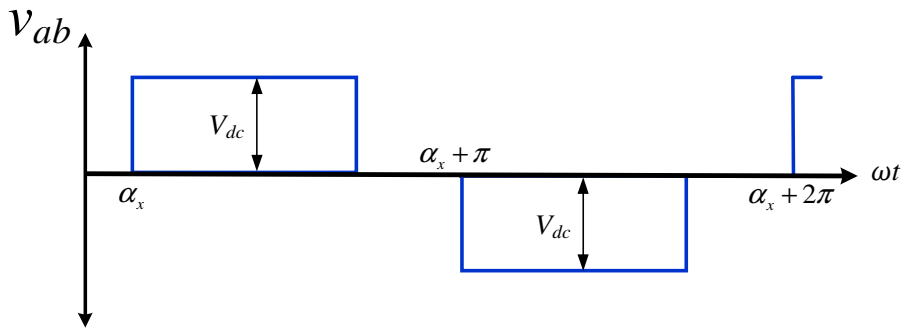

Fig. 5.16. 2L-VSI Line-to-Line Voltage using Six-Step Operation.

5.5.4 Simulation Studies

To verify the theoretical analysis, simulation studies on a grid-connected 2L-VSI FFE using the proposed controller were conducted. A regenerative load is connected to the DC-link. The system parameters are shown in Table 5.4.

TABLE 5.4. 2L-VSI FFE SIMULATION SYSTEM PARAMETERS.

FFE input voltage	480 V
DC-link nominal reference voltage	615 V
DC-link Current	100 A
Nominal frequency	60 Hz
Grid-connecting filter	2 mH
Capacitor value	5000 µF (50 µF/A)

Fig. 5.17 shows the gating sequence for the switches (S_1 and S_4) for the FFE shown in Fig. 5.5, each switch conducts for 180°, and is switched ON/OFF once in each cycle. A detailed view of the line-to-line voltage is shown in Fig. 5.18, as discussed, the waveform contains three voltage levels of $+V_{dc}$, $-V_{dc}$ and 0.

Fig. 5.19 shows the performance of the proposed controller with rated motoring and regenerative active power with unity power factor. The reactive power is compensated and kept around zero. The DC-link voltage is regulated around the nominal value. The line current and voltage have good dynamic response.

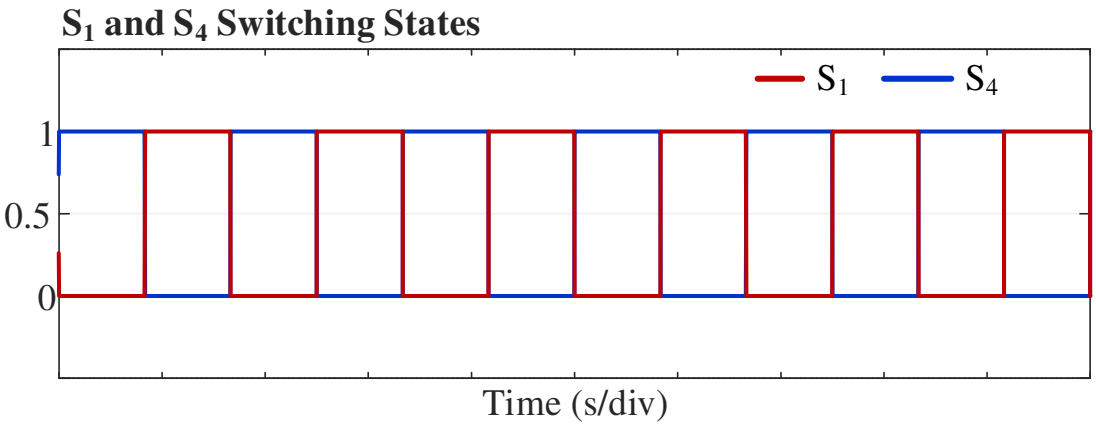

Fig. 5.17. 2L-VSI Switching States using Proposed FFE Controller.

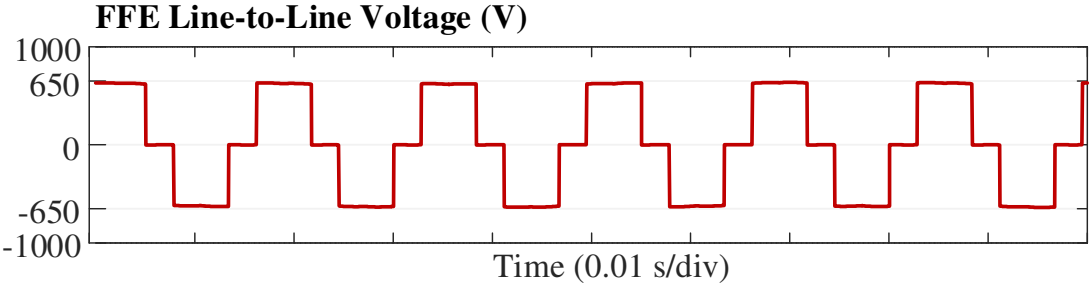

Fig. 5.18. 2L-VSI FFE Output Line-to-Line Voltage using Proposed FFE Controller.

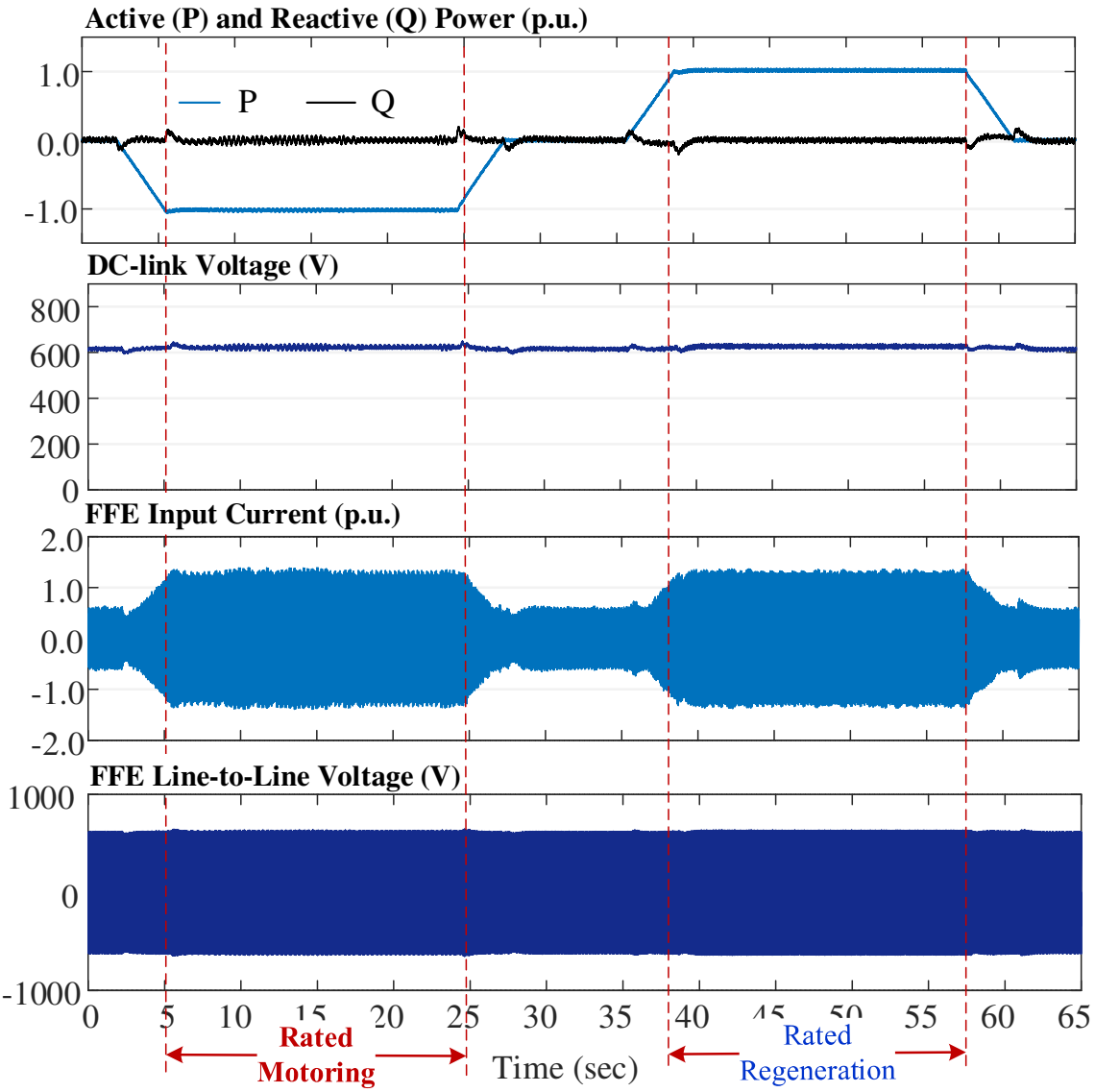

Fig. 5.19. Proposed FFE Controller Performance with Rated Motoring and Regeneration with Zero Reactive Power.

The FFE line currents and their harmonic spectrum are shown in Fig. 5.20 and 5.21. The first low order harmonics to appear are the 5th and 7th order harmonics.

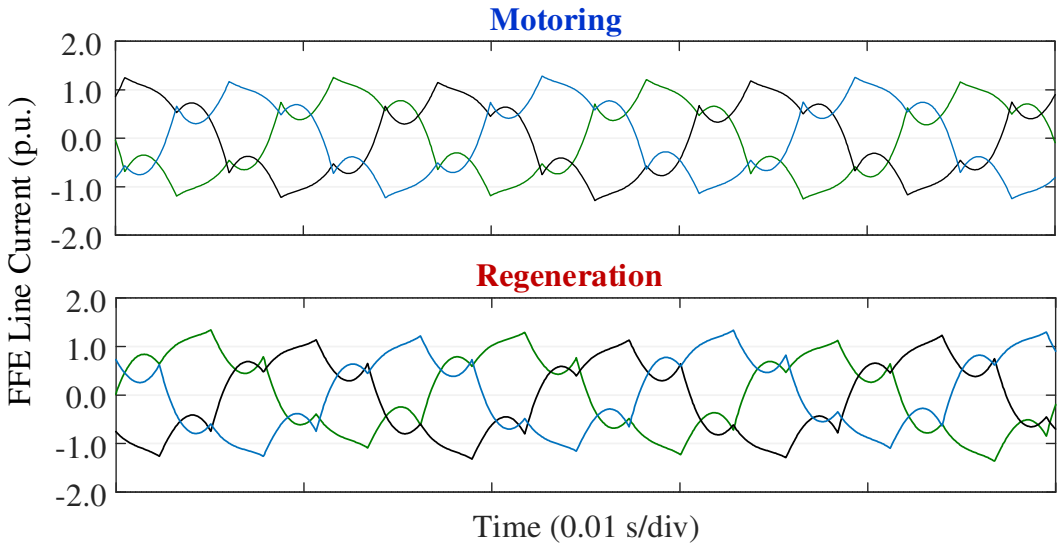

Fig. 5.20. Line Currents of 2L-VSI FFE using Proposed Controller during Rated Motoring and Regeneration.

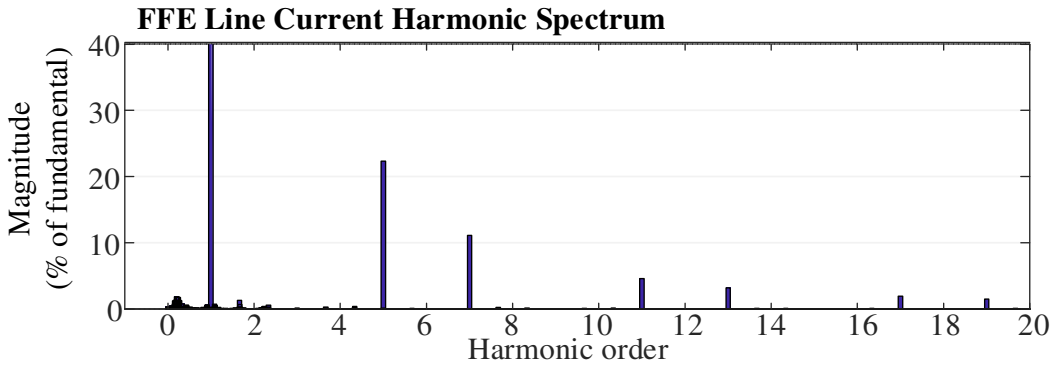

Fig. 5.21. Line Currents Harmonics of 2L-VSI FFE using Proposed Controller during Rated Motoring and Regeneration.

To test the controller capability of controlling any value of reactive power, the system was run as a STATCOM with zero active power and rated reactive power in both directions, inductive and capacitive. The overall performance is shown in Fig. 5.22. As discussed, the DC-link voltage decreases or increases to control the reactive power flow. The system has a good dynamic response.

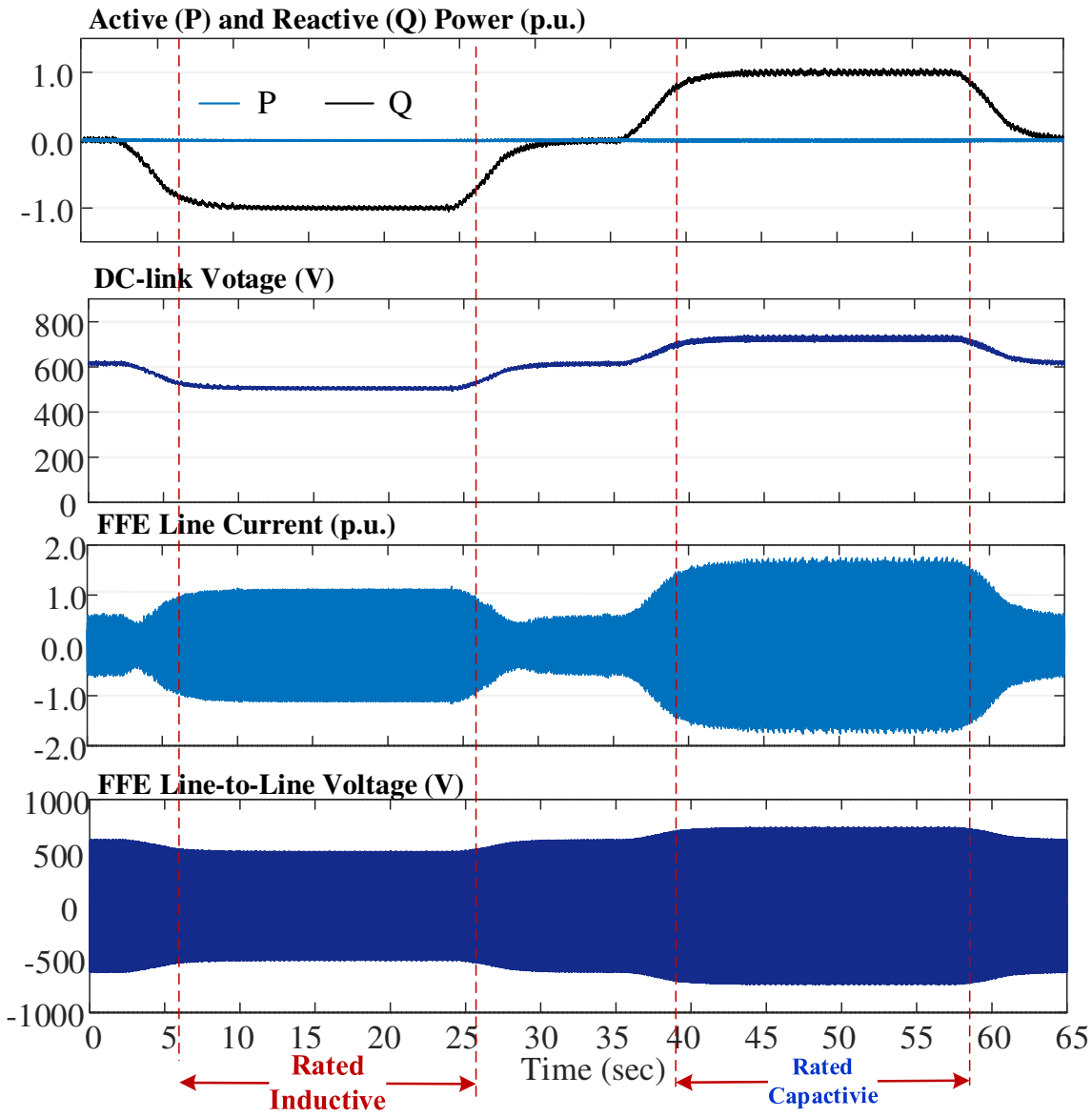

Fig. 5.22. Proposed FFE Controller Performance with Rated Inductive and Capacitive STATCOM operation.

Unlike the unity power factor operation, the current waveforms completely change in the inductive and capacitive operations due to different current paths in the switches and the diodes as shown in Fig. 5.23. Nevertheless, there is not much change in their harmonic spectrum as shown in Fig. 5.24.

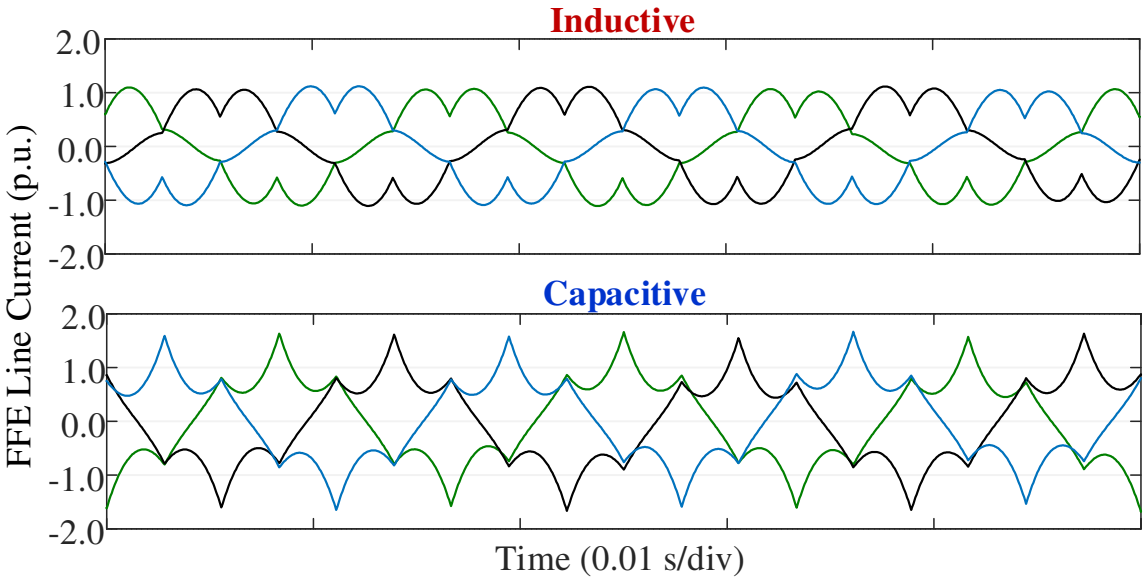

Fig. 5.23. Line Currents of 2L-VSI FFE using Proposed Controller during Rated Inductive and Capacitive STATCOM Operation.

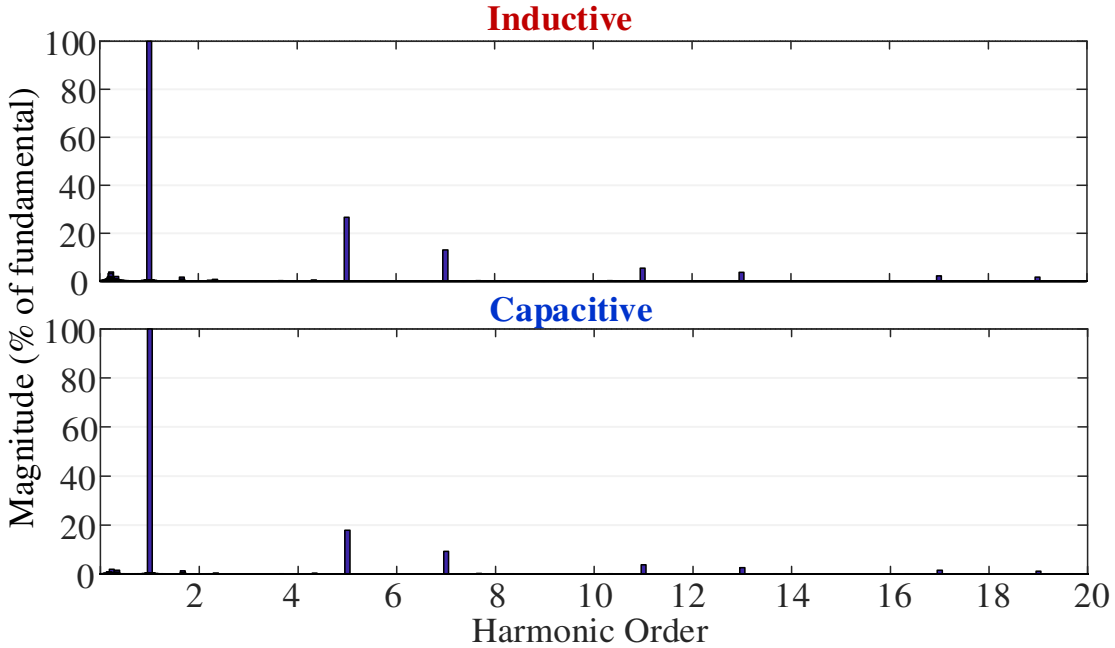

Fig. 5.24. Line Currents Harmonics of 2L-VSI FFE using Proposed Controller during Rated Inductive and Capacitive STATCOM Operation.

5.6 Summary

FFEs were introduced in low-cost low-voltage drives to operate with fundamental frequency switching, instead of the high switching frequencies used in AFEs. Adoption of FFEs in regenerative CHB drives is proposed in this work as a second solution for more cost-effective and energy efficient system by minimization of the switching power losses.

A review of the FFE control approaches present in literature shows that the biggest compromise in these controllers is between DC-link voltage utilization, DC-link voltage control, and reactive power compensation.

A new FFE controller approach was presented in this chapter to address the aforementioned challenges. The controller is based on the power flow relations in power systems between two voltage sources. The controller regulates the DC-link voltage and provides reactive power compensation. Moreover, the controller operates the FFE in six-step switching mode, which allows the highest DC-link utilization factor of 78%. Theoretical analysis was verified through simulation studies on a 2L-VSI FFE using the proposed controller.

In the following chapter, application of the FFE proposed controller in regenerative CHB drive with both six-switch and four-switch FFEs is presented. The results show that integration of FFEs can lead to more energy efficient and economic regenerative CHB drives.

Chapter 6

Proposed FFE Controller Strategy in Regenerative CHB Drives

6.1 Introduction

Fundamental frequency ends (FFEs) are a common solution for low-cost low-voltage regenerative motor drives. Triggering the switches at the fundamental frequency causes the switching power losses to be minimal, and allows more compact design of the heat sink [38]-[44]. A new FFE controller was proposed in Chapter 5 to obtain the highest DC-link voltage utilization, DC-link voltage regulation, and reactive power control.

Application of 2L-VSI FFEs using the aforementioned proposed controller in regenerative CHB MV drives is proposed in this chapter as a more economic and energy efficient solution. Just as the case of having DFEs, phase-shifting transformer is required to cancel the low order harmonics and meet the grid connection standards.

Another level of economization is also proposed by merging switching at fundamental frequency with switch-count reduction through application of FSTPI FFEs in regenerative CHB MV drives. Employing of the previously proposed phase-alternation method in Chapter 4 with phase-shifting transformer can achieve the desired low order harmonic cancellation and grid-connection standards.

Application of both proposed approaches in regenerative CHB drives, 2L-VSI FFE and FSTPI FFEs, is thoroughly analyzed. Simulation studies results using the proposed FFE controller are presented to verify the theoretical analysis. An efficiency and cost analysis was conducted to compare these solutions with the 2L-VSI AFE. The analysis shows that the two proposed solutions can reduce the power losses and the cost of the regenerative CHB drives.

6.2 Proposed Regenerative CHB Drives with 2L-VSI FFE

6.2.1 Output Voltage Analysis

Fig. 6.1 shows a regenerative power cell with 2L-VSI FFE using the proposed controller. An arbitrary leg output voltage with respect to the DC-link midpoint is shown in Fig. 6.2. In 2L-VSI FFE, the leg output voltage corresponds to the phase converter output voltage.

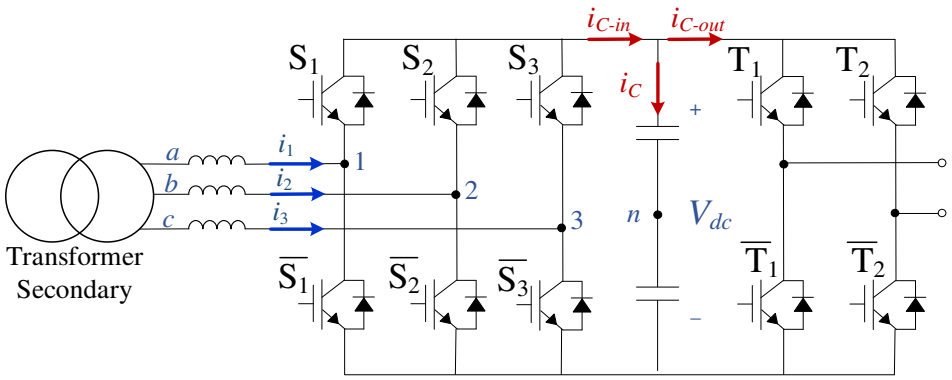

Fig. 6.1. Regenerative CHB Power Cell with 2L-VSI FFE using Proposed Controller.

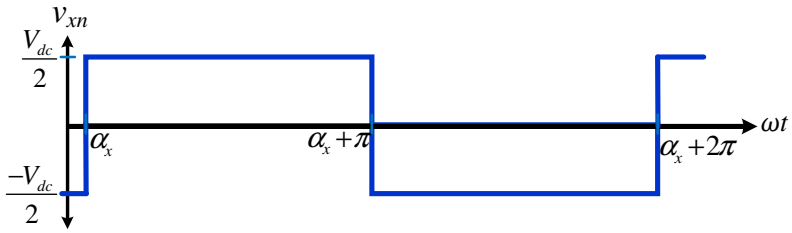

Fig. 6.2. FFE Arbitrary Leg Output Voltage using Proposed Controller.

The 2L-VSI FFE phase output voltages can be expressed using Fourier series by:

$$
\begin{aligned}
V_{1n} &= \sum_{k=0}^{\infty} \frac{2V_{dc}}{(2k+1)\pi} \sin\left((2k+1)*(\omega_g t+\alpha_1)\right) \\
V_{2n} &= \sum_{k=0}^{\infty} \frac{2V_{dc}}{(2k+1)\pi} \sin\left((2k+1)*\left(\omega_g t+\alpha_1-\frac{2\pi}{3}\right)\right) \\
V_{3n} &= \sum_{k=0}^{\infty} \frac{2V_{dc}}{(2k+1)\pi} \sin\left((2k+1)*\left(\omega_g t+\alpha_1+\frac{2\pi}{3}\right)\right)
\end{aligned}
\qquad (6.1)
$$

, where ω_g is the grid angular frequency, $2k+1$ is the odd harmonic order, and α_1 is the first phase fundamental phase shift.

The FFE phase output voltage contains all odd harmonics. However, the line-to-line voltages contain all odd non-triplen harmonics as expressed in:

$$
V_{12} = V_{1n} - V_{2n} = \frac{2\sqrt{3}V_{dc}}{\pi} \text{in}\left(\omega_g t+\alpha_1+\frac{\pi}{6}\right) + \sum_{k=1}^{\infty} \frac{2\sqrt{3}V_{dc}}{(6k\pm1)\pi} \sin\left((6k\pm1)*\left(\omega_g t+\alpha_1+\frac{\pi}{6}\right)\right) \qquad (6.2)
$$

, where $6i\pm1$ are the odd harmonic orders not divisible by three.

From (6.2), the DC-link voltage utilization factor for output line-to-line voltage is 78%, which is higher than SPWM with 3rd order harmonic injection DC-link utilization by 10%.

6.2.2 DC-Link Voltage Ripples

The three line currents in 2L-VSI FFE can be expressed by:

$$\begin{aligned} i_1 &= I\sin\left(\omega_g t+\theta_1\right)+\sum_{k=1}^{\infty} I_{6k\pm1}\sin\left(\left(6k\pm1\right)*\left(\omega_g t+\theta_{6k\pm1}\right)\right) \\ i_2 &= I\sin\left(\omega_g t+\theta_1-\frac{2\pi}{3}\right)+\sum_{k=1}^{\infty} I_{6k\pm1}\sin\left(\left(6k\pm1\right)*\left(\omega_g t+\theta_{6k\pm1}-\frac{2\pi}{3}\right)\right) \\ i_3 &= I\sin\left(\omega_g t+\theta_1+\frac{2\pi}{3}\right)+\sum_{k=1}^{\infty} I_{6k\pm1}\sin\left(\left(6k\pm1\right)*\left(\omega_g t+\theta_{6k\pm1}+\frac{2\pi}{3}\right)\right) \end{aligned} \tag{6.3}$$

, where I is the maximum fundamental magnitude, $I_{6k\pm1}$ is the magnitude for the corresponding harmonic component, θ_1 is the fundamental phase shift, and $\theta_{6k\pm1}$ is the harmonic phase shift.

Beside the fundamental component, the line currents contain odd non-tirplen harmonics. The fundamental component magnitude and phase shift depend on the required active and reactive powers. The harmonic components magnitude and phase shift depend on the line filter impedance.

The output voltage can be expressed in terms of switching states as follows:

$$\begin{bmatrix} v_{1n} \\ v_{2n} \\ v_{3n} \end{bmatrix} = \begin{bmatrix} S_1 & \overline{S_1} \\ S_2 & \overline{S_2} \\ S_3 & \overline{S_3} \end{bmatrix} \begin{bmatrix} \frac{V_{dc}}{2} \\ \frac{-V_{dc}}{2} \end{bmatrix} \tag{6.4}$$

From (6.1) and (6.4), the switching states of leg *x* can be determined as:

$$S_x = \frac{1}{2} + \sum_{k=0}^{\infty} \frac{2}{(2k+1)\pi} \sin\left((2k+1) * \left(\omega_g t + \alpha_x\right)\right)$$
$$\overline{S_x} = 1 - S_x \tag{6.5}$$

Using Kirchhoff's current law, FFE side contribution to the DC-link charging current is:

$$\begin{aligned} i_{C-in} &= S_1 \cdot i_1 + S_2 \cdot i_2 + S_3 \cdot i_3 \\ &= I_{dc} + \sum_{k=1}^{\infty} I_{6k} \cos\left(6k\left(\omega_g t + \theta_{6k}\right)\right) \end{aligned} \tag{6.6}$$

From (6.6), the DC-link capacitor charging current from FFE contains DC-components and harmonics of orders multiple of six. The DC-link voltage is given by:

$$v_C = \frac{1}{C}\int i_C dt \tag{6.7}$$

Therefore, in addition to the second-order harmonic ripples from the H-bridge side, the DC-link voltage will contain ripples of harmonic orders that are multiple of six. However, due to the dependence on the capacitance effective impedance at high frequencies, these components are very small and can be neglected.

6.2.3 Cell Input Current Harmonics

The cell input currents contain two sets of low order harmonics:

- Odd low order harmonics of orders not divisible by three, due to the application of FFE. Similar to DFE operation, most of these components can be cancelled from the primary side using the phase-shifting transformer.
- Low order harmonics of frequencies equal to $\omega_g \pm 2\omega_{out}$, where ω_{out} is the H-bridge output fundamental frequency, due to the presence of output second-order harmonics

in the DC-link voltage. These components are inherently cancelled from the primary because of the three-phase nature of the system as discussed in Chapter 4.

6.2.4 Simulation Studies

Simulation studies were conducted to verify the theoretical analysis. The system is a 3kV/160A regenerative CHB drive using a 2L-VSI FFE with the proposed controller with and FOC-controlled regenerative motor. An 18-pulse phase shifting transformer is used for the grid-interface connection. Table 6.1 shows the system parameters, per unit values are based on the system base values.

TABLE 6.1. REGENERATIVE CHB DRIVE WITH 2L-VSI FFE USING PROPOSED CONTROLLER SIMULATION SYSTEM PARAMETERS.

Rated Voltage	3 kV
Rated Current	160 A
Grid Voltage	3 kV
Phase shifting transformer ratio	3000 kV/1014 kV
Nominal frequency	60 Hz
Grid-connecting filter	10%
DC nominal reference voltage	1300 V
Capacitor value	8000 μF (50 μF/A)
Number of motor pole pairs	3
Motor rated speed	1192 rpm

a) Overall Performance

Fig. 6.3 shows overall system performance using the proposed FFE controller. The motor was operated in both rated motoring and regeneration conditions. Input reactive power is zero indicating unity power factor. Cell input current has good dynamic response during transitions. DC-link voltage is controlled during the whole operation around the nominal value of 1300V.

The converter output line-to-line voltages are shown in Fig. 6.4. As expected, the voltage waveform is 3-level quasi-square wave of $+V_{dc}$, 0, and $-V_{dc}$.

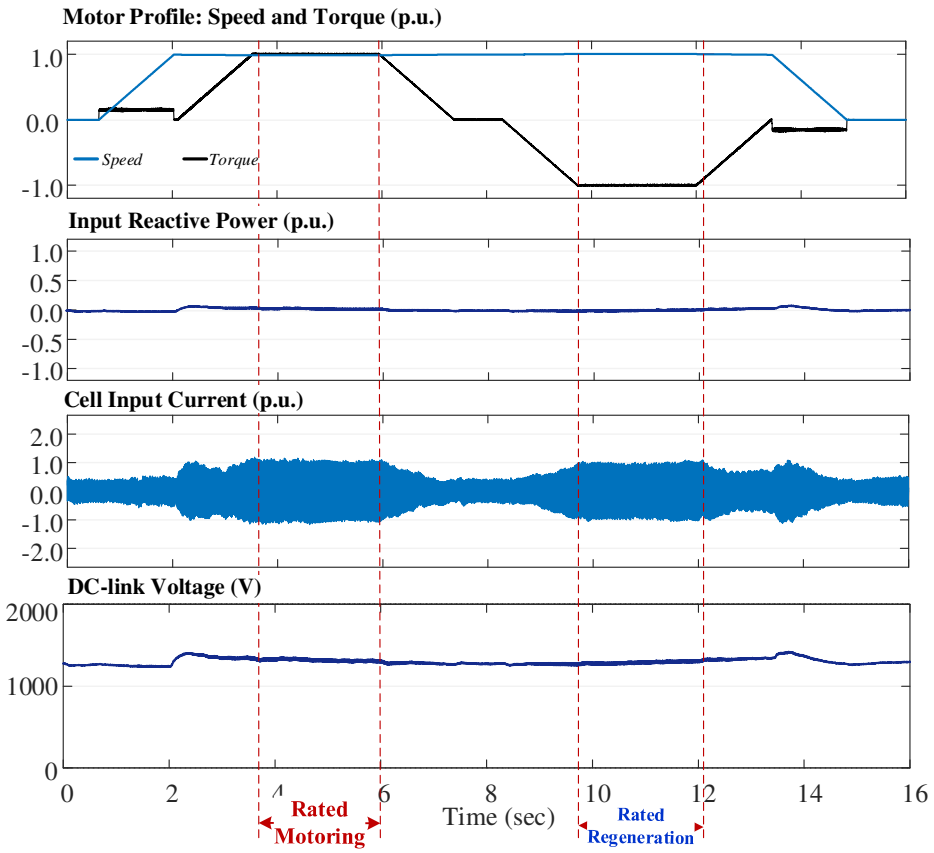

Fig. 6.3. Motor profile, Input Reactive Power, Cell Input Current, Total DC-Link Voltage in Regenerative CHB Drive with 2L-VSI FFE using the Proposed Controller.

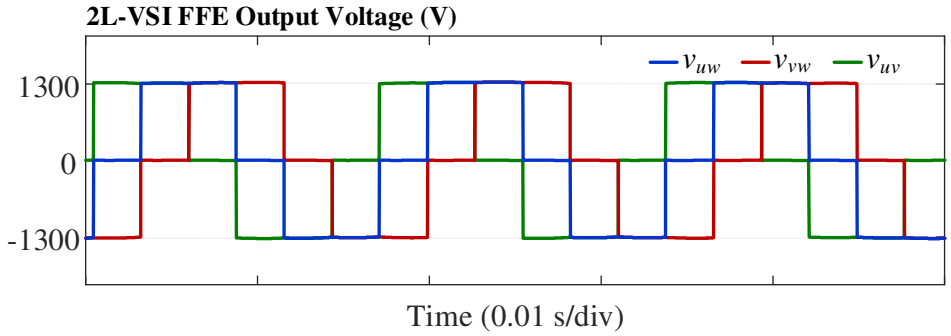

Fig. 6.4. 2L-VSI FFE Output Voltage in Regenerative CHB Drive using the Proposed Controller.

b) DC-Link Voltage Ripples and Harmonics

The details of the DC-link voltage during motoring and regeneration are shown in Fig. 6.5. The voltage is kept regulated near nominal voltage value (1300V). The output second-order voltage ripples have the highest magnitude of 0.8% as shown in Fig. 6.6. Higher order ripples are of negligible magnitude as discussed.

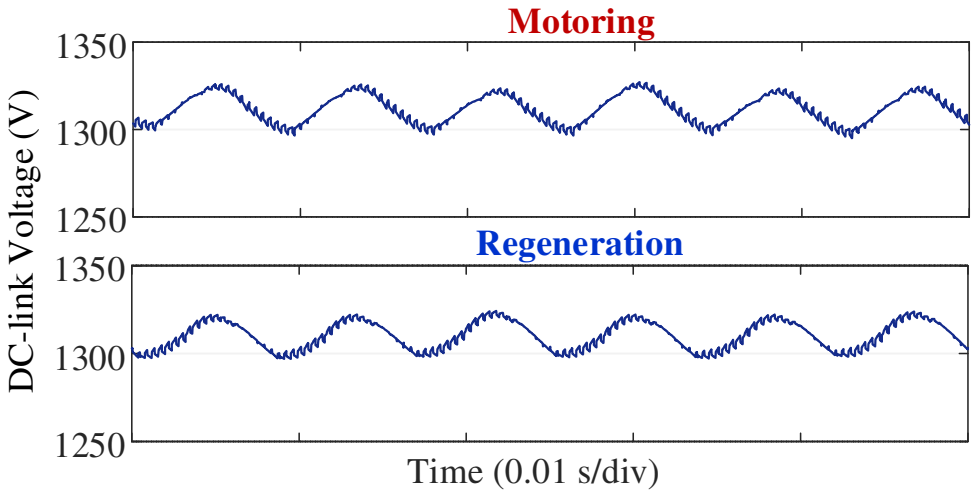

Fig. 6.5. DC-Link Voltage during Motoring and Regeneration in Regenerative CHB Drive with 2L-VSI FFE using the Proposed Controller.

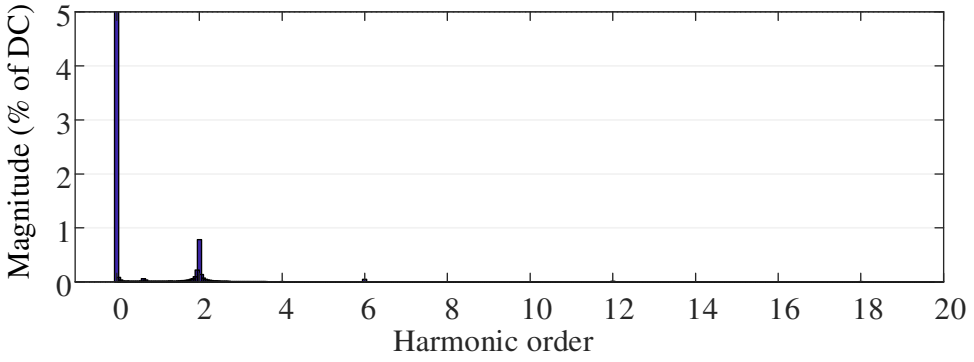

Fig. 6.6. DC-Link Voltage Harmonics in Regenerative CHB Drive with 2L-VSI FFE using the Proposed Controller.

c) Primary and Secondary Line Currents

The primary and secondary line currents are shown in Fig. 6.7. Their harmonic spectra are shown in Fig. 6.8. The secondary currents contain odd low order harmonics of orders not divisible by three. The use of phase-shifting transformer (18-pulse) in the system cancels the low order harmonics up to the 13th order, therefore the first harmonic orders to appear in the primary spectrum are the 17th and 19th, both are below the grid connection standards limits in Table 4.2 . Cancellation of low order harmonics through the phase-shifting transformer reduces the THD from 30% in the secondary to 3% the primary currents.

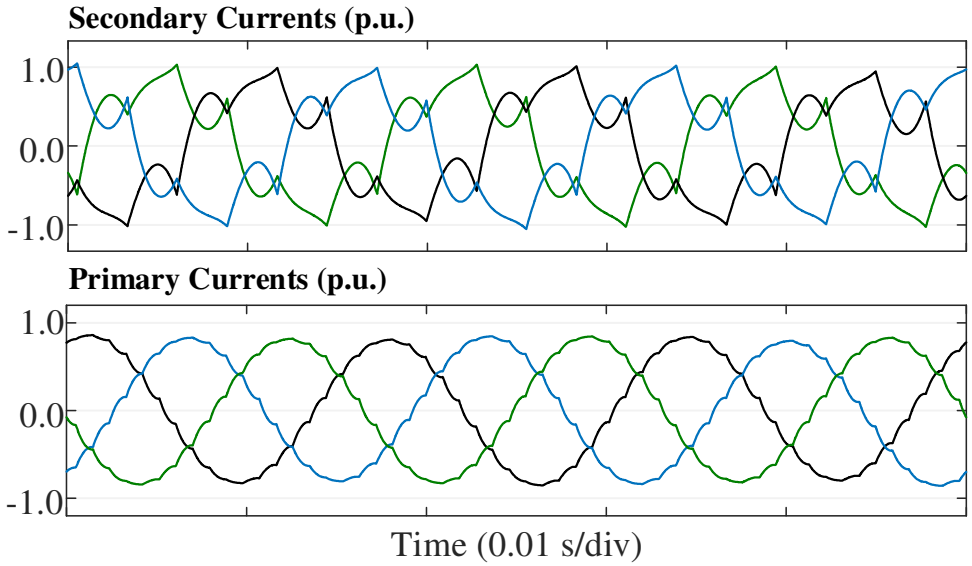

Fig. 6.7. Secondary and Primary Currents in Regenerative CHB Drive with 2L-VSI FFE using the Proposed Controller

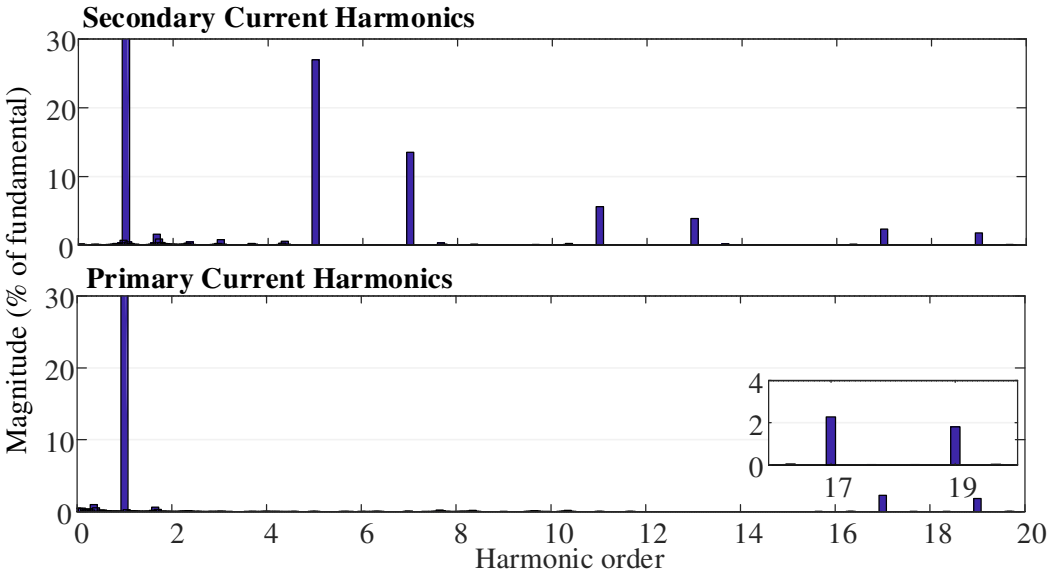

Fig. 6.8. Secondary and Primary Currents Harmonics in Regenerative CHB Drive with 2L-VSI FFE using the Proposed Controller

6.3 Proposed Regenerative CHB Drives with FSTPI FFE

6.3.1 Output Voltage Analysis

Another level of economization can be achieved by combining the switching frequency minimization with switch-count reduction. Fig. 6.9 shows a regenerative CHB power cell with FSTPI FFE using the proposed controller. The FFE leg output voltage shown in Fig. 6.2 corresponds in this case to the line-to-line voltages between any of the controlled phases and the third phase connected to the DC-link midpoint.

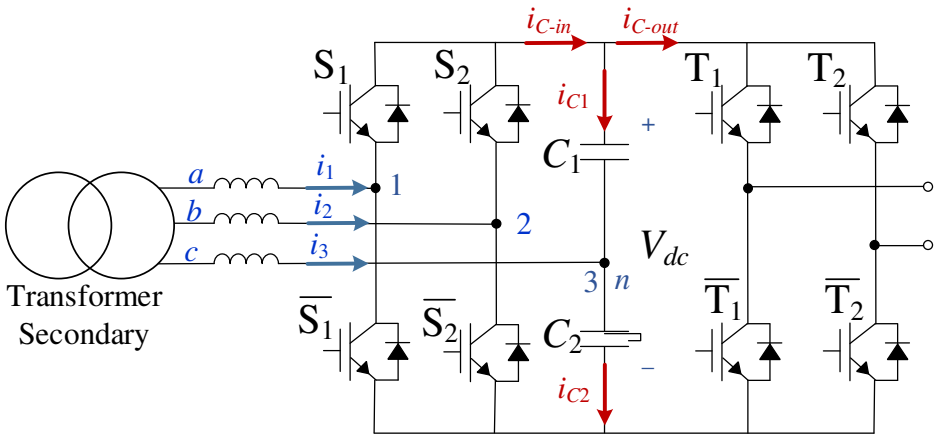

Fig. 6.9. Regenerative CHB Power Cell with FSTPI FFE using Proposed Controller.

Since the two controlled legs are always 60° apart from each other, the line-to-line voltages and phase voltages in a FSTPI FFE are respectively expressed by:

$$
\begin{aligned}
V_{13} &= \sum_{k=0}^{\infty} \frac{2V_{dc}}{(2k+1)\pi} \sin\left((2k+1)*\left(\omega_g t+\alpha_{13}\right)\right) \\
V_{23} &= \sum_{k=0}^{\infty} \frac{2V_{dc}}{(2k+1)\pi} \sin\left((2k+1)*\left(\omega_g t+\alpha_{13}-\frac{\pi}{3}\right)\right) \\
V_{12} &= V_{13}-V_{23} \\
&= \sum_{k=0}^{\infty} \frac{2V_{dc}}{(6k\pm1)\pi} \sin\left((6k\pm1)*\left(\omega_g t+\alpha_{13}+\frac{\pi}{3}\right)\right) \\
&\quad + \sum_{i=1}^{\infty} \frac{4V_{dc}}{(6i-3)\pi} \sin\left((6i-3)*\left(\omega_g t+\alpha_{13}\right)\right)
\end{aligned}
\tag{6.8}
$$

$$
\begin{aligned}
V_1 &= \sum_{k=0}^{\infty} \frac{2V_{dc}}{(6k\pm1)\sqrt{3}\pi} \sin\left((6k\pm1)*\left(\omega_g t+\alpha_{13}\pm\frac{\pi}{6}\right)\right) \\
&\quad + \sum_{i=1}^{\infty} \frac{2V_{dc}}{(6i-3)\pi} \sin\left((6i-3)*\left(\omega_g t+\alpha_{13}\right)\right) \\
V_2 &= \sum_{k=0}^{\infty} \frac{2V_{dc}}{(6k\pm1)\sqrt{3}\pi} \sin\left((6k\pm1)*\left(\omega_g t+\alpha_{13}\mp\frac{\pi}{2}\right)\right) \\
&\quad + \sum_{i=1}^{\infty} \frac{2V_{dc}}{(6i-3)\pi} \sin\left((6i-3)*\left(\omega_g t+\alpha_{13}-\pi\right)\right) \\
V_3 &= \sum_{k=0}^{\infty} \frac{2V_{dc}}{(6k\pm1)\sqrt{3}\pi} \sin\left((6k\pm1)*\left(\omega_g t+\alpha_{13}\pm\frac{5\pi}{6}\right)\right)
\end{aligned}
\tag{6.9}
$$

, where ω_g is the grid angular frequency, and α_{13} is the fundamental angle shift in for V_{13}.

As shown in (6.8), the line to line voltages contain all odd harmonics, including the triplen harmonics. The DC-link voltage utilization for output line-to-line voltage is 45%, this is 28.5% more than when using SPWM with the FSTPI AFE. In (6.9), the phase output voltages, and consequently the line currents, contain balanced odd harmonics that are not divisible by three. The two controlled phases contain triplen harmonics that are 180^o apart as discussed in chapter 4, while the uncontrolled phase does not contain any triplen harmonics.

6.3.2 Capacitors' Voltage Ripples

The analysis of the capacitors' voltage ripples is similar to the case of using SPWM with third order harmonic injection discussed in Chapter 4. In addition to output second order harmonics, the individual capacitors' voltages will contain input fundamental, and low magnitude of even low order harmonics due to the interaction between the switching states and the input current components. All these components except for the fundamental show on the total DC-link voltage.

6.3.3 Cell Input Current Harmonics

The cell input currents contain three sets of low order harmonics:

1. Balanced odd low order harmonics of orders not divisible by three, due to the application of FFE. Most of these components can be cancelled from the primary side using the phase-shifting transformer.
2. Triplen harmonics in the two controlled phases line currents that are 180^o out of phase. These harmonics can be cancelled using the phase alternation method

proposed in chapter 4 (Fig 4.9).

3. Low order harmonics of frequencies equal to $\omega_g \pm 2\omega_{out}$, where ω_{out} is the H-bridge output fundamental frequency, due to the presence of output second-order harmonics in the DC-link voltage. These components are cancelled from the primary due the three-phase nature of the system as discussed in chapter 4.

6.3.4 Simulation Studies

To verify the theoretical analysis, simulation studies on the same system used for the 2L-VSI FFE analysis were conducted. Phase alternation method shown in Fig. 4.9 was used to connect the cells to the secondary windings of the 18-pulse phase-shifting transformer. The system parameters are shown in table 6.2, where per unit values are based on the system ratings.

TABLE 6.2. REGENERATIVE CHB DRIVE WITH FSTPI FFE USING PROPOSED CONTROLLER SIMULATION SYSTEM PARAMETERS.

Rated Voltage	3 kV
Rated Current	160 A
Grid Voltage	3 kV
Phase shifting transformer ratio	3000 kV/585 kV
Nominal frequency	60 Hz
Grid-connecting filter	10%
DC nominal reference voltage	1300 V
Capacitor value	8000 μF (50 μF/A)
Number of motor pole pairs	3
Motor rated speed	1192 rpm

a) Overall Performance

Fig. 6.10 shows overall system performance. The motor was operated in both rated motoring and regeneration conditions using FOC scheme. Input reactive power is zero throughout the operation indicating unity power factor. Cell input current has very good dynamic response during transitions. DC-link voltage is controlled during the whole operation at the reference value of 1300V, while the two capacitor's voltages are kept each at 650V. The FSTPI FFE output line voltages in one cell are shown in Fig. 6.11. As discussed, the two controlled line voltages (v_{uw} and v_{vw}) are two level between $+V_{dc}/2$ and $-V_{dc}/2$, while the third line to line voltage (v_{uv}) is three level between $+V_{dc}$, 0, and $-V_{dc}$.

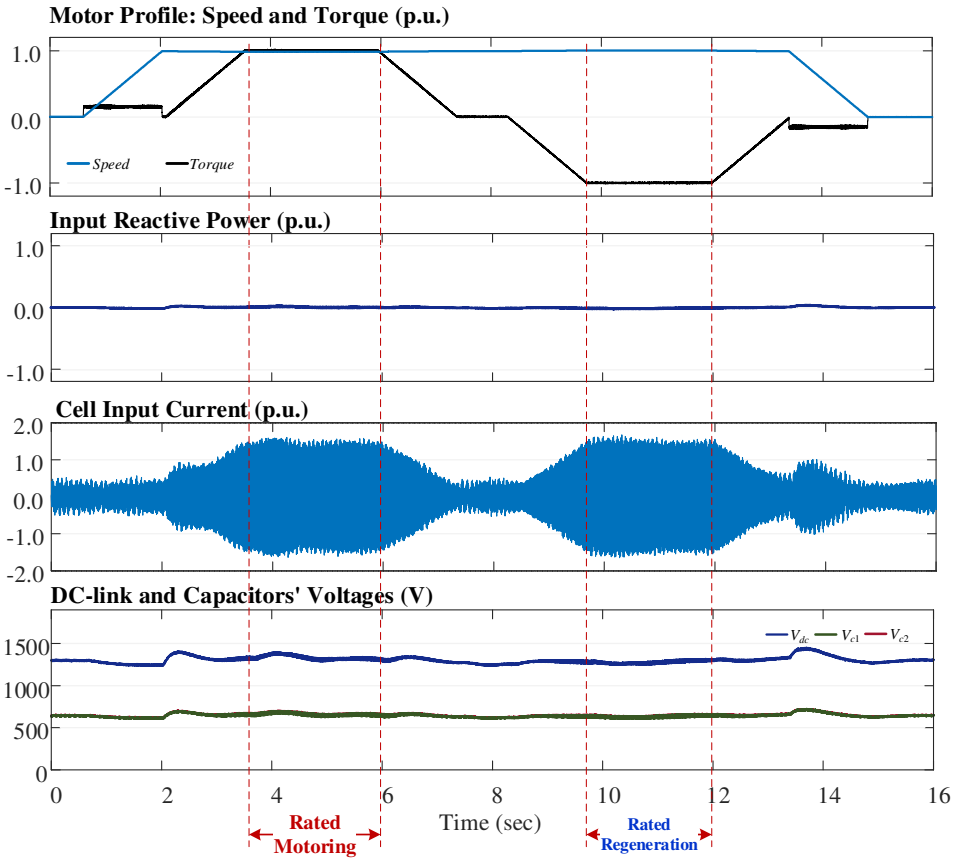

Fig. 6.10. Motor profile, Input Reactive Power, Cell Input Current, Total DC-Link Voltage in Regenerative CHB Drive with FSTPI FFE using the Proposed Controller.

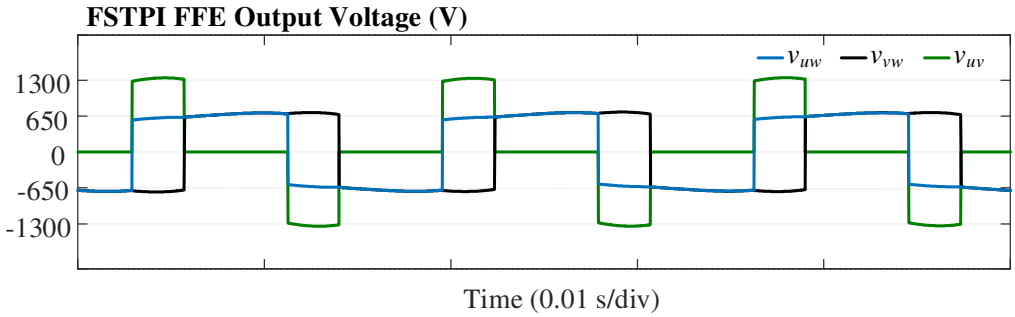

Fig. 6.11. FSTPI FFE Output Voltage in Regenerative CHB Drive using the Proposed Controller.

b) Capacitors' and DC-Link Voltage Regulation and Harmonics

The capacitors' voltages during motoring and regeneration are illustrated in Fig. 6.12, both capacitors' voltages are balanced and are kept around the average nominal voltage of 650 V. The total DC-link voltage during motoring and regeneration is shown in Fig. 6.13 with ripples below 1%. The harmonic analysis of the capacitors' and total DC-link voltages is shown in Fig. 6.14. As discussed, the individual capacitors' voltages contain fundamental, second, and fourth order harmonics. However, the fundamental component is cancelled from the DC-link total voltage harmonics.

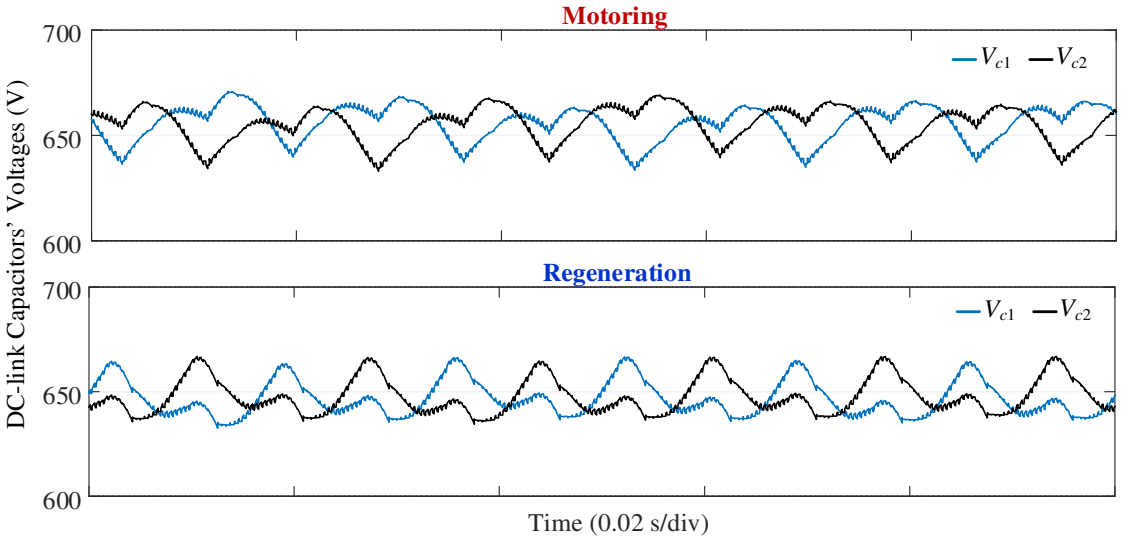

Fig. 6.12. DC-link capacitors' Voltages during Motoring and Regeneration in Regenerative CHB drive with FSTPI FFE using Proposed Controller.

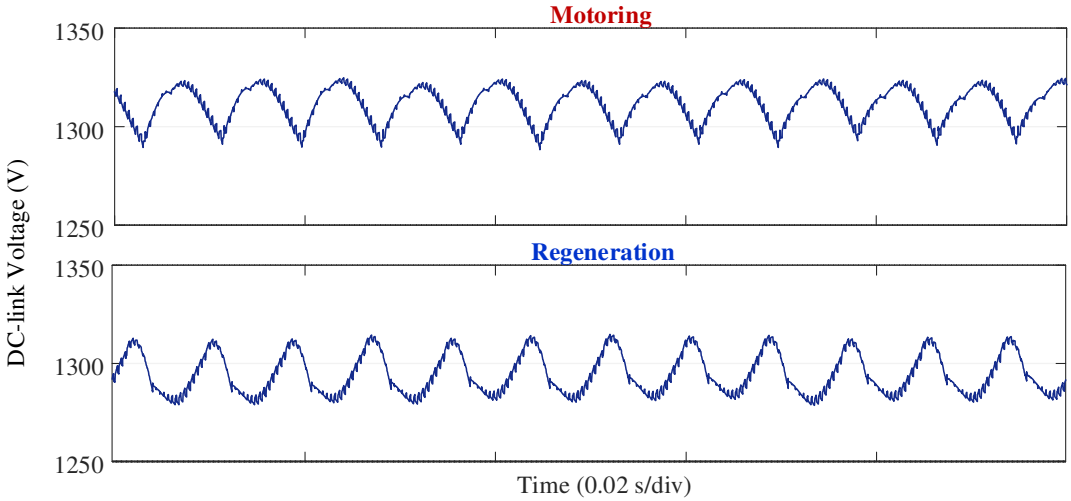

Fig. 6.13. DC-link Voltage during Motoring and Regeneration
in Regenerative CHB drive with FSTPI FFE using Proposed Controller.

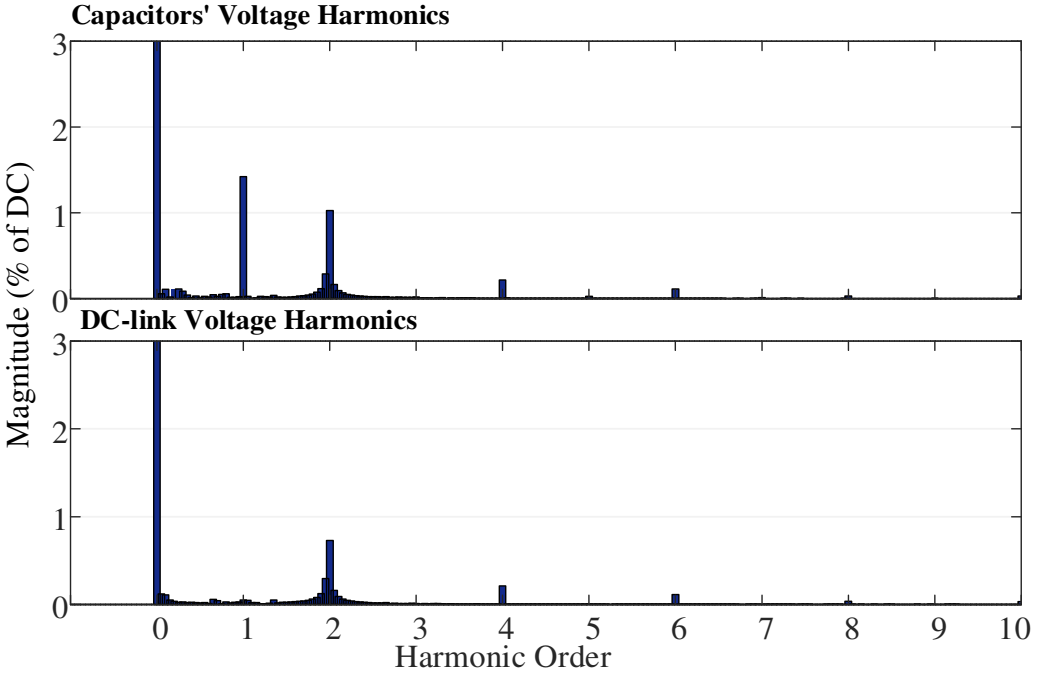

Fig. 6.14. DC-Link Capacitors' and Total Voltages Harmonics in Regenerative CHB drive with FSTPI FFE using Proposed Controller.

c) Primary and Secondary Line Currents

The primary and secondary line currents waveforms are shown in Fig. 6.15. The harmonic spectra of one of the controlled phase currents and primary current are shown in Fig. 6.16. The controlled phase secondary currents contain all odd low order harmonics including the triplen harmonics. The use of proposed phase-alternation method cancels all triplen harmonics from the primary currents, while the 18-pulse phase-shifting transformer cancels other odd low order harmonics up to the 13th order. The remaining harmonics are kept below the grid standards limits, and the THD is reduced from 58% in the secondary currents to 2.5% in the primary currents.

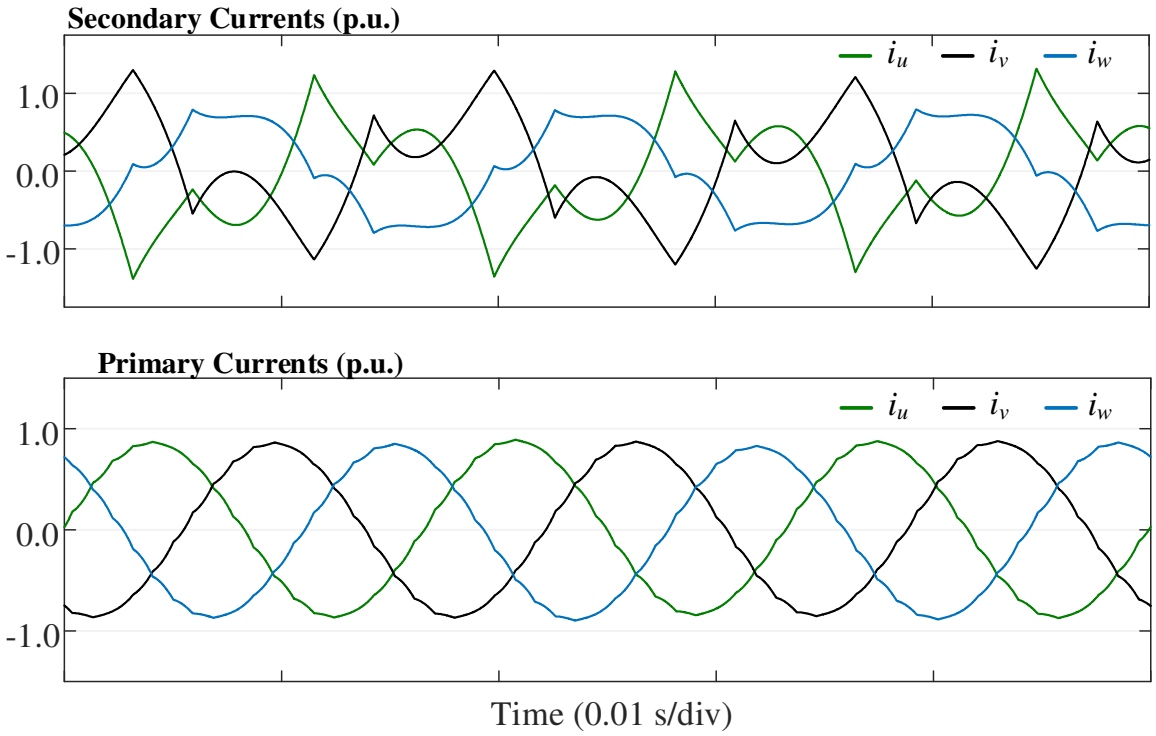

Fig. 6.15. Secondary and Primary Currents in Regenerative CHB drive with FSTPI FFE using Proposed Controller.

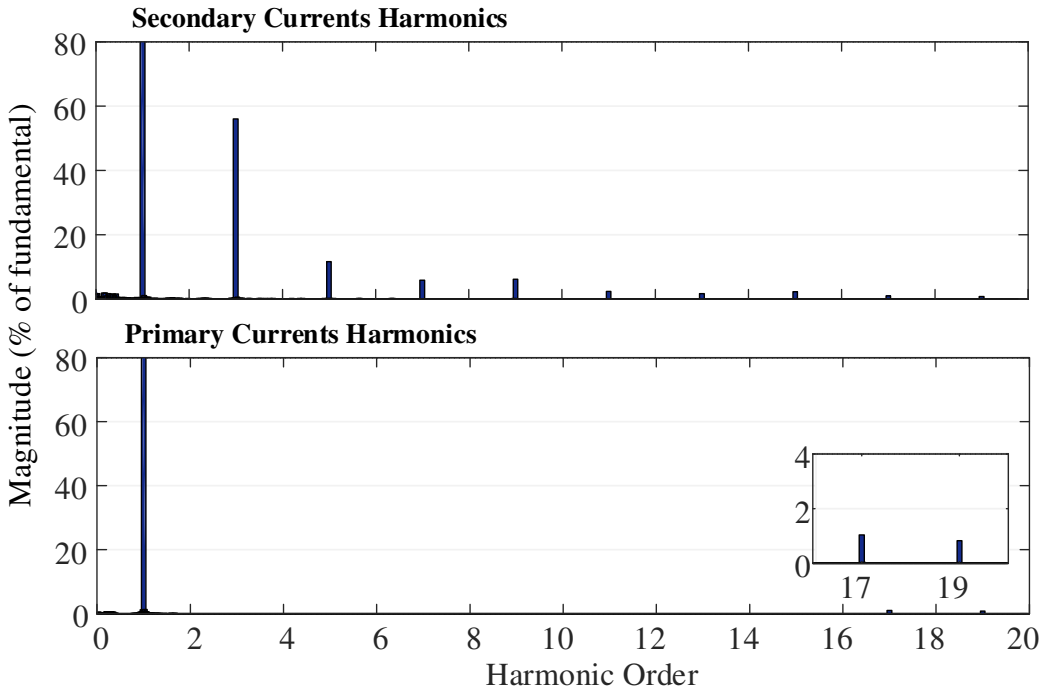

Fig. 6.16. Secondary and Primary Currents Harmonic in Regenerative CHB drive with FSTPI FFE using Proposed Controller.

6.4 Efficiency and Cost Analysis

To get a measure of how using fundamental frequency switching will affect the total drive efficiency, power loss calculation and switches' cost calculation for the simulated 3kV/160A 7-level regen CHB system was conducted for the following scenarios:

- 2L-VSI AFE.
- 2L-VSI FFE.
- FSTPI FFE.

The simulation was conducted using Infineon power loss calculation software IPOSIM. Table 6.3 shows simulation parameters. The input secondary voltages and thus the fundamental current ratings were chosen based on the maximum DC-link voltage utilization. A typical switching frequency of 1200 Hz was chosen for the AFE operation.

TABLE 6.3. EFFICIENCY ANALYSIS: POWER LOSS CALCULATION PARAMETERS

Front End	**2L-VSI AFE**	**2L-VSI FFE**	**FSTPI FFE**
Input Voltage	920 V	1014V	585V
Nominal Current	58 A	53 A	91 A
Secondary Input Current Multiplication Factor ($\sqrt{1+THD^2}$)	1	1	1.16
Switching Frequency (Hz)	1200	60	60

The current multiplication factor aims to calculate the switches' r.m.s. current based on the secondary input current THD based on:

$$THD = \frac{100 * \sqrt{\sum_{h=2}^{\infty} I_{h,rms}^2}}{I_{1,rms}} \qquad (6.10)$$

$$\therefore I_{rms} = I_{1,rms}\sqrt{1+THD^2}$$

, where *h* is the harmonics order.

Fig. 6.17 shows the system cost and power losses normalized to the 2L-VSI AFE results as a benchmark. The lowest power losses occur in 2L-VSI FFE with only 35% of the 2L-VSI AFE based system. The FSTPI FFE has the least switches' cost (67% of the 2L-VSI), while the power losses are intermediate (58% of 2L-VSI AFE) due to the increased current rating which is always a compromise in reduced switch-count topologies. The results show that using FFEs in regenerative CHB is both energy efficient, and cost effective.

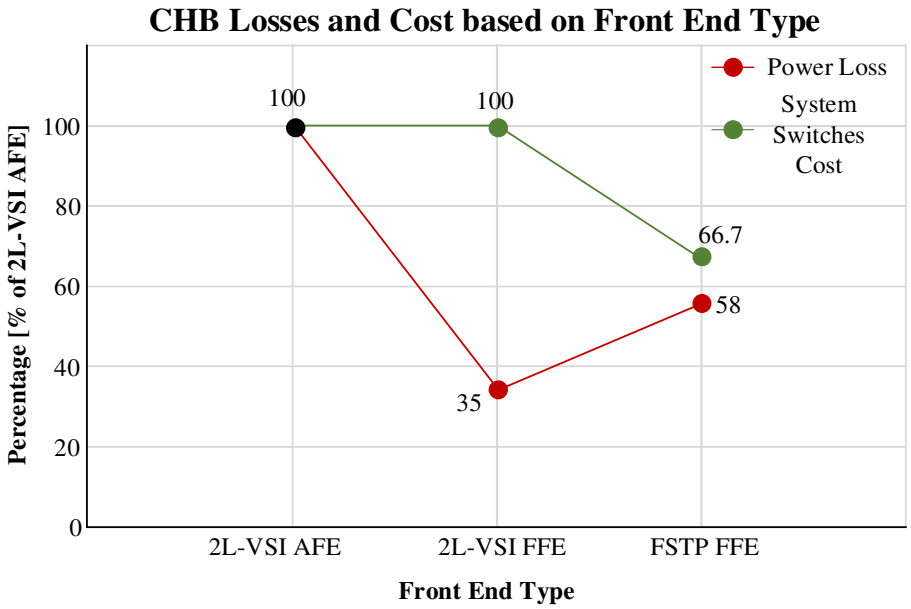

Fig. 6.17. CHB System Power Losses and Switches' Cost for Proposed FFEs vs. 2L-VSI AFE.

6.5 Summary

FFEs are introduced as another solution to have more economic and efficient regenerative CHB motor drives by minimizing the switching power losses. Application of 2L-VSI FFEs in regenerative CHB motor drives using the proposed controller has been analyzed theoretically and using simulation studies. The phase-shifting transformer is used to cancel low order harmonics from the primary currents to comply with the grid connection standards. Another step further is combining both switch-count reduction and switching losses reduction by employing FSTPI FFEs in regenerative CHB motor drives using the proposed controller. In this case, phase-shifting transformer along with proposed phase-alternation connection are used to cancel low order harmonics from the primary currents and comply with the grid standards. Simulation studies, and efficiency and cost analysis of both solutions show they exhibit a promising potential as a highly economic and energy efficient solutions for regenerative CHB motor drives.

Chapter 7

Experimental Implementation and Validation

7.1 Experimental Implementation of Regenerative CHB Drive

To verify the theoretical and simulation analysis of the proposed methods discussed throughout the thesis, a scaled-down version of the 7-Level CHB MV motor drive was implemented. Active front ends were integrated to the system to add regeneration capability. The setup was developed in cooperation with the rest of the motor drives research team in High Power Electronics Lab (HiPEL) at McMaster University as a part of the research collaboration project with the R&D team in Rockwell Automation Canada.

An overall view of the system is shown in Fig. 7.1. The developed system is meant to have a flexible configuration so that different topologies can be implemented on the front end side.

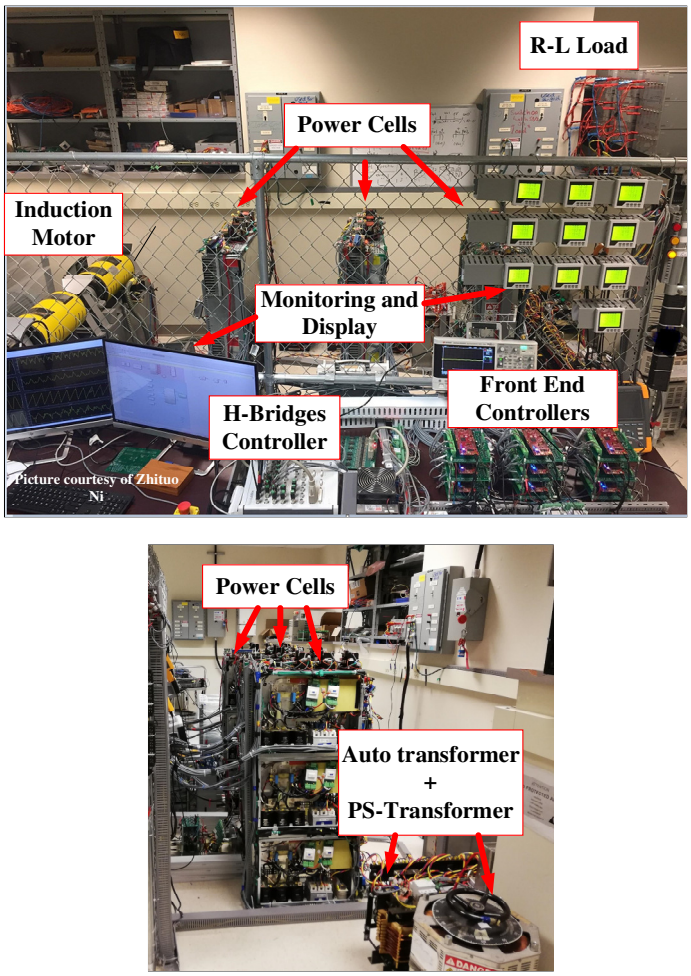

Fig. 7.1. The Experimental Setup Overview.

The system structure consists of :

1. Power circuits, which include the phase-shifting transformer, and the drive power cells.
2. Measurement circuits including voltage and current sensors for feedback signals.

3. Front ends and drive output controllers.
4. Loads.
5. Display and Monitoring.

7.1.1 Power Circuits

An 18-pulse phase-shifting (PS) transformer is used to connect the system to the grid. The presence of phase-shifting transformer is mainly to cancel low order harmonics in case of having DFE or FFE operation.

Fig. 7.2 shows the components of one of the nine power cells used in the system. For non-regenerative operation with DFE, a 1.7kV/60A three-phase diode bridge is used (not shown in the figure). To add regeneration capability, three 1.2kV/50A IGBT half-bridge modules (FF1-3) are connected in parallel to the diode bridge. The contactors (K1 and K2) are used to switch between DFE and AFE operations. For the DC-link implementation, six 400V/4700μF electrolytic capacitors (C_6) are used to produce different capacitance values with different voltage and current ratings. The grid-connection filter (L1) is 4 mH. A 1.2kV/50A IGBT half-bridge module (FF4) (not shown in the figure) connects the DC-link to a chopper resistance for overvoltage protection. For the output H-bridge side, two 1.2kV/50A IGBT modules (FF5-6) are used. The gate drivers G1-G6, are to control the front end, the chopper and the H-bridge IGBT modules.

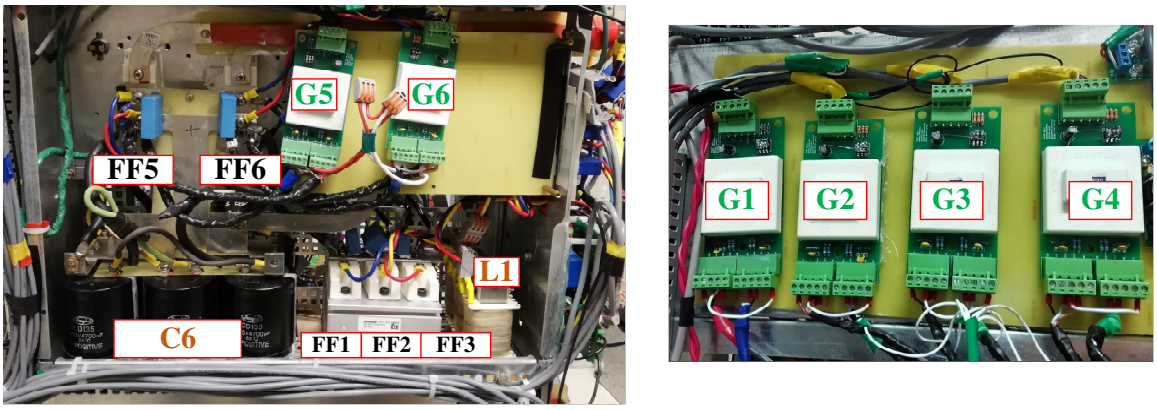

(a) Power switches, DC-link capacitors, grid-connection filter, and Gate drivers.

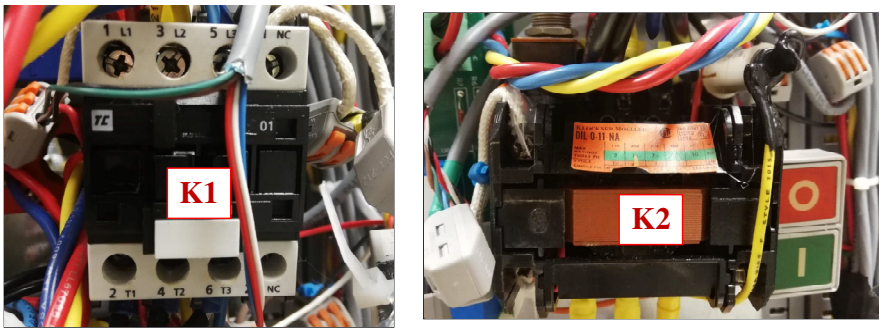

(b) Cell Control Contactors.

Fig. 7.2. Power Cell Components.

7.1.2 Measurement Circuits

Fig. 7.3(a) shows the front end voltage measurements boards used for each cell. Each board has three voltage sensors to provide the measurements required for PLL operation and DC-link voltage control.

Fig. 7.3(b) shows the front end current sensor boards used in each cell to provide the line current measurements required for control and protection.

Fig. 7.4 shows the drive output voltage and current measurement board. These measurements are used in the drive output control.

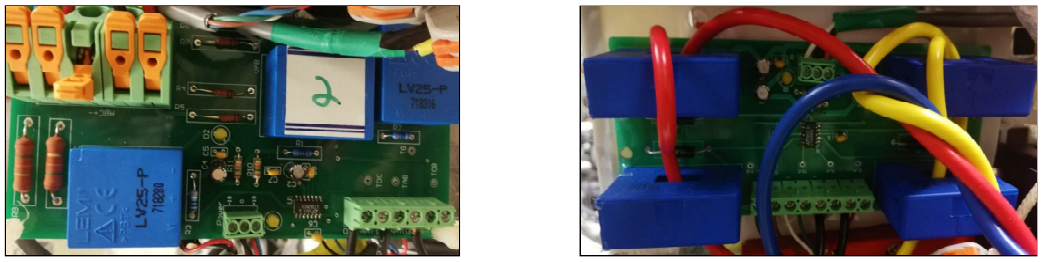

(a) Voltage Sensor Board. (b) Current Sensor Board.

Fig. 7.3. Cell Front End Sensor Boards.

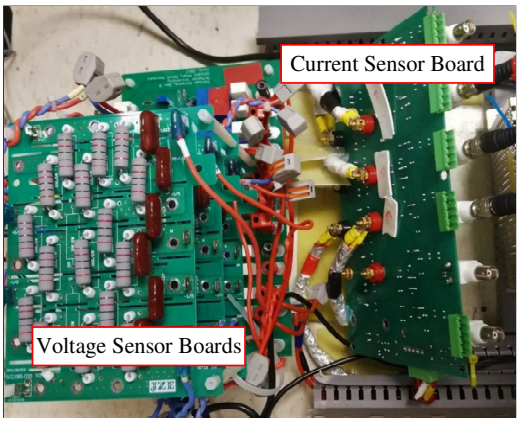

Fig. 7.4. Drive Output Measurements Boards.

7.1.3 Digital Controllers

Fig. 7.5 shows the front end controller boards. Ten DSP interface boards were designed, nine of the DSP controllers are programmed as slave controllers for driving and monitoring the AFE performance in single power cell. The tenth controller is programmed to be a master controller for overall system monitoring and communication with the motor controller. Each DSP board contains:

1. C2000 Delfino MCUs F28379D LaunchPad for control.
2. Analog input interface for the voltage and current sensors readings.
3. Interface circuits with the motor controller and gate drivers.
4. Synchronization and communication interfaces between different MCUs.

The drive output control was achieved using dSpace MicroLabBox shown in Fig. 7.6. The drive output voltage and current are used by the microprocessor along with more inputs such as the speed in case of motor load to control the output H-bridges gating signals.

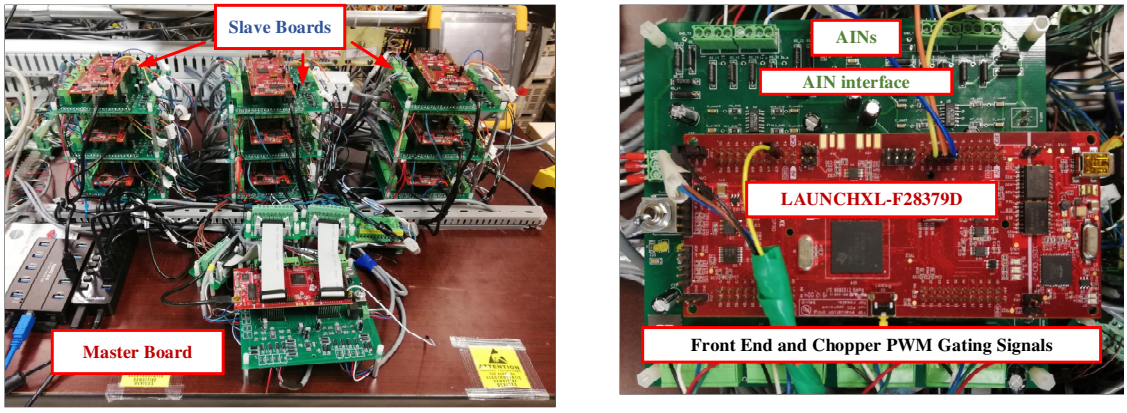

Fig. 7.5. Front End Controllers.

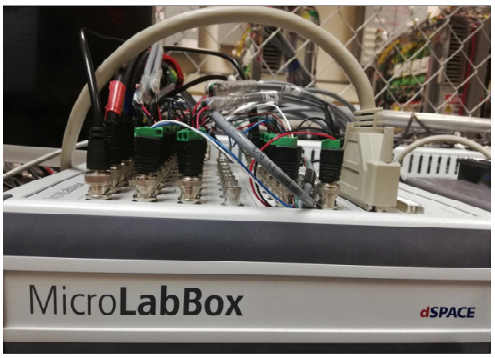

Fig. 7.6. Drive Output Controller.

7.1.4 Loads

Two types of loads can be connected to the system as shown in Fig. 7.1:

1. 10 kW R-L load, which can be controlled through either open-loop or closed-loop control schemes.
2. 15 kW motor-generator set for motoring and regeneration operation. The motor can be controlled through closed loop *v/f* or FOC control schemes.

7.2 Experimental Validation of Proposed Reduced Switch-Count Configuration with SPWM

To verify the theoretical and simulation analysis throughout the thesis, the experimental results of the experimental setup operation using the proposed FSTPI-AFE are presented using regular SPWM, as it was found to have better overall performance. Preliminary results are obtained with R-L load and STATCOM operation injecting rated reactive power to the system. Due to the restrictions of time, operation with regenerative motor and the experimental validation of FFE controller and its application on the setup are considered in the future work.

The results were obtained using DC-link of 4700 μF capacitance, and 4mH grid connection filer. The input voltage for the secondary cells is 45V and the DC-link voltage is 180 V.

To have a clear investigation of the capacitors and total DC-link performance, a single cell was first run with 600 W R-L load.

Fig. 7.7 shows the two capacitors' voltages. Their values are balanced at 90 V. Their input fundamental ripples are 180° out of phase as analyzed, while they both contain the same output second order ripples.

Fig. 7.8 shows the two capacitors' voltages in comparison with the total DC-link voltage. The DC-link is kept at 180 V, and contains only output second order harmonic ripples.

The cell input currents are shown in Fig. 7.9 with evident current unbalance and switching harmonics existence.

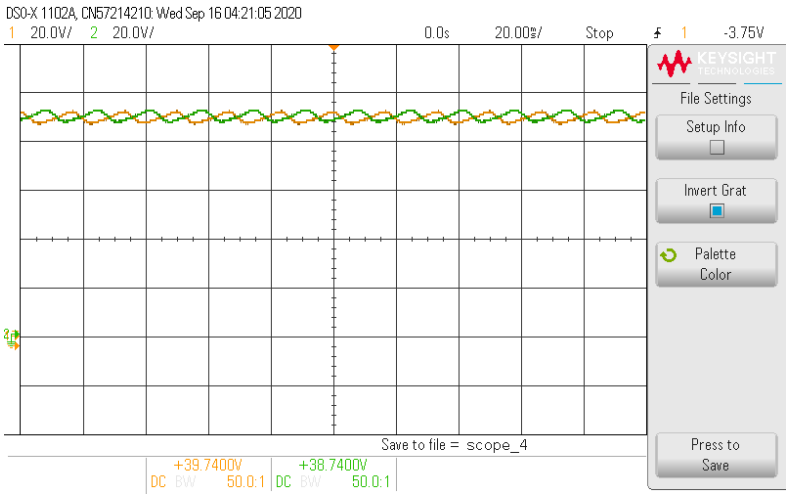

Fig. 7.7. Experimental results for Capacitors' Voltages
in the Proposed FSTPI-AFE Based Power cell with SPWM.

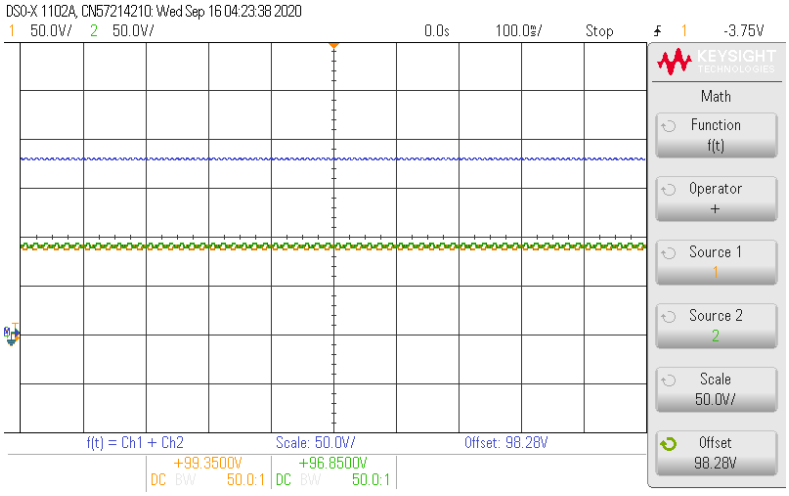

Fig. 7.8. Experimental Results for Capacitors' and Total DC-Link Voltage
in the Proposed FSTPI-AFE Based Regenerative CHB Drive with SPWM.

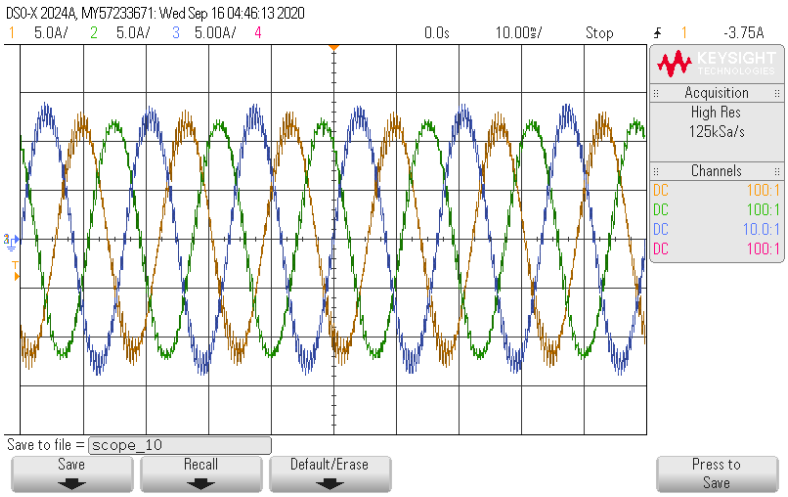

Fig. 7.9. Experimental Results for Cell Input Current
in the Proposed FSTPI-AFE Based Regenerative CHB Drive with SPWM.

To validate the whole system operation and its ability to interact with the grid, the system was operated as a STATCOM to inject 5 kVA to the grid.

Fig. 7.10(a) shows the primary currents without applying any of the proposed methods of phase alternation or carrier phase shifting. Fig. 7.11(a) shows the corresponding harmonic spectrum. As expected, the secondary currents unbalance and switching harmonics are reflected to the primary side leading to high THD.

Fig. 7.10(b) shows the primary currents when the proposed phase alternation connection is applied. The corresponding harmonic spectrum is shown in Fig. 7.11(b). The proposed phase alternation connection is validated to eliminate the current unbalance and cancel the carrier harmonics. The THD is highly improved.

Fig. 7.10(c) shows the primary currents when the proposed method I of carrier phase-shifting is employed due to the existence of phase-shifting transformer. Their harmonic spectrum is shown in Fig. 7.11(c). The results shows how the unbalance and harmonics are highly reduced compared with the other two scenarios.

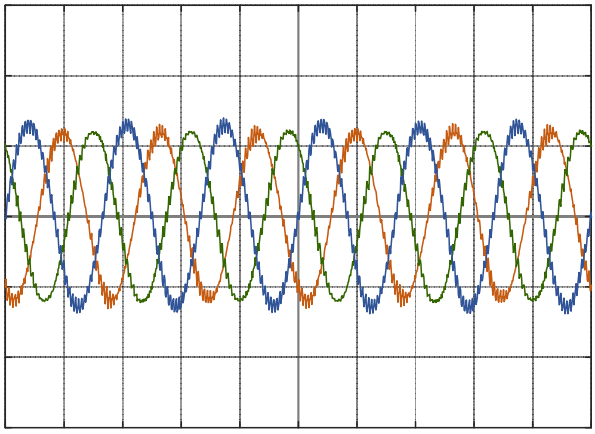

(a) **Case 1:** No phase alternation or carrier phase-shifting.
Time Scale: (10 ms/div) Current Scale: (20 A/div)

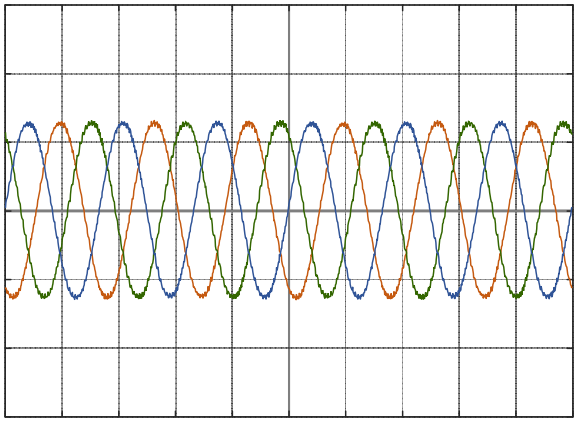

(b) **Case 2:** Using proposed phase alternation method.
Time Scale: (10 ms/div) Current Scale: (20 A/div)

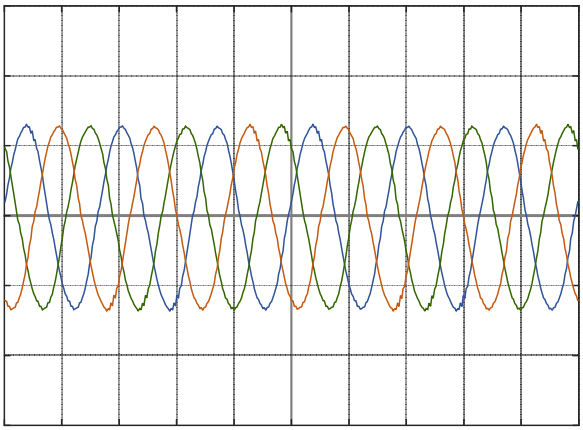

(c) **Case 3:** Using Proposed Carrier Phase-shifting method I.
Time Scale: (10 ms/div) Current Scale: (20 A/div)

Fig. 7.10. Experimental Results for Primary Currents
in the Proposed FSTPI-AFE Based Regenerative CHB Drive with SPWM.

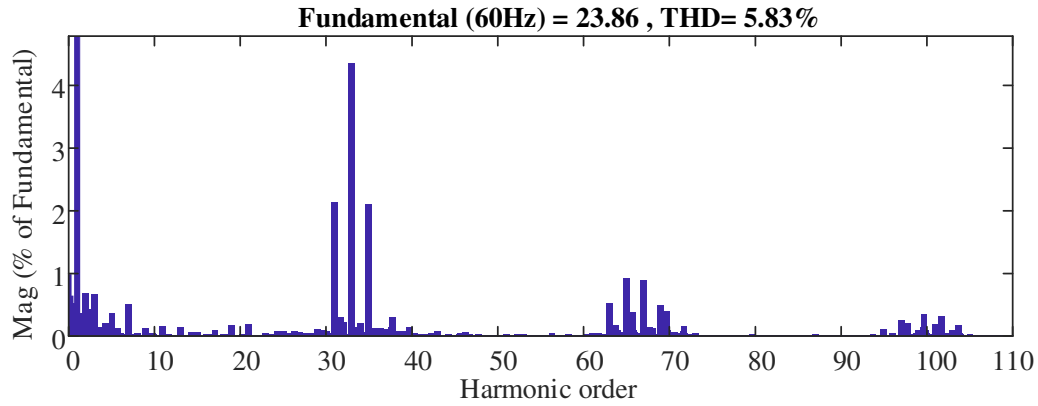

(a) **Case 1:** No Phase Alternation or Carrier Phase-Shifting.

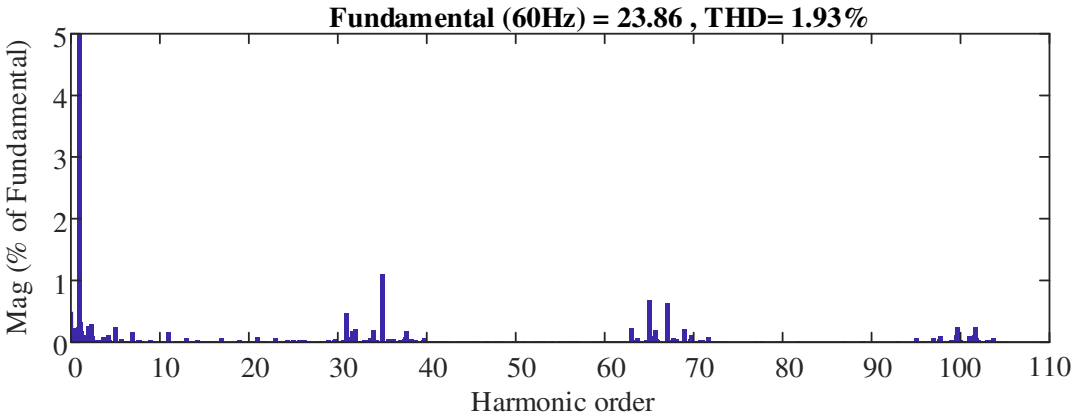

(b) **Case 2:** Using Proposed Phase Alternation Method.

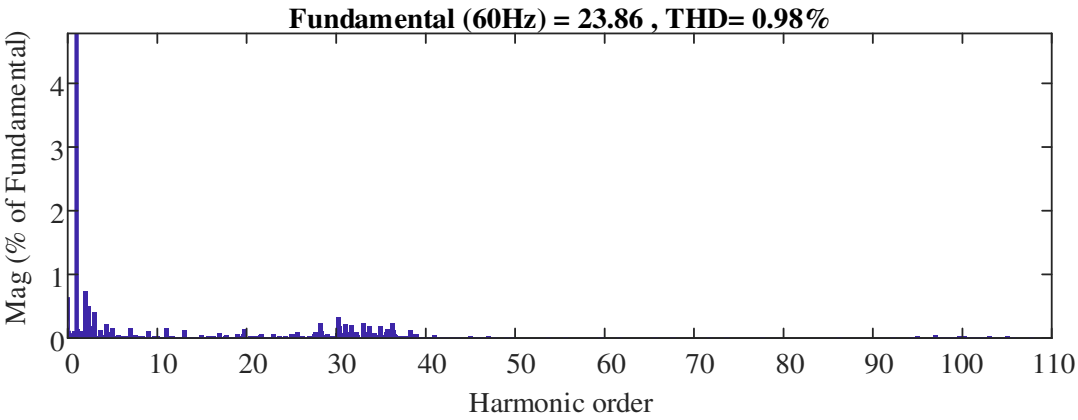

(c) **Case 3:** Using Proposed Carrier Phase-Shifting Method I.

Fig. 7.11. Experimental Results for Primary Currents Harmonic Analysis in the Proposed FSTPI-AFE Based Regenerative CHB Drive with SPWM.

Fig. 7.12 shows the results for phase A secondary currents in three cells with and without carrier phase shifting. The results demonstrate how the carrier phase-shifting technique affect the switching harmonics so that they are cancelled in the primary currents.

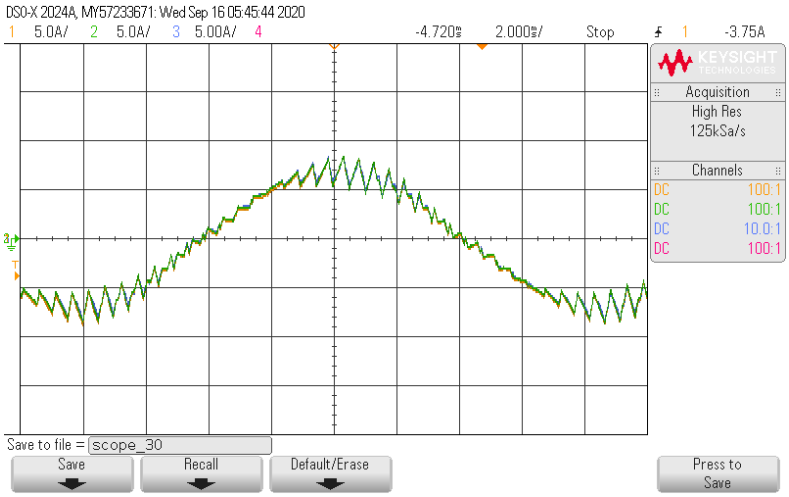

(a) Without Carrier Phase-Shifting.

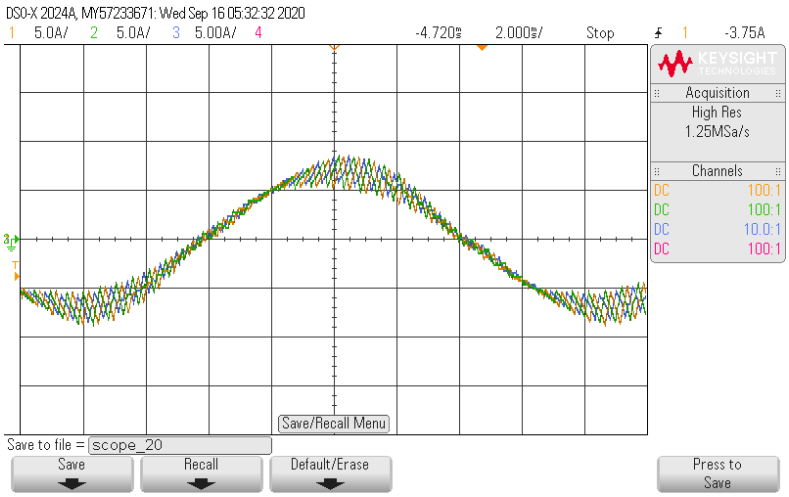

(b) With Carrier Phase-Shifting

Fig. 7.12. Experimental Phase A Secondary Currents in Three Cells Without and With Carrier Phase-Shifting in the Proposed FSTPI-AFE Based Regenerative CHB Drive with SPWM.

Chapter 8

Conclusions and Future Work

8.1 Thesis Summary

Among different multilevel inverter topologies, cascaded H-bridge (CHB) multilevel inverters are widely used in the motor drives applications due to their modularity, redundancy, fault tolerant capability, and high power quality on both motor and grid sides. The typical structure of CHB motor drives comprises diode rectifiers in the front end which allow unidirectional power flow from the grid to the motor. However, in certain types of loads, such as lifts and conveyors, the power can be regenerated from the load side. Unless the installed drive allows bidirectional power flow, this regenerated power would have to be dissipated resulting in system inefficiency, higher cost, and increased carbon footprint.

To obtain a regenerative version of CHB drives, the diode rectifier is typically replaced with a three-phase PWM rectifier to have active front end (AFE). This solution comes at the cost of increased number of switches to become ten switches in each CHB cell instead of only four switches in case of the non-regenerative drives. The increase in switches' number is associated with increase in cost, power losses, system complexity, and bulkiness. These challenges hinder the economic viability of a regenerative CHB drive.

The objective of this thesis is to research solutions for more economic and efficient regenerative CHB drives. Two solutions are investigated in this thesis:

- Switch-count reduction.
- Minimization of the switching frequency and the associated power losses.

A detailed literature review of the existing reduced switch-count regenerative CHB configurations shows that their dependency on single-phase AFEs is accompanied with many challenges such as DC-link voltage ripples, and limitation of input current low order harmonics cancellation by the number of cells. To overcome these issues, two potential reduced switch-count configurations based on three-phase AFE are reviewed with their pros and cons. Based on this comparison, one of them is selected as the preferable configuration to be further investigated.

The selected configuration employs a four-switch three-phase inverter (FSTPI) AFE and thus reduces the switch-count in each CHB cell by two switches. Thorough analysis of the FSTPI and its standalone operation reveals three main challenges: capacitors' voltage imbalance due to DC-link midpoint connection, current unbalance and triplen harmonics, and the need for very high switching frequency or a trap filter to comply with the grid

connection standards (IEEE std. 519-2014). Nevertheless, these issues are solved using integration of FSTPI in the CHB modular structure:

- Due to grid connection, the capacitors' voltages are proven to be inherently balanced.
- A proposed phase alternation connection between cells to the transformer secondary windings can eliminate the current unbalance and triplen harmonics.
- Two carrier shifting techniques are proposed to allow operation at typical switching frequency and still comply with the grid-connection standards.

The FSTPI AFE control structure is simple, it can be modulated by SVM or SPWM. Due to the simplicity and ease of implementation of the latter, SPWM is used as the modulation technique in this work, both with and without third order harmonic injection. Simulation studies on a developed model for a regenerative CHB drive with FOC controlled motor load operating in both rated motoring and regeneration modes are presented. The results of the proposed configuration using SPWM along with the proposed cell arrangement and carrier shifting techniques show promising performance to be applied in more economic and efficient regenerative CHB drives.

As the existing high switching AFE modulation techniques are associated with high switching power losses, fundamental frequency ends (FFEs) are proposed in this thesis to be applied in regenerative CHB drives as a more efficient solution where the switches are triggered at the fundamental frequency and thus nearly eliminating the switching power losses. Review of the existing FFE controllers in low voltage drives shows that they compromise between the DC-link voltage utilization factor, DC-link voltage regulation,

and the control of reactive power. To overcome this issue, a new controller approach is proposed in this work to achieve the highest DC-link voltage utilization along with DC-link voltage regulation and reactive power control. The performance of the proposed controller is verified through simulation studies of a 2L-VSI FFE in Matlab/Simlink.

Proposal and application of 2L-VSI FFEs in regenerative CHB drives using the proposed controller is investigated using theoretical analysis and simulation studies of the developed model of regenerative CHB with regenerative FOC controlled motor load. The phase-shifting transformer is used to cancel low order harmonics from the primary currents to comply with the grid connection standards. The system shows a promising performance to improve the design and the cost-effectiveness.

More economization is achieved by combining switch-count reduction and switching losses reduction through employing FSTPI FFEs in regenerative motor drives. In this case, phase-shifting transformer along with the proposed phase alternation connection are used to cancel low order harmonics from the primary and comply with the grid standards. Theoretical analysis and simulation studies of this system using developed model of regenerative CHB drive with regenerative FOC controlled motor load are provided. The system shows a propitious potential as a highly economic solution for regenerative CHB motor drives.

For experimental validation, a scaled-down version of 7-level regenerative CHB drive in addition to the front end and drive output controller circuits are implemented. The developed hardware is part of the collaboration project between the research and development department in Rockwell Automation Canada, and the High Power Electronics

Lab (HiPEL) motor drives research team in McMaster University, Canada. The setup is meant to be reconfigurable in order to operate with different proposed topologies and controller schemes. Due to the bounded time, preliminary results of the reduced switch-count configuration and its associated proposed techniques in STATCOM operation are shown for validation. The verification of the FFE proposed controller and its application is considered in the future work.

8.2 Contributions

The main contributions of the presented work are summarized as follows:

- Proposal of a new reduced switch-count regenerative CHB power cell configuration with FSTPI AFE. The proposed configuration reduces the number of switches in each CHB power cell by two switches.
- Proposal of phase-alternation connection method and carrier shifting techniques in conjunction with the modular structure of CHB motor drives to overcome the proposed configuration challenges.
- Proposal of a new general FFE controller with the highest DC-link utilization factor, DC-link voltage regulation, and reactive power flow control.
- Application of the proposed FFE controller in regenerative CHB motor drives with 2L-VSI FFEs to minimize the switching power losses.
- Combination of the proposed FFE controller and the proposed reduced switch-count CHB configuration by using FSTPI FFE, to reduce the switch-count and minimize the switching power losses.

- Experimental implementation of a reconfigurable scaled-down version of a regenerative CHB motor drive along with front end and drive output controllers for experimental validation of the proposed methods throughout the thesis.

8.3 Future Work

The two main ideas proposed in this thesis are switch-count reduction by employing FSTPI AFEs, and switching power losses minimization by using FFEs. As the main objective of this thesis is to develop more economic, efficient, and reliable industrial regenerative CHB drives, the future work considers further assessment and validation of the proposed ideas. The future work can be concluded in the following points:

- Sensitivity analysis of the FSTPI AFEs to the grid side disturbances.
- Analysis of reliability and fault-tolerant capability of the proposed FSTPI AFE based regenerative CHB drive.
- Experimental validation of the proposed FSTPI AFE based regenerative CHB drive with regenerative motor load.
- Sensitivity analysis of 2L-VSI FFEs to the grid side disturbances.
- Analysis of reliability and fault tolerant capability of the 2L-VSI FFE based regenerative CHB drive.
- Experimental validation of the proposed 2L-VSI FFE based regenerative CHB drive with regenerative motor load.
- Sensitivity analysis of FSTPI FFEs to the grid side disturbances.

- Analysis of reliability and fault tolerant capability of FSTPI FFE based regenerative CHB drive.
- Experimental validation of the proposed FSTPI FFE based regenerative CHB drive with regenerative motor load.

Publications

Published:

[1] **S. Badawi**, M. Narimani, Z. Cheng, and N. R. Zargari, "*A New Reduced Switch-Count Configuration for Regenerative Cascaded H-Bridge Converter*", *IEEE Energy Conversion Congress and Exposition* (ECCE), Detroit, MI, USA, Oct. 2020.

To be Submitted:

- ***Patents*:**

[2] **S. Badawi**, M. Narimani, Z. Cheng, and N. R. Zargari, "*Regenerative Cascaded H Bridge Power Supply*" – Filed, Nov. 2019, *App.#* 2019*P*-047-*US-CIP*.

- ***Journals*:**

[3] **S. Badawi**, M. Narimani, Z. Cheng, and N. R. Zargari, "*Reduced Switch-Count Regenerative Cascaded H Bridge Motor Drives*" to be submitted to *IEEE Transaction on Power Electronics*.

[4] **S. Badawi**, M. Narimani, Z. Cheng, and N. R. Zargari, "*Fundamental Frequency Ends in Regenerative Cascaded H Bridge Motor Drives*", to be submitted to *IEEE Transaction on Industrial Electronics*.

[5] **S. Badawi**, M. Narimani, Z. Cheng, and N. R. Zargari, "*Reduced Switch-Count Fundamental Frequency Ends in Regenerative Cascaded H Bridge Motor Drives*" – to be submitted to *IEEE Transaction on Power Electronics*.

[6] K. Zarei, **S. Badawi**, A. Abuelnaga, and M. Narimani, "*Regenerative Cascaded H-Bridge Motor Drives: A Review*" to be submitted to *Journal of Emerging and Selected Topics in Power Electronics.*

References

[1] B. Bugiardini, and F. Jason, “Matching VFD to Application Requirements”, *Rockwell Automation on demand webinars*, 20-5-2020.

[2] B. Wu, and M. Narimani, "High-Power Converters and AC drives ", *Wiley-IEEE Press*, 2017, ISBN: 978-1-119-15603-1.

[3] J. Rodriguez, J.S. Lai, and F.Z. Peng, "Multilevel inverters: a survey of topologies, controls, and applications," in *IEEE Transactions on Industrial Electronics*, vol. 49, no. 4, pp. 724-738, Aug. 2002, doi: 10.1109/TIE.2002.801052.

[4] S. Kouro, M. Malinowski, K. Gopakumar, J. Pou, L. G. Franquelo, B. Wu, J. Rodriguez, M. A. Pérez, and J. I. Leon, "Recent Advances and Industrial Applications of Multilevel Converters," in *IEEE Transactions on Industrial Electronics*, vol. 57, no. 8, pp. 2553-2580, Aug. 2010, doi: 10.1109/TIE.2010.2049719.

[5] A. Nabae, I. Takahashi and H. Akagi, "A New Neutral-Point-Clamped PWM Inverter," in *IEEE Transactions on Industry Applications*, vol. IA-17, no. 5, pp. 518-523, Sept. 1981, doi: 10.1109/TIA.1981.4503992.

[6] P. W. Hammond, "A new approach to enhance power quality for medium voltage AC drives," in *IEEE Transactions on Industry Applications*, vol. 33, no. 1, pp. 202-208, Jan.-Feb. 1997, doi: 10.1109/28.567113.

[7] M. Vijeh, M. Rezanejad, E. Samadaei and K. Bertilsson, "A General Review of Multilevel Inverters Based on Main Submodules: Structural Point of View," in *IEEE Transactions on Power Electronics*, vol. 34, no. 10, pp. 9479-9502, Oct. 2019, doi: 10.1109/TPEL.2018.2890649.

[8] PowerFlex 6000 Medium Voltage Drives Product Profile: : https://literature.rockwellautomation.com/idc/groups/literature/documents/pp/6000-pp003_-en-p.pdf

[9] HIVECTOL - HVI - E Medium Voltage Multi-Level Drives Brochure https://www.hitachi.com.au/documents/product/Variable_Speed_Drives_Brochure.pdf

[10] ABB general purpose drives ACS580MV catalog https://library.e.abb.com/public/80d9e920d55846ad90bfb2147fb7afaf/ACS580MV_catalog_3BHT490775R0001_RevC_EN.pdf

[11] Siemens Prefect Harmony GH180 https://new.siemens.com/global/en/products/drives/sinamics/medium-voltage-converters/sinamics-perfect-harmony-gh180.html

[12] M. Rastogi, R. H. Osman, and Y. Fukuta, "Variable-frequency drive with regeneration capability", *US7508147B2*.

[13] J. Wang, and Y. Li, "PWM rectifier in power cell of cascaded H-bridge multilevel converter," *2007 International Conference on Electrical Machines and Systems (ICEMS)*, Seoul, 2007, pp. 18-21.

[14] M. A. Perez, J. R. Espinoza, J. R. Rodriguez and P. Lezana, "Regenerative medium-voltage AC drive based on a multicell arrangement with reduced energy storage requirements," in *IEEE Transactions on Industrial Electronics*, vol. 52, no. 1, pp. 171-180, Feb. 2005, doi: 10.1109/TIE.2004.841095.

[15] J. Rodriguez et al., "High-voltage multilevel converter with regeneration capability," in *IEEE Transactions on Industrial Electronics*, vol. 49, no. 4, pp. 839-846, Aug. 2002, doi: 10.1109/TIE.2002.801238.

[16] P. Lezana, J. Rodriguez, D. Rojas and J. Pontt, "Novel cell based on reduced single-phase active front end for multicell converters," *31st Annual Conference of IEEE Industrial Electronics Society, 2005*. IECON 2005, Raleigh, NC, 2005, pp. 6 pp.-, doi: 10.1109/IECON.2005.1568995.

[17] P. Lezana, J. Rodriguez and D. A. Oyarzun, "Cascaded Multilevel Inverter With Regeneration Capability and Reduced Number of Switches," in *IEEE Transactions on Industrial Electronics*, vol. 55, no. 3, pp. 1059-1066, March 2008, doi: 10.1109/TIE.2008.917095.

[18] J. Rodriguez, J. Pontt, E. Silva, J. Espinoza and M. Perez, "Topologies for regenerative cascaded multilevel inverters," *IEEE 34th Annual Conference on Power Electronics Specialist, 2003. PESC '03*. Acapulco, Mexico, 2003, pp. 519-524 vol.2, doi: 10.1109/PESC.2003.1218109.

[19] J. R. Rodriguez, J. W. Dixon, J. R. Espinoza, J. Pontt and P. Lezana, "PWM regenerative rectifiers: state of the art," in *IEEE Transactions on Industrial Electronics*, vol. 52, no. 1, pp. 5-22, Feb. 2005, doi: 10.1109/TIE.2004.841149.

[20] J. Gong, L. Xiong, F. Liu and X. Zha, "A Regenerative Cascaded Multilevel Converter Adopting Active Front Ends Only in Part of Cells," in *IEEE Transactions on Industry Applications*, vol. 51, no. 2, pp. 1754-1762, March-April 2015, doi: 10.1109/TIA.2014.2360014.

[21] Z. Yang, J. Sun, X. Zha and Y. Tang, "Power Decoupling Control for Capacitance Reduction in Cascaded-H-Bridge-Converter-Based Regenerative Motor Drive Systems," in *IEEE Transactions on Power Electronics*, vol. 34, no. 1, pp. 538-549, Jan. 2019, doi: 10.1109/TPEL.2018.2818719.

[22] J. W. Finch, D. J. Atkinson and P. P. Acarnley, "Scalar to vector: general principles of modern induction motor control," *1990 Fourth International Conference on Power Electronics and Variable-Speed Drives (Conf. Publ. No. 324)*, London, UK, 1990, pp. 364-369.

[23] I. Boldea, A. Moldovan and L. Tutelea, "Scalar V/f and I-f control of AC motor drives: An overview," *2015 Intl Aegean Conference on Electrical Machines & Power Electronics (ACEMP), 2015 Intl Conference on Optimization of Electrical & Electronic Equipment (OPTIM) & 2015 Intl Symposium on Advanced Electromechanical Motion Systems (ELECTROMOTION)*, Side, 2015, pp. 8-17, doi: 10.1109/OPTIM.2015.7426739.

[24] L. K. Jisha and A. A. Powly Thomas, "A comparative study on scalar and vector control of Induction motor drives," *2013 International conference on Circuits, Controls and Communications (CCUBE)*, Bengaluru, 2013, pp. 1-5, doi: 10.1109/CCUBE.2013.6718554.

[25] https://www.iea.org/reports/multiple-benefits-of-energy-efficiency/emissions-savings

[26] J. P. Karunadasa, I. B. H. Bandara, W. D. D. Dayananda, K. G. S. U. Kumara and G. M. R. Tennakoon, "High Performance AC-AC Regenerative 5-Level NPC Converter with Capacitor Voltage Balancing," *2018 2nd International Conference On Electrical Engineering (EECon)*, Colombo, 2018, pp. 1-7, doi: 10.1109/EECon.2018.8540989.

[27] Gi-Taek Kim and T. A. Lipo, "VSI-PWM rectifier/inverter system with a reduced switch count," *IAS '95. Conference Record of the 1995 IEEE Industry Applications Conference Thirtieth IAS Annual Meeting*, Orlando, FL, USA, 1995, pp. 2327-2332 vol.3, doi: 10.1109/IAS.1995.530598.

[28] U. Bose, K. Divya, V. Jyothi and Sreejith S., "Performance analysis of four-switch three-phase inverter-fed induction motor drive," *2014 POWER AND ENERGY SYSTEMS: TOWARDS SUSTAINABLE ENERGY*, Bangalore, 2014, pp. 1-6, doi: 10.1109/PESTSE.2014.6805315.

[29] M. B. de Rossiter Correa, C. B. Jacobina, E. R. C. da Silva and A. M. N. Lima, "A General PWM Strategy for Four-Switch Three-Phase Inverters," in *IEEE*

Transactions on Power Electronics, vol. 21, no. 6, pp. 1618-1627, Nov. 2006, doi: 10.1109/TPEL.2006.882964.

[30] C. B. Jacobina, E. R. C. da Silva, A. M. N. Lima and R. L. A. Ribeiro, "Vector and scalar control of a four switch three phase inverter," *IAS '95. Conference Record of the 1995 IEEE Industry Applications Conference Thirtieth IAS Annual Meeting*, Orlando, FL, USA, 1995, pp. 2422-2429 vol.3, doi: 10.1109/IAS.1995.530611.

[31] P. Q. Dzung, Le Minh Phuong, P. Q. Vinh, N. M. Hoang and T. C. Binh, "New Space Vector Control Approach for Four Switch Three Phase Inverter (FSTPI)," *2007 7th International Conference on Power Electronics and Drive Systems*, Bangkok, 2007, pp. 1002-1008, doi: 10.1109/PEDS.2007.4487826.

[32] C. Brandao Jacobina, M. Beltrao de Rossiter Correa, A. M. Nogueira Lima and E. R. Cabral da Silva, "AC motor drive systems with a reduced-switch-count converter," in *IEEE Transactions on Industry Applications*, vol. 39, no. 5, pp. 1333-1342, Sept.-Oct. 2003, doi: 10.1109/TIA.2003.816526.

[33] IEEE Recommended Practice and Requirements for Harmonic Control in Electric Power Systems," in *IEEE Std 519-2014 (Revision of IEEE Std 519-1992)*, pp.1-29, 11 June 2014, doi: 10.1109/IEEESTD.2014.6826459.

[34] D. G. Holmes, and T. A. Lipo, " Pulse Width Modulation for Power Converters: Principles and Practice, " *Wiley-IEEE Press*, 2003, ISBN: 978-0-471-20814-3.

[35] Y. Patel, D. Pixler and A. Nasiri, "Analysis and design of TRAP and LCL filters for active switching converters," *2010 IEEE International Symposium on Industrial Electronics*, Bari, 2010, pp. 638-643, doi: 10.1109/ISIE.2010.5637475.

[36] J. R. Espinoza, G. Joos, J. Guzman, L. Moran and R. P. Burgos, "Selective harmonic elimination and current/voltage control in current/voltage source topologies: a unified approach," *IECON'99. Conference Proceedings. 25th Annual Conference of the IEEE Industrial Electronics Society (Cat. No.99CH37029)*, San Jose, CA, USA, 1999, pp. 318-323 vol.1, doi: 10.1109/IECON.1999.822217.

[37] Dr. D. Graovac, and M. Pürschel, "IGBT Power Losses Calculation Using the Data-Sheet Parameters," *Infineon Application Note*, V 1.1, Jan 2009.

[38] F. Becker, and Norbert Benesch, "Method for operating a converter and corresponding apparatus, " *US 8,116,108 B2*, 2012.

[39] A. Sayed-Ahmed, R. Kerkman and B. Seibel, "Analysis of IGBT based fundamental front end regenerative motor-drive systems," *2013 Twenty-Eighth Annual IEEE Applied Power Electronics Conference and Exposition (APEC)*, Long Beach, CA, 2013, pp. 765-772, doi: 10.1109/APEC.2013.6520296.

[40] N. Benesch, "Method and apparatus for setting a feedback power of a fundamental frequency clocked converter ," *US20100008115A1*, 2010.

[41] N. Benesch, B. Köhler, "Mains converter for switching, without any interruption, between clocked voltage-regulated operation and fundamental-frequency

unregulated operation, and method for switching a converter such as this without any interruption", *US20090285002A1*, 2009.

[42] A. Sayed-Ahmed, L. Wei and B. Seibel, "Industrial regenerative motor-drive systems," *2012 Twenty-Seventh Annual IEEE Applied Power Electronics Conference and Exposition (APEC)*, Orlando, FL, 2012, pp. 1555-1561, doi: 10.1109/APEC.2012.6166027.

[43] N. Benesch, "Method for reducing the reactive power requirement of a fundamental frequency clocked power supply side converter under no load and with low motor loading, " *US 7,983,060 B2*, 2011.

[44] Z. ZHANG, and A. Sayed-Ahmed, "Voltage angle control of a fundamental front end converter for a grid, "*US10122175B1*, 2018.

[45] J. D. Glover, M. S. Sarma, T. J. Overbye, "Power system analysis and design, " *Cengage Learning*, 2012, ISBN: 978-1-111-42577-7.